Hybrid numerical modeling of reverberation chambers

Zhao, Huapeng

2011

Zhao, H. (2011). Hybrid numerical modeling of reverberation chambers. Doctoral thesis, Nanyang Technological University, Singapore.

https://hdl.handle.net/10356/48663

https://doi.org/10.32657/10356/48663

Hybrid Numerical Modeling of Reverberation Chambers

Zhao Huapeng

School of Electrical and Electronic Engineering

A thesis submitted to the Nanyang Technological University
in partial fulfillment of the requirement for the degree of
Doctor of Philosophy

2011

Acknowledgements

First, I would like to express my deepest gratitude to my supervisor, A/P Shen Zhongxiang. The completion of this thesis would be impossible without his careful supervision. He suggested me a very important research topic for this thesis, and gave me a lot of insightful advice during my Ph.D. study. More importantly, he was always trying to teach me the practice I should follow to succeed in my research, which is beneficial for me in all my future work.

Second, I wish to acknowledge my indebtedness to my teammates, Dr. Zheng Boyu, Dr. Tan Weihua, Mr. Zhong Weiye, Mr. Tao Yun and Mr. Ali Reza Akbarzadeh. They were always there to assist me when I come across difficulties in my research and life.

Third, I would also like to thank Professor R. Mittra of the Pennsylvania State University for his insightful comments and helpful suggestions on the work in this thesis.

Last but not least, I deeply appreciate my family for their support, sacrifice and understanding. My special thanks are due to my wife who encouraged and accompanied me when I was depressed and provided me with many useful discussions on my work.

Table of Contents

Summary

This thesis deals with the efficient modeling of a full-scale reverberation chamber (RC), and a hybrid technique combining the discrete singular convolution (DSC) method and method of moments (MoM) is proposed to overcome difficulties in RC modeling.

An RC is constituted by a large rectangular cavity, in which stirrers and antennas are mounted/stationed. The large cavity is usually of rectangular shape, while stirrers and antennas are arbitrarily shaped and oriented. The challenge in modeling an RC is mainly from the large resonant cavity. Because of the existence of multiple resonances, conventional iterative solvers encounter the slow convergence problem, and direct solvers are usually utilized for solving matrix equations arising from RC modeling. In this case, the memory and CPU time requirement increases drastically with the number of unknowns, which limits the size of the RC to be modeled.

In this thesis, the hybridization of DSC method and MoM is developed to accelerate RC analysis. The hybrid method utilizes the DSC method for the efficient modeling of the large cavity, and applies the MoM to simulate stirrers and antennas. Using higher-order basis, the DSC method can obtain better accuracy using coarser grids compared to the conventional finite difference method. In this way, the number of unknowns is greatly reduced. However, the DSC method is not flexible in modeling structures of arbitrary shape. This is because structured grids are usually used to discretize the

computational domain. Meanwhile, using coarse grids further reduces the flexibility of the DSC method. The inflexibility of the DSC method is complemented by MoM in the proposed hybrid method. A Huygens' box is used to enclose a stirrer, and Huygens' principle is applied to obtain fields illuminating the stirrer. The induced current on the stirrer can be solved using MoM, and it is considered as a secondary source for the large cavity. The antenna is treated in the same way as the stirrer. The large cavity excited by current sources are then modeled using the DSC method. Since the induced current on stirrers and the excitation sources from antennas are distributed in an irregular domain, it is difficult to model them directly in the DSC method. A regularization technique for singular terms in differential equations is therefore introduced to model arbitrarily distributed current sources. The proposed hybrid method is first applied to the analysis of two-dimensional (2-D) transverse magnetic (TM) RCs. Its advantages are demonstrated using numerical examples on 2-D TM RCs. It is then used for the modeling of three-dimensional RCs. Numerical examples show that the proposed hybrid method is much more efficient than a pure MoM-based commercial software.

In order to further reduce the memory requirement, a hybrid technique combining recursive update DSC (RUDSC) method and MoM is developed. In the hybrid RUDSC-MoM, the DSC unknowns are first eliminated using a layer-based elimination algorithm, and the MoM unknowns are solved by a direct solver. The RC is then equivalent to a large cavity excited by known current sources, which is modeled by adopting the RUDSC method. In the layer-based elimination algorithm, the cavity is divided into many layers along its longest direction, and DSC unknowns are eliminated layer by layer. Employing the local property of differential operators, the layer-based elimination algorithm requires low memory cost. Meanwhile, the RUDSC method consumes a small amount of memory because it only needs storing two sparse dif-

ferentiation matrices. With its low memory consumption, the hybrid RUDSC-MoM extends RC modeling to higher frequencies, which would be impossible using the MoM-based commercial software.

List of Figures

List of Tables

List of Acronyms

ACRONYMS	FULL EXPRESSIONS
2-D	Two-Dimensional
3-D	Three-Dimensional
ABC	Absorbing Boundary Condition
AC	Anechoic Chamber
CEM	Computational Electromagnetics
CFIE	Combined Field Integral Equation
DSC	Discrete Singular Convolution
EFIE	Electric Field Integral Equation
EMC	Electromagnetic Compatibility
EUT	Equipment Under Test
FD	Finite Difference
FDTD	Finite Difference Time Domain
FEM	Finite Element Method
FE	Finite Element
GPU	Graphics Processing Unit
HIE	Hybrid Integral Equation
MFIE	Magnetic Field Integral Equation
MLFMA	Multilevel Fast Multi-pole Algorithm

MoM	Method of Moments
MOD	Marching-on-in-Degree
MOT	Marching-on-in-Time
OATS	Open Area Test Site
RC	Reverberation Chamber
RU	Recursive Update
RUDSC	RU Discrete Singular Convolution
RUFD	RU Finite Difference
TDDSC	Time-Domain DSC
TDIE	Time-Domain Integral Equation
TLM	Transmission Line Matrix
TM	Transverse Magnetic

Chapter 1

Introduction

1.1 Motivation

As modern electromagnetic environment becomes more and more complex, today's electronic products should be designed so that they do not disturb the proper operation of other products. Meanwhile, they should also be able to withstand electromagnetic radiation emitted from all kinds of sources. The electromagnetic compatibility (EMC) is hence becoming a crucial aspect of modern electronic devices. In this case, the effective and accurate testing of EMC becomes important for successful product development. Typical EMC measurement environments include the open-area test sites (OATS), (semi-) anechoic chambers (ACs), reverberation chambers (RCs) and so on. Of these measurement facilities, the RC is becoming more and more popular because of its unique advantages over other measurement facilities.

Figure 1.1 shows a typical RC environment. It consists of a shielded metallic enclosure, a rotating stirrer and a transmitting antenna. The rotating stirrer changes the boundary condition of the RC so that many different modes are excited. Hence, RC is also called overmoded cavity. Near the center of RC, a test volume is created,
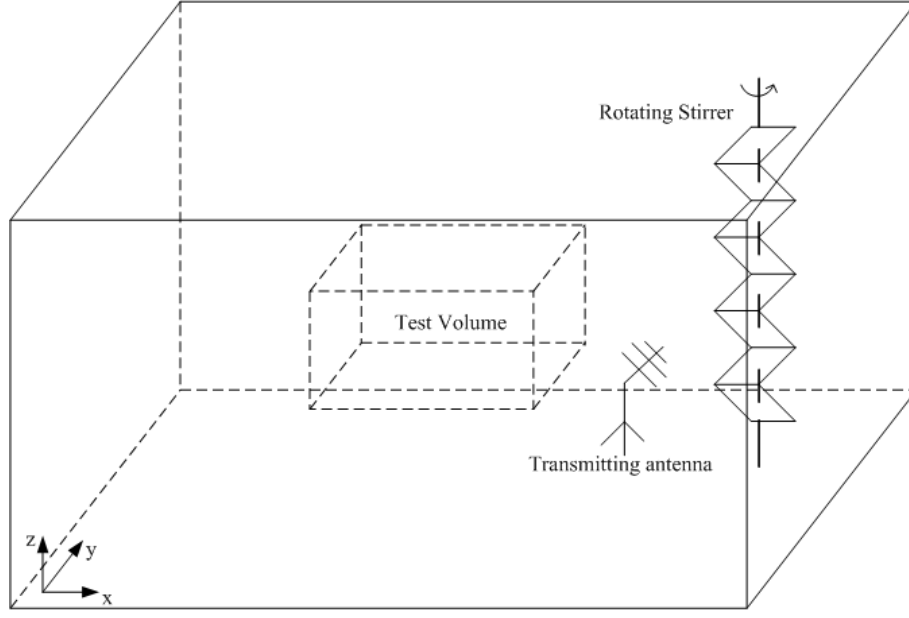
Figure 1.1: A typical RC environment.

where the field is statistically isotropic and uniform. There are two methods of rotation for the stirrer: continuous and stepwise rotations, which are termed as mode-tuned and mode-stirred, respectively. This thesis focuses on the mode-stirred RC. Therefore, the term RC refers to mode-stirred RC in the rest of this thesis.

RC measurements have the following benefits. First, the RC simulates the real-world electromagnetic environment much better than other facilities. When using OATS or ACs, it is assumed that the equipment under test (EUT) radiates or receives similarly to a monopole, dipole or other antennas. However, the direction, polarization and amplitude of the incident wave are random in RC, which better simulates the practical electromagnetic environment. Second, as a shielded metallic chamber, high electric field strength can be obtained with a moderate input power to the RC, which saves the cost of power amplifier. Finally, the building cost of RCs is lower than that of ACs. ACs are usually made of broadband absorbing materials, which are expensive and difficult to maintain. RCs are comprised of metallic materials, which

2

are usually cheaper than absorbing materials. The advantages of RC measurements lead to its standardization in 2003 [1], which indicates a more wide-spread use of this measurement technique.

Although the RC was originally designed for EMC measurements, its application has recently been extended. Other applications of RC include the measurement of radar cross section [2], absorbing cross section [3, 4], multiple input multiple output antennas [5–10], and small antennas [11–13]. Because of the statistical electromagnetic environment provided by an RC, it is particularly suitable for the measurements of wireless communication antennas. In many applications, RC works better than the AC. In some cases, RC may be the unique choice because of its advantages over other facilities.

In the meanwhile, new stirring techniques are being proposed to optimize the stirring effectiveness and to reduce the measurement time [14–22]. The mechanical stirring approach can produce electromagnetic environment satisfying the IEC standard [1]. However, rotating a stirrer is time consuming. A potential alternative to the mechanical stirring is the electronic stirring [16–22]. In electronic stirring, the field distribution inside the chamber is changed by switching on and off antennas located at different positions. As the position of active excitation antennas changes, the field distribution inside the RC varies. Compared to slowly rotating mechanical stirrers, electronic stirring may significantly reduce the measurement time.

With the increasing popularity of RC, numerical RC analysis is attracting more and more interest. RC modeling is important for the following reasons. First, RC modeling can help RC designers optimize the performance of an RC and examine the effectiveness of new stirring techniques. Although detailed information on RC

3

was given in [1], only basic guidelines on designing and constructing an RC were presented, which were mostly derived from years of practical experience. An optimized RC design is usually obtained through a time-consuming trial-and-error approach. On the other hand, RC modeling allows RC designers to predict and optimize the performance of an RC before its fabrication, which will save time and cost in RC designing. Furthermore, it is economical to check the effectiveness of new stirring methods using numerical techniques before costly experiments. Second, as an alternative to measurements, theoretical modeling can save the measurement cost. If one can simulate the RC numerically, RC measurements can be supplemented with numerical simulations, which can reduce the cost of experiments. Finally, numerical modeling is also helpful for the development of new RC applications. Before actually using the chamber and investigating new RC applications, one may simulate a new application using modeling techniques. This will reduce the cost at an early stage.

Despite the great importance of RC modeling, efficient numerical techniques are still not available for the analysis of a full-scale practical RC. This is mainly because it is a challenging task to model such an electrically large resonant chamber in a broad frequency range and over multiple stirrer positions. Because of an RC's resonance nature, conventional iterative solvers encounter the slow convergence problem in solving matrix equations resulting from RC modeling. In this case, direct solvers are usually utilized. This indicates that RC modeling requires large memory and long CPU time [23], which in turn limits the size of the RC to be modeled. In the meanwhile, many simulations are needed for the modeling of multiple stirrer positions. This again substantially increases the simulation time. In order to accelerate RC modeling, a lot of efforts have been made towards the development of efficient numerical RC modeling, which has led to two kinds of modeling techniques: statistical and deterministic approaches. Statistical approaches [24–27] are mainly under

4

the hypothesis that an RC is well stirred, and plane wave superposition is applied to simulate the statistical electromagnetic environment in the RC [24, 26, 27]. Because statistical approaches do not model the large cavity directly, they are fast as long as the equipment under test is not electrically large. On the other hand, statistical approaches are not as accurate as deterministic approaches. Deterministic approaches utilize accurate numerical methods to model the whole RC, and these include the method of moments (MoM) [20, 23, 28–30], the finite element method (FEM) [16, 31], the finite difference time domain (FDTD) method [32–36], the transmission line matrix (TLM) method [37–39], and so on. These methods are accurate but require high computational resources in modeling a large RC. Therefore, it is highly important to develop new methods for efficient and accurate modeling of full-scale RCs.

A careful examination shows that existing methods have their respective advantages and disadvantages in modeling an RC. The MoM and FEM are geometrically flexible, and they are good candidates for the modeling of stirrers. Moreover, the MoM is particularly suitable for the analysis of conducting structures (e.g. the stirrer in an RC), because only the surface of a conducting object needs discretization using MoM. However, both MoM and FEM require the solution of a matrix equation, which is computation intensive. On the other hand, the FDTD method does not need solving matrix equation. The main drawback of the FDTD method is its low spatial resolution. This is due to the structured grids utilized by the FDTD method[1]. When thin wire conducting structures (e.g. the wire antenna in an RC) are modeled, both FDTD and FEM are not as powerful as MoM. The aforementioned discussions indicate that a single numerical method is not competent for RC modeling. Hence, it is desirable to hybridize different numerical methods in order to combine their respective advantages

---

[1]The FDTD method here refers to the conventional FDTD method. There are variants of FDTD method with improved geometrical flexibility (e.g. the conformal FDTD method [40, 41]).

and to overcome their shortcomings, which motivates the work in this thesis.

1.2 Objectives

The goal of this thesis is to accelerate RC modeling by hybridizing different numerical methods. In order to achieve the final objective, the following tasks have been envisaged.

1. To find the best candidates for modeling individual parts of an RC, an extensive literature survey is first conducted. This allows us to develop a powerful hybrid method employing the most suitable modeling technique for every single component of an RC and combining advantages of the state-of-the-art numerical methods.

2. It is known that the main challenge in modeling an RC is from the large resonant cavity. On the other hand, the geometrical simplicity of the cavity can be utilized to reduce the computational burden. For simplicity, we begin our study by developing an efficient and accurate method for the modeling of a two-dimensional (2-D) transverse magnetic (TM) cavity.

3. Since stirrers and transmitting antennas are arbitrarily shaped conducting objects, they may be simulated using MoM. The developed efficient cavity modeling method will be combined with MoM to accelerate RC modeling. The 2-D TM case will again be considered in order to explore the way of hybridization and to study the advantages of the hybrid method.

4. The success of our 2-D hybrid method will pave the way for the development of 3-D hybrid method. By developing a 3-D hybrid method, we expect to achieve the fast analysis of 3-D RCs. The proposed hybrid method is expected to outperform a pure MoM-based commercial software.

5. For simplicity, a point current source can be used as the excitation in previous steps. In practice, wire antennas are often used as transmitting antennas of an RC. For the modeling of wire antennas, an MoM code will be implemented, and it will be included in the 3-D hybrid method. After incorporating the MoM for wire structures, the hybrid method will be able to efficiently model a practical full-scale RC.

6. It is noted that the memory requirement for RC modeling is high because direct solvers are usually used to solve the matrix equation. In order to reduce the memory requirement, a new solution method will be developed. With its low memory consumption, the new solution method will extends RC modeling to higher frequencies.

It should be noted that the numerical modeling of 2-D transverse electric RC is similar to that of the 2-D TM RC. Hence, only 2-D TM RC is considered in this thesis.

1.3 Key Contributions of the Thesis

In this thesis, three key contributions have been made for RC modeling. They are hybridization of the discrete singular convolution (DSC) method and MoM for the modeling of 2-D TM RCs, efficient analysis of 3-D medium-sized RCs by hybrid DSC-MoM, and memory-efficient modeling of RCs using hybrid recursive update DSC (RUDSC)-MoM. 'Medium-sized' means the volume of the RC is from 12 λ^3 to 100 λ^3, where λ is the wavelength.

Hybridization of DSC and MoM for 2-D TM RC Modeling

Through a thorough literature review, this thesis first finds the most suitable modeling technique for every individual part of an RC. The DSC method is chosen to model the

large cavity of an RC. The DSC method is a generalized higher-order finite difference (FD) method. Compared to second-order methods, it needs much less unknowns in modeling the large cavity. On the other hand, the DSC method is not able to model arbitrarily shaped objects because of its coarse structured grids. The MoM is therefore adopted to model the stirrers/antennas. The way of combining the DSC method and MoM is first explored in the 2-D TM case, and the Huygens' principle and regularization technique are used to couple the two methods together. A few numerical experiments are conducted to validate the proposed hybrid method and to examine its performance. Taking advantage of the high efficiency of the DSC method, the hybrid method is shown to be much more efficient than a pure MoM in modeling 2-D TM RCs.

Efficient Analysis of 3-D Medium-Sized RCs by Hybrid DSC-MoM

The success of 2-D hybrid method lays the foundation for a 3-D hybrid method. In the 3-D case, the RWG basis is utilized to expand the induced current on the stirrer and the equivalent current on Huygens' box. The property of RWG basis is employed to connect the DSC field solution with the excitation field in MoM. The regularization technique for 3-D surface current is applied to model arbitrarily distributed current sources in structured grids of the DSC method.

Modeling the large cavity using the DSC method, the number of unknowns is greatly reduced. The performance of the proposed hybrid method is compared with a pure MoM-based commercial software. It is found that the proposed hybrid method requires much shorter CPU time and consumes less memory compared to the commercial software. For medium-sized RCs, the proposed hybrid method takes a few hundred seconds to analyze one stirrer position. The same task costs the commercial software thousands of seconds. Therefore, the proposed hybrid method constitutes an

important contribution to the development of efficient RC modeling techniques.

Hybrid RUDSC-MoM for Memory-Efficient Modeling of RCs

Due to the usage of a direct solver, the memory requirement of modeling an RC at higher frequencies is beyond the capability of a personal computer. In order to reduce the memory cost, a hybrid RUDSC-MoM is proposed in this thesis. In hybrid RUDSC-MoM, the DSC and MoM unknowns are solved separately, each using the most suitable method. In order to solve the DSC and MoM unknowns individually, a layer-based elimination algorithm is developed to efficiently eliminate the DSC unknowns. Direct solver is then utilized to solve the MoM unknowns. The RUDSC method is finally applied to solve the DSC unknowns after obtaining the MoM solution. In the proposed layer-based elimination algorithm, the cavity is divided into many layers along its longest direction, and the DSC unknowns are arranged layer by layer. Utilizing the local property of the curl operator, the layer-based elimination algorithm retains low memory consumption. In the meanwhile, the storage complexity of RUDSC method is low because only two sparse differentiation matrices need storing. With its reduced memory cost, the hybrid RUDSC-MoM extends the modeling of a full-scale RC to higher frequencies, which should be a leap in the development of efficient RC modeling techniques.

1.4 Organization of the Thesis

The rest of this thesis is organized as follows. In Chapter 2, a thorough literature review is presented. Existing RC modeling techniques are first summarized, and their advantages and shortcomings are discussed. Recent advances in computational electromagnetics (CEM) are then studied in order to choose the state-of-the-art techniques for hybrid numerical RC modeling.

Chapter 3 presents a hybrid method for the efficient modeling of 2-D TM RCs. Formulation of the hybrid method is described in detail, and numerical examples are presented to illustrate the benefits of the hybrid method. Performance of the 2-D hybrid method is compared with that of a pure MoM.

In Chapter 4, 3-D hybridization of the DSC method and MoM is introduced. Numerical examples on 3-D RCs are presented. Choice of grid size in the DSC method is studied. CPU time and memory cost of the proposed 3-D hybrid method is compared with those of a commercial software. Stirring effects of three different stirrers are investigated using the proposed 3-D hybrid method.

The hybrid RUDSC-MoM is proposed in Chapter 5. Derivation of the RUDSC method for the modeling of a large cavity is first described in detail. The advantages of RUDSC method are shown through comparisons with alternative methods. Layer division of a cavity along its longest direction is then introduced. Pseudocode of the layer-based elimination algorithm is given. Computational and storage complexity of the layer-based elimination algorithm is studied. Through the application of the layer-based elimination algorithm, the RUDSC method is combined with MoM for memory-efficient modeling of RCs. Furthermore, the MoM for wire structures is incorporated into the 3-D hybrid method in order to take the practical transmitting antenna into account.

Finally, Chapter 6 summarizes the work presented in this thesis, and gives recommendations for future work.

Chapter 2

Literature Review

As it is noted in Chapter 1, numerical RC modeling has attracted much interest recently because of its great importance in RC design and applications. This chapter first reviews existing RC modeling methods, and discusses their advantages and weaknesses. Recent developments in CEM are then summarized in order to find the state-of-the-art techniques to complement the weaknesses of existing RC modeling methods.

2.1 Existing RC Modeling Methods

Existing RC modeling techniques can generally be classified into two categories. The first one is the statistical models of RC [26, 27]. Most statistical models are based on the assumption of local plane waves in the RC, and they avoid the direct modeling of the large cavity, which makes them highly efficient. However, statistical models can only simulate the random environment instead of the RC itself. In order to model the whole chamber, a lot of effort was made towards the development of deterministic approaches, which utilize accurate numerical methods and need extensive computational resources. In order to understand their advantages and drawbacks, statistical

and deterministic modeling approaches are summarized in Sections 2.1.1 and 2.1.2, respectively.

2.1.1   Statistical Modeling Approach

The theoretical basis of statistical modeling approaches is the plane wave superposition, which was well documented in [42]. Take the susceptibility test as an example. Direct simulation of susceptibility test in RC involves the entire volume of the RC, the stirrers, and the antennas. The computation time is a function of the chamber volume, the wall conductivity, the frequency range, and the EUT characteristics. Hence, it will require long CPU time and large memory to directly simulate this measurement scenario. On the other hand, under the hypothesis that the RC is well stirred, the working volume may be considered as an electromagnetic environment where the incident wave is random in its incident angle, amplitude and polarization. Based on this understanding, the plane wave superposition was proposed to simulate the random environment of the RC. In the plane wave superposition, the simulation only involves the EUT. Therefore, the computation time is only a function of the characteristics of the EUT. Moglie et al. [35] combined the standard FDTD method with the plane wave superposition to simulate the induced current on the load of a transmission line in an RC. Good agreement was obtained between simulated and measured results both for the average value and for the maximum value of the induced current on the line.

Recently, Bonnet et al. [25] proposed a stochastic collocation method for the simulation of a mode-stirred RC. This method relied on an analogy between an RC and an empty enclosure whose wall conductivity was randomly characterized. The distribution law of cavity wall conductivity is obtained by measurements. A stochastic collocation method was then applied to numerically assess electromagnetic field from

a low number of empty cavity (without stirrer) simulations. Since efficient methods exist for the modeling of an empty cavity, the stochastic collocation method notably reduces the computation time.

In conclusion, the statistical modeling methods either model the EUT only or simulate an empty cavity alone. They are very efficient because the EUT is not very large and an empty cavity can be modeled efficiently using some special algorithm. Nevertheless, statistical methods can only provide statistical parameters. They are not useful for the characterization and optimization of an RC. Furthermore, they are not as accurate as deterministic methods. Therefore, it is of great importance to develop efficient deterministic modeling methods.

2.1.2 Deterministic Modeling Approach

In deterministic modeling methods, the whole structure of an RC is discretized, and Maxwell's equations are numerically solved to obtain the field or current solution. They are therefore accurate but require long CPU time and large memory. Typical deterministic methods include the MoM [20, 28–30, 43], the cavity Green's function method [20], the FEM [16, 19, 31, 44], the FDTD method [32–36, 45–48], the TLM method [37–39], and the modal expansion method [18, 21, 49]. These methods are summarized as follows.

The MoM

The MoM [43] is based on the integral equation, and it is a flexible and accurate modeling technique. It usually adopts some kind of basis function to expand the current. A set of matrix equation is obtained by substituting the current expansion into the integral equation and enforcing the boundary condition. After solving the

matrix equation, one can obtain the current distribution and then calculate the desired parameters. In practice, triangle is usually used to discretize a surface structure, and the RWG basis [50] is then adopted to expand the current flowing along the surface. Because of its high accuracy and flexibility, the MoM has been widely used for the analysis of scattering and radiation from arbitrarily shaped 3-D conducting objects. In scattering and radiation problems, iterative solvers are usually used to solve the matrix equation in order to reduce the memory cost.

Due to the resonance nature of an RC, iterative solvers may suffer from the slow convergence problem, and direct solvers are commonly used to solve the matrix equation in RC modeling. In this case, the MoM has the storing and computational complexity of $O(N^2)$ and $O(N^3)$, respectively. N is the number of unknowns, and it scales as f^2 for 3-D conducting objects, where f denotes the frequency of interest. In other words, the storage and computing complexity is approximately $O(f^4)$ and $O(f^6)$, respectively. Hence, the CPU time and memory requirement increases dramatically against the frequency, which prohibits the application of MoM at higher frequencies. The MoM-based commercial software FEKO® was applied for RC modeling in [30], and it was stated that the excessive runtime rendered RC simulations at high frequencies useless. On the other hand, because of its geometry flexibility, the MoM is particularly suitable for the modeling of stirrers and antennas inside an RC. Therefore, the MoM may be hybridized with an efficient cavity modeling method to realize efficient and flexible modeling of RCs.

Cavity Green's Function Method

In a conventional MoM, the free space Green's function is adopted, and the large cavity is directly modeled, which makes the number of unknowns large. On the other hand, the boundary condition of the large cavity can be enforced using cavity Green's

function, which is called the cavity Green's function method. In cavity Green's function method, only objects inside the chamber need discretization, which substantially reduces the number of unknowns. Laermans et al. [29] proposed to model a 2-D RC with cavity Green's function. Although cavity Green's function method greatly reduces the number of unknowns, the computation of cavity Green's function is complicated and time-consuming. Laermans et al. concluded that only for very small objects in a chamber, their method was advantageous over conventional MoM. Kildal et al. [20, 28] developed the 3-D cavity Green's function method for the modeling of a dipole in RC, and they utilized a few special techniques to accelerate the calculation of cavity Green's function. Kildal's method is very powerful in modeling small wire antennas in an RC. Nevertheless, when a full-scale RC with a mechanical stirrer is modeled, the computation time would still be prohibitive due to the overhead of calculating the cavity Green's function, though its computation can be accelerated by improved implementation of cavity Green's function method [51]. Therefore, the cavity Green's function method is not applicable to RCs with relatively large objects inside (e.g. an RC with mechanical stirrers and a large EUT).

The FDTD Method

The FDTD method [48] is a popular numerical technique in electromagnetics. It directly discretizes Maxwell's equations of differential form by approximating the differential operators using central difference. The FDTD method is efficient because it does not need to solve a linear equation. Furthermore, as it works in time-domain, wide-band information can be obtained with one single simulation.

Due to its high efficiency, the FDTD method was widely used for RC modeling. In [45–47], Kouveliotis et al. applied the FDTD method to the modeling of the vibrating intrinsic RC. Moglie et al. [32] studied the loss modeling of the RC and

analyzed the convergence of FDTD method. They simulated the susceptibility and coupling tests in RC with the FDTD method [35, 36]. In [35], current induced on the load of a transmission line was measured and simulated in an RC environment to characterize the susceptibility of the transmission line. In order to study the level of coupling between external field and an enclosure with slot, the induced current on a loop inside the enclosure was simulated in [36]. Because the loss of an RC is frequency-dependent, it is difficult to model the loss directly for wide-band excitation. In [33,34], the loss was modeled in a postprocessing step to overcome the difficulty of modeling dispersive loss. Even with the high efficiency of FDTD method, the modeling of a medium-sized RC still requires a few days on a personal computer [32] . This is due to the numerous multiple reflections and slow damping of energy in an RC.

A shortcoming of the FDTD method is that it is not as flexible as MoM. In the FDTD method, structured grids are usually adopted to discretize the computational domain. This makes it difficult to model the stirrers of an RC in the FDTD method. In existing methods, staircase approximation is usually adopted to model the geometry of a stirrer. In [52], the concept of digital geometry was introduced to generate the staircase grids. Compared to the triangular representation of stirrers in MoM, the staircase approximation introduces undesired roughness on the surface of the stirrer. This will contaminate the field calculations significantly [53], in which case very fine grids are required to suppress the error. Therefore, the FDTD method is not flexible in modeling the stirrers of arbitrary shape. However, it is suitable for the modeling of the large rectangular cavity.

The FEM

The FEM [44] is another popular numerical technique in electromagnetics. In FEM, the fields are expanded with a proper basis. After substituting the field expansion into

16

Maxwell's equations, Galerkin's matching process is applied to make the equations satisfied. Utilizing tetrahedron for discretization of the computational domain, the FEM is geometrically flexible. Based on Maxwell's equations of differential form, the FEM can easily model medium inhomogeneity. Therefore, the most widely used commercial software high frequency structure simulator® [54] is developed based on the FEM.

Requiring the solution of a matrix equation, FEM analysis of an RC is also time-consuming. In [16] and [19], Bunting et al. applied the FEM to investigate the effectiveness of frequency stirring. However, they only simulated an internal cavity in the 2-D case, and they took a cavity with aperture as a simplified model of an RC in the 3-D case. Orjubin et al. [31] used the FEM modal approach for RC analysis. They first determined the modes of an RC using the FEM and then expressed the field in the RC with modal expansions in a single post-treatment. Compared with the harmonic analysis, the computational cost is reduced with this FEM modal approach. However, their derivations have many limitations and the validity of their method is yet to be fully examined [31].

In conclusion, the FEM alone is not competent for efficient analysis of an RC. The advantage of FEM lies in its geometrical flexibility and its ability in modeling material inhomogeneity. For RC modeling, the FEM may be used to model arbitrarily shaped EUT constituted by inhomogeneous materials.

Other Methods

Other RC modeling methods include the TLM method [37–39] and the modal-expansion method [18, 21, 49]. In [37], the TLM method was used to optimize the design of the stirrer. Instead of modeling the whole chamber, the stirrer was simulated in free

space, and the free-space scattering performance was correlated with the chamber performance. A low-resolution TLM model of an RC was validated in [38]. A variety of statistical and heuristic approaches were used to quantify the level of agreement, and the likely lower bound for the quality of comparisons between simulations and measurements was set. Another purpose of [38] was to assess whether a coarse implementation of a TLM model provided a sufficiently high level of agreement for RC modeling. It was concluded that the agreement between simulation and measurement was satisfactory considering the saving of simulation time. However, even with the coarse model, it would require 200 days to simulate 200 stirrer positions of a medium-sized RC. Meanwhile, the TLM method also utilizes structured girds, and staircase approximation is usually adopted to model arbitrarily aligned stirrers, which may introduce undesired error in field calculations. The modal-expansion method is a semi-analytical method, and it is similar to the cavity Green's function method. It expands the fields in the chamber using standard cavity modes, and enforces the boundary condition on the objects inside the chamber using some matching process. The modal-expansion method avoids direct modeling of a large cavity, and it requires less unknowns. However, it is only applicable to simple objects in a small cavity, and a large number of modes will be required to accurately express the fields in a large chamber. Furthermore, it is difficult to enforce the boundary condition of complicated objects in a modal-expansion method.

2.2 Recent Advances in CEM

The review in Section 2.1.2 indicates that most existing RC modeling techniques utilized conventional numerical methods, which are not optimized for RC modeling. To improve the efficiency and accuracy of conventional methods, new numerical techniques were recently developed. In order to examine their possible application in RC

modeling, five recent advances in CEM are reviewed in this section. They are fast algorithms based on integral equations, hybrid integral equation, higher-order methods, hybrid techniques, and matrix free method.

2.2.1 Fast Algorithms Based on Integral Equations

As mentioned in Section 2.1.2, the MoM leads to computational and storing complexity of $O(N^3)$ and $O(N^2)$, respectively. To accelerate the computation, fast algorithms based on integral equations were developed. A widely used fast algorithm is the multilevel fast multi-pole algorithm (MLFMA) [55–57], which is based on the multi-pole expansion of the free space Green's function. The principle and procedure of MLFMA were well documented in [57], and some tricks on implementation of MLFMA were summarized in [56]. It should be mentioned that MLFMA reduces the computational and storing complexity of MoM to $O(N \log N)$, which enables the solution of problems with hundreds of thousands of unknowns on a single personal computer. With the aid of parallel techniques, several research groups [56, 58–60] successfully solved problems with millions or even ten millions unknowns in only several hours.

The efficiency of MLFMA is no doubt attractive, however, this efficiency is obtained at the cost of sacrificed accuracy. In [61], the multi-pole expansion error was studied. It was shown that the expansion error was nearly 10 percent in some cases. A 10 percent error occasionally occurring in MLFMA results in smaller error in the matrix vector product, because MLFMA is for far-interactions only and there are no approximations in near interactions. Hence, the final far fields are accurate [62], and the MLFMA can be applied for the computation of radar cross section, antenna radiation pattern and so on. In these situations, the accuracy requirement is relatively low and MLFMA works well. However, when applied to the near-field computation,

MLFMA doesn't generate acceptable results [23]. To our best knowledge, the application of other fast algorithms (e.g. the adaptive integral method [63]) are also limited to scattering and radiation problems up to now. Therefore, most fast algorithms based on integral equations are not applicable to RC modeling because of the high accuracy requirement in RC analysis.

2.2.2 Hybrid Integral Equation

In modeling a closed structure, the combined field integral equation (CFIE) [64] is usually used in order to eliminate the internal resonance. The CFIE is a linear combination of the electric field integral equation (EFIE) and the magnetic field integral equation (MFIE), and it is only applicable to closed objects due to the usage of the MFIE. On the other hand, there are many structures with both open and closed surfaces. In order to efficiently model these structures, a hybrid integral equation (HIE) was proposed based on the CFIE [65]. The HIE is essentially a hybridization of CFIE and EFIE, in which CFIE is applied for the closed surface and EFIE is used for the open surface. It was shown that the HIE was effective in improving the convergence when the open surface was small compared to the closed surface [65].

The HIE seems very promising for RC modeling at its first look because the RC is constituted by a large closed cavity with small open structures. However, a careful examination indicates that the HIE is not applicable to RC modeling. HIE is effective because the CFIE can make the internal resonant frequency of a cavity scatter become a complex number [66]. However, because the resonant frequency of an RC is physical, it can not be changed by the CFIE. Figure 2.1 illustrates the condition number of the interaction matrix in modeling an internal cavity using different integral equations. It is seen that the CFIE fails to reduce the condition number near the physical resonant
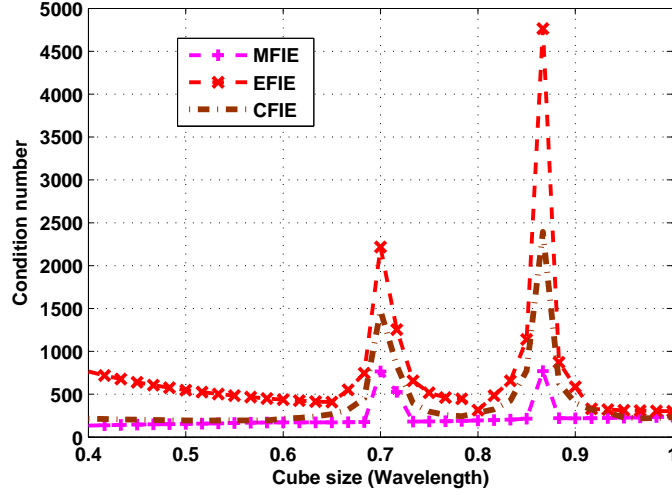
Figure 2.1: Condition number of the interaction matrix in modeling an internal cavity using EFIE, MFIE, and CFIE.

frequency of the cavity. Hence, the HIE can not be used for RC modeling.

2.2.3 Higher-Order Methods

Higher-order methods are based on modifications made to the expansion basis of conventional methods. In conventional methods, the number of unknowns goes high as the electrical size increases. The computational cost is hence increased drastically with the frequency. Using higher-order basis, better accuracy can be obtained using coarser grids. In this way, a significant reduction of the number of unknowns is realized, and the CPU time and memory requirement is substantially reduced. In the past, various authors developed higher-order MoM [67–69], FEM [70–73] and FDTD method [74–76]. Of these new higher-order methods, the DSC method [74, 75] is very attractive. The DSC method [74, 75] is a generalized higher-order FD method. With a higher-order interpolation basis (e.g. the Lagrange interpolation basis [75]), the field quantities are expanded and the differential operators in Maxwell's equations are acted directly to the field expansion. With the expansion coefficients being constant, the differential operators are actually taken upon the basis, whose derivatives can

be computed analytically. In this way, Maxwell's equations are discretized into a matrix equation, which can be solved to obtain the field solution. It has been shown that the DSC method is much more efficient and accurate than conventional FD methods [75]. The DSC method is similar to the pseudospectral method [77, 78], because they both aim to find the accurate approximation of the spatial differentials in Maxwell's equations. Discussions on the similarities and differences between them can be found in [79, 80].

In RC modeling, the DSC method is very suitable for the modeling of the large cavity. The DSC method not only greatly reduces the number of unknowns, it also needs little effort in building the matrix equation. This is due to the translation invariant property of the curl operator and the analytical calculation of the differential of basis functions. On the other hand, the higher-order MoM requires long CPU time to calculate the interaction matrix. This is because integration of complicated higher-order basis is needed in higher-order MoM.

2.2.4 Hybrid Techniques

Hybrid techniques combine different methods to explore their respective advantages. The FEM and FDTD method are flexible in modeling inhomogeneous material. However, they require the absorbing boundary condition (ABC) to truncate the computational domain when modeling open-region problems, which increases the computational burden. On the other hand, it is time-consuming to solve problems involving inhomogeneous media using MoM, but the radiation boundary condition is automatically satisfied in the integral equation. Therefore, the finite element-boundary integral method [81–85] was developed for modeling scattering and radiation by inhomogeneous media. Another kind of hybrid techniques [86–89] combine the FD method in

time or frequency domain with MoM. The benefits are either modeling fine structure with FD method [86–88] or eliminating the need for ABC in the FD method [89]. For waveguide structures, the modal-expansion method has natural advantages. However, a pure modal-expansion method is only applicable to regular structures. To model the irregular parts in a waveguide component, hybrid finite-element-modal-expansion method was developed by Shen et al. [90]. More hybrid techniques combining modal-expansion and other methods can be found in [91]. For transient modeling of a mixed-scale structure (i.e. large scale objects and fine features are coexistent), it will be time consuming to model the whole structure using an explicit time-domain methods, because the time step should be very small to satisfy the stability condition. On the other hand, an implicit time-domain method is unconditionally stable but it is awkward in modeling the large object due to the requirement of solving a matrix equation. Hence, the hybrid implicit-explicit method was proposed for modeling mixed-scale structures [92,93]. The hybrid implicit-explicit method accurately models fine structures using an implicit method and efficiently analyzes the large object using an explicit method. Therefore, the computational burden in solving a matrix equation is greatly reduced, and the time step size can be chosen according to the grid size in the explicit method. In summary, hybrid techniques are powerful in solving complex electromagnetic problems. They combine advantages of different methods and overcome their limitations. For RC modeling, a hybrid technique is desirable because it can utilize the most suitable method in modeling every single component of the RC.

2.2.5   Matrix Free Method

Solving a matrix equation is usually necessary for frequency-domain methods. However, a time-domain method[1] does not require the trouble of solving a matrix equation

---

[1]Here, we refer to an explicit time-domain method. For implicit time-domain method, it is still needed to solve a matrix equation.

directly (e.g. the FDTD method). In a time-domain method, Maxwell's equations can be numerically solved using a marching-on-in-time (MOT) scheme. Starting from zero and recursively updating the electromagnetic fields, solution to the time-domain Maxwell's equations can be obtained without solving a matrix equation. Recently, the concept of MOT was extended to frequency-domain methods [94]. Beginning with the time-domain Maxwell's equations and assuming periodic excitation, a recursive update scheme was derived to obtain the frequency-domain solution without solving a matrix equation. The method was named as matrix free method in [95]. Under a given condition, the matrix free method converges to the solution of frequency-domain Maxwell's equations, and it is particularly useful when conventional iterative solvers fail. Furthermore, the matrix free method only consumes a small amount of memory because only two sparse differentiation matrices need storing. Therefore, the matrix free method can be utilized to reduce the memory requirement of RC modeling, and this will be discussed in Chapter 5.

2.3 Summary

This chapter first reviewed existing RC modeling methods. It was found that a single numerical method was not efficient or flexible enough to achieve full-scale analysis of an RC. Among existing methods, the MoM is very suitable for the modeling of stirrers/antennas of an RC, but it incurs a heavy computational burden in modeling the large cavity. Recent advances in CEM were then studied, and their possible application in RC modeling was discussed. Among these new numerical methods, the DSC method can be used to reduce the computational burden in modeling a large cavity, and the matrix free method is useful for reducing the memory requirement. Furthermore, a hybrid technique is highly desirable for RC modeling because it can utilize the most powerful technique for every single component of an RC. The rest

of this thesis will develop a hybrid method combining the DSC method and MoM for efficient RC modeling. Meanwhile, the matrix free method will be applied in the hybrid method for memory-efficient modeling of RCs.

Chapter 3

Hybrid DSC-MoM Analysis of 2-D TM RCs

3.1 Introduction

During the historical development of RC, the 2-D TM RC was extensively studied due to its simplicity [16, 18, 29]. The 2-D case was usually considered in the early stage of new stirring or modeling methods. This is because the success in 2-D will lay a solid foundation for the development of 3-D methods.

In this chapter, a new hybrid technique combining the DSC method and the MoM is proposed for the efficient analysis of a 2-D TM RC. The metallic stirrer is viewed as a current sheet along whose surface the tangential electric field is forced to zero. The DSC method is used to model the cavity excited by the original source plus the current sheet, which are expressed on the grids of the DSC method using the regularization technique [96]. The MoM is used to enforce the boundary condition along the stirrer. Solutions from the above two steps are coupled together with the aid of the equivalence principle. The validity and advantage of the proposed hybrid technique is shown
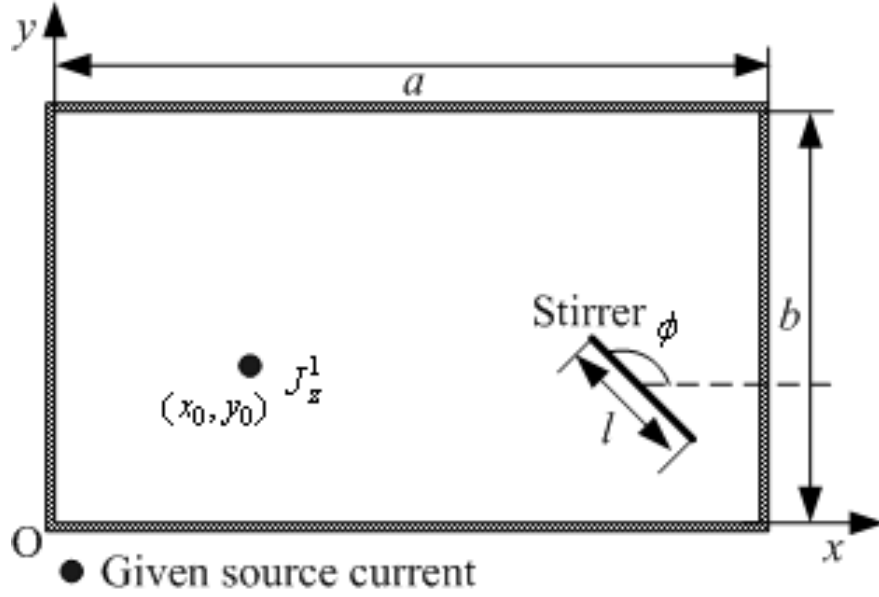
Figure 3.1: A 2-D TM RC with a metallic stirrer.

through comparisons with results from alternative methods. Taking advantage of the high efficiency of the DSC method, the new hybrid technique is shown to be a lot more efficient than a pure MoM with approximately the same memory cost.

The rest of this chapter is organized as follows. Section 3.2 describes the proposed hybrid technique in detail. Section 3.3 demonstrates the validity and efficiency of our hybrid technique through numerical simulations. Finally, Section 3.4 concludes the work described in this chapter.

3.2 Formulation

The problem considered is a 2-D TM RC shown in Figure 3.1. The dimension of the enclosure is $a \times b$ and the length of the stirrer is l. The rotating angle ϕ is defined as the angle between the stirrer and the positive x-direction. The RC is excited by a

line current source J_z^1 located at (x_0, y_0).

The rectangular cavity can be easily modeled with the DSC method. However, the rotating stirrer poses difficulty for structured grids, especially when coarse grids are required to achieve high efficiency. Therefore, we solve the problem in two steps. First, the stirrer is viewed as a current sheet J_z^2 and the DSC model is then obtained, as shown in Figure 3.2. Second, the tangential electric field along the stirrer is forced to zero with application of the MoM, and the MoM model shown in Figure 3.3 is obtained. To relate the two steps together, a Huygens' box S is placed around the stirrer in the MoM model, and the equivalence principle is used to couple solutions from the DSC method and MoM.

3.2.1 The DSC Model

In the DSC model, Maxwell's equations governing fields in the cavity are of the form:

$$H_x = -\frac{1}{j\omega\mu}\frac{\partial E_z}{\partial y}, \tag{3.1a}$$

$$H_y = \frac{1}{j\omega\mu}\frac{\partial E_z}{\partial x}, \tag{3.1b}$$

$$E_z = \frac{1}{j\omega\epsilon}\left(\frac{\partial H_y}{\partial x} - \frac{\partial H_x}{\partial y}\right) - \frac{1}{j\omega\epsilon}\left(J_z^1 + J_z^2\right). \tag{3.1c}$$

The computational domain is discretized by the standard Yee's cell [48] and the differential operators in (3.1) are approximated using the regularized Lagrange interpolation basis presented in [75]. For the completeness of this thesis, the regularized Lagrange interpolation basis is briefly introduced as follows. It should be mentioned that the two-dimensional or three-dimensional regularized Lagrange interpolation basis is the product of one-dimensional regularized Lagrange interpolation basis in each dimension. Therefore, only one-dimensional regularized Lagrange interpolation basis
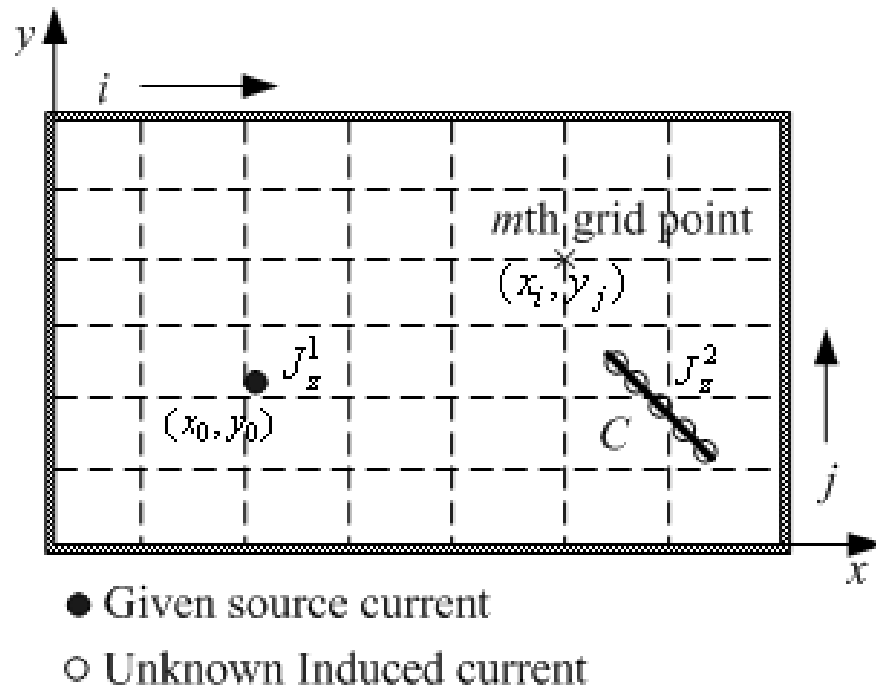
Figure 3.2: Illustration of the DSC model.
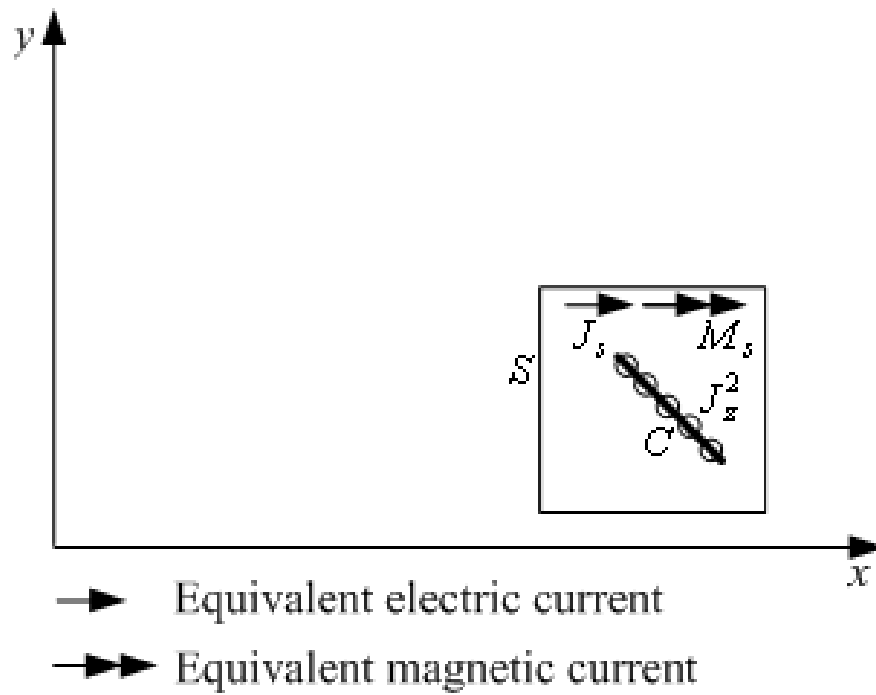
Figure 3.3: Illustration of the MoM model.
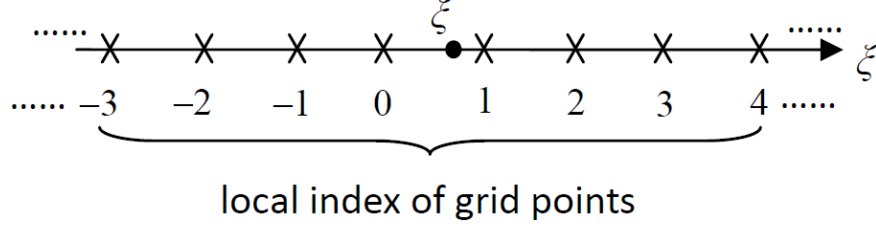
Figure 3.4: An arbitrary point along the ξ-axis (ξ can be x or y).

is described here. The one-dimensional Lagrange interpolation basis is

$$F_{M,k}(\xi) = \prod_{\substack{j=-M+1 \\ j \neq k}}^{M} \frac{(\xi - \xi_j)}{(\xi_k - \xi_j)}, \quad k = -M+1, \ldots -1, 0, 1, \ldots M, \tag{3.2}$$

where ξ can be x, y, or z. ξ_k is the kth grid point, and k is the local index of grid points, as shown in Figure 3.4. In order to improve its smoothness and localization, the Lagrange interpolation basis is multiplied by a Gaussian regularizer, and the regularized Lagrange interpolation basis is obtained

$$L_{M,k}(\xi) = F_{M,k}(\xi) \exp \left[-\frac{(\xi - \xi_k)^2}{2\sigma^2} \right], \tag{3.3}$$

where σ is used to control the bandwidth of the Gaussian envelop, and it is chosen to be $4\triangle_\xi$, as suggested in [74]. $\triangle_\xi$ is the grid size in the ξ-direction. The first and second order ordinary differentials of $L_{M,k}$ are

$$L'_{M,k}(\xi) = F'_{M,k}(\xi) \exp \left[-\frac{(\xi - \xi_k)^2}{2\sigma^2} \right] - L_{M,k}(\xi) \frac{(\xi - \xi_k)}{\sigma^2}, \tag{3.4}$$

$$L''_{M,k}(\xi) = F''_{M,k}(\xi) \exp \left[-\frac{(\xi - \xi_k)^2}{2\sigma^2} \right] - F'_{M,k}(\xi) \exp \left[-\frac{(\xi - \xi_k)^2}{2\sigma^2} \right] \frac{\xi - \xi_k}{\sigma^2}$$
$$- L'_{M,k}(\xi) \frac{(\xi - \xi_k)}{\sigma^2} - L_{M,k}(\xi) \frac{1}{\sigma^2}. \tag{3.5}$$

$F'_{M,k}$ and $F''_{M,k}$ can be calculated using the recursive algorithm provided in Appendix C of [97]. The interpolation polynomial in (3.2) gives the error level of $\triangle_\xi^{2M}$ [97]. Hence, the regularized Lagrange interpolation basis defined in (3.3) is called the $2M$-th order interpolation basis. If $M=1$ and σ is infinitely large, the regularized Lagrange interpolation function reduces to the linear interpolation function and the DSC method becomes the FD method.

Since J_z^1 exists at one point and J_z^2 distributes along a one-dimensional surface [96], they are hard to be resolved by the structured grids in the DSC method. Fortunately, the regularization technique [96] can be used to express these singular currents on the structured grids of the DSC method. Take J_z^2 as an example. In Figure 3.2, J_z^2 is a singular electric current distributing along the stirrer's contour C, which is a one-dimensional continuous surface in a two-dimensional space. Using the regularization technique, the regularized form of J_z^2 at the mth grid point (x_i, y_j) is [96]

$$J_{zR}^2(x_i, y_j) = \int_C \zeta_\epsilon(x_i - x_c)\zeta_\epsilon(y_j - y_c)J_z^2(x_c, y_c)dl, \qquad (3.6)$$

where (x_c, y_c) is a point on C and $J_z^2(x_c, y_c)$ is the value of the induced current at point (x_c, y_c). ζ_ϵ represents the regularized Dirac function, whose definition is [96]

$$\zeta_\epsilon(\xi_i - \xi_c) = \left[\begin{array}{cc} 1 - 0.5|d| - |d|^2 + 0.5|d|^3, & \text{if } d \leq 1 \\ 1 - \frac{11}{6}|d| + |d|^2 - \frac{1}{6}|d|^3, & \text{if } 1 \leq d \leq 2 \\ 0, & \text{otherwise} \end{array} \right], \qquad (3.7)$$

where

$$d = \frac{\xi_i - \xi_c}{\triangle_\xi}, \qquad (3.8)$$

and ξ can be either x or y. The validity of the above regularization has been demonstrated both theoretically and numerically in [96] and is hence adopted in our work. Because J_z^2 is unknown, it is first expanded using the pulse basis as

$$J_z^2 = \sum_{l=1}^{NC} \zeta(x - x_l, y - y_l)s_l, \tag{3.9}$$

where ζ represents the Dirac function and s_l is the value of J_z^2 at point (x_l, y_l). Substituting the current expansion (3.9) into (3.6) and replacing the integral in (3.6) with a trapezoidal rule, we have

$$J_{zR}^2(x_i, y_j) = \triangle \sum_{l=1}^{NC} \zeta_\epsilon(x_i - x_l)\zeta_\epsilon(y_j - y_l)s_l, \tag{3.10}$$

whose matrix form is

$$\mathbf{j}_{zR}^2 = \mathbf{Rs}, \tag{3.11}$$

where $\mathbf{s}$ is the vector constituted by the expansion coefficients of J_z^2 and $\triangle$ is the sampling step on C. $\mathbf{R}$ is named as the regularization matrix whose elements are

$$R(m, n) = \zeta_\epsilon(x_i - x_n)\zeta_\epsilon(y_j - y_n)\triangle, \tag{3.12}$$

where i and j are the indices of the mth DSC grid point in the x and y directions, respectively. (x_n, y_n) is the coordinate of the nth sampled point on C. The case of J_z^1 is much simpler because it is known and exists at only one point. With a similar procedure, the regularized value of J_z^1 on the mth grid point is

$$j_{zR}^1(m) = \zeta_\epsilon(x_i - x_0)\zeta_\epsilon(y_j - y_0)v_z^1, \tag{3.13}$$

where v_z^1 is the value of J_z^1. Following the approximation of differential operators presented in [75] and expressing the singular sources with (3.11) and (3.13), (3.1) is transformed into the following linear equations

$$\mathbf{h}_x = -\frac{1}{j\omega\mu}\mathbf{A}_x\mathbf{e}_z, \qquad (3.14a)$$

$$\mathbf{h}_y = \frac{1}{j\omega\mu}\mathbf{A}_y\mathbf{e}_z, \qquad (3.14b)$$

$$\mathbf{e}_z = \frac{1}{j\omega\epsilon}\left(\mathbf{B}_y\mathbf{h}_y - \mathbf{B}_x\mathbf{h}_x\right) - \frac{1}{j\omega\epsilon}\left(\mathbf{j}_{zR}^1 + \mathbf{Rs}\right), \qquad (3.14c)$$

where $\mathbf{h}_x$, $\mathbf{h}_y$ and $\mathbf{e}_z$ are unknown vectors constituted by the values of H_x, H_y and E_z at grid points, respectively. Matrices $\mathbf{A}_x$, $\mathbf{A}_y$, $\mathbf{B}_x$ and $\mathbf{B}_y$ are differentiation matrices [97] resulting from the differential of the Lagrange interpolation basis. These matrices are highly sparse and can be filled efficiently with a recursive procedure [97]. Details about the calculation of differentiation matrices can be found in Appendix A.1.

3.2.2   The MoM Model

In the DSC model, the effect of the induced current along the stirrer is considered as a secondary source for the large cavity. However, the boundary condition along the surface of the conducting stirrer is not satisfied. In order to force the tangential field along the stirrer to zero, we first substitute the current expansion (3.9) into the 2-D TM EFIE

$$\frac{4}{\omega\mu}E_z^i(\vec{r}) = \int_C J_z(\vec{r}')H_0^{(2)}(k\,|\vec{r} - \vec{r}'|)d\vec{r}' \qquad (3.15)$$

and then invoke the point matching process upon it. Finally, we have

$$\frac{4}{\omega\mu}E_z^i(\vec{r}_m) = \sum_{n=1}^{NC} s_n \int_{C_n} H_0^{(2)}(k\,|\vec{r}_m - \vec{r}'|)d\vec{r}', \qquad (3.16)$$

whose matrix form becomes

$$\frac{4}{\omega\mu}\mathbf{e}_z^i = \mathbf{L}\mathbf{s}, \tag{3.17}$$

where $\mathbf{e}_z^i$ is the incident field vector and $H_0^{(2)}$ is the second kind Hankel function of order zero. $\mathbf{L}$ is the interaction matrix defined as

$$L(m,n) = \int_{C_n} H_0^{(2)}(k\,|\vec{r}_m - \vec{r}'|)d\vec{r}'. \tag{3.18}$$

When filling the matrix $\mathbf{L}$, the problem of singularity is encountered when $|m - n| \leq 1$ and it is circumvented through the small argument approximation to the Hankel function [98].

3.2.3 Hybridization

In order to find the unknown incident field E_z^i on the stirrer, a Huygens' box S is placed around the stirrer, as shown in Figure 3.3. Along the surface of Huygens' box, tangential electric and magnetic fields should be continuous. The Huygens' box is not required to be conformal with Yee's grid used in DSC because interpolation can be used to obtain field information on Huygens' box. The equivalent currents across the box can be viewed as sources of E_z^i. The equivalent currents are related to the total fields as

$$\vec{J}(\vec{r}_S) = \hat{n} \times \vec{H}(\vec{r}_S), \ \ \vec{M}(\vec{r}_S) = -\hat{n} \times \vec{E}(\vec{r}_S), \tag{3.19}$$

where $\hat{n}$ is the unit normal vector inwards to the surface of the box, and $\vec{H}(\vec{r}_S)$ and $\vec{E}(\vec{r}_S)$ are the total fields across the box.

Since unknown vectors $\mathbf{h}_x$, $\mathbf{h}_y$ and $\mathbf{e}_z$ in (3.14) are defined by the values of total fields at grid points, $\vec{H}(\vec{r}_S)$ and $\vec{E}(\vec{r}_S)$ across the box can be computed using the unknown vectors in (3.14) through interpolation. Hence, we obtain

$$\mathbf{h}_x^b = \mathbf{W}_x \mathbf{h}_x, \ \ \mathbf{h}_y^b = \mathbf{W}_y \mathbf{h}_y, \ \ \mathbf{e}_z^b = \mathbf{W}_z \mathbf{e}_z, \tag{3.20}$$

where those vectors with superscript b consist of field quantities on the Huygens' box and matrices $\mathbf{W}$ are interpolation matrices filled with the values of interpolating polynomials. Elements of these interpolation matrices are defined in Appendix B.1.

From (3.19) and (3.20), the equivalent currents on the box are related to the unknown vectors $\mathbf{h}_x$, $\mathbf{h}_y$, and $\mathbf{e}_z$ in (3.14) as:

$$\mathbf{j}_z^b = \mathbf{T}_{xz} \mathbf{W}_x \mathbf{h}_x + \mathbf{T}_{yz} \mathbf{W}_y \mathbf{h}_y, \tag{3.21a}$$

$$\mathbf{m}_x^b = \mathbf{T}_{zx} \mathbf{W}_z \mathbf{e}_z, \ \ \mathbf{m}_y^b = \mathbf{T}_{zy} \mathbf{W}_z \mathbf{e}_z, \tag{3.21b}$$

where $\mathbf{j}_z^b$, $\mathbf{m}_x^b$, and $\mathbf{m}_y^b$ are vectors consisting of the equivalent electric and magnetic currents across the box. Matrices $\mathbf{T}$ represent the translation from fields to equivalent currents and they can be obtained from (3.19) as follows. For the TM case, the z-component of the magnetic field is zero, and x- and y-components of the electric field are zero. Meanwhile, the unit vector $\hat{n}$ has no z-directed component. Therefore, (3.19) can be written as

$$J_z(\vec{r}_S) = \hat{n}_x(\vec{r}_S) H_y(\vec{r}_S) - \hat{n}_y(\vec{r}_S) H_x(\vec{r}_S), \tag{3.22a}$$

$$M_x(\vec{r}_S) = -\hat{n}_y(\vec{r}_S) E_z(\vec{r}_S), \tag{3.22b}$$

$$M_y(\vec{r}_S) = \hat{n}_x(\vec{r}_S) E_z(\vec{r}_S), \tag{3.22c}$$

35

where $\hat{n}_x$ and $\hat{n}_y$ denote the x- and y-components of the unit vector $\hat{n}$, respectively. From (3.22a), one can have

$$T_{xz}(m,n) = \begin{bmatrix} -\hat{n}_y(\vec{r}_S^{\,m}), & \text{if } m = n \\ 0, & \text{otherwise} \end{bmatrix}, \tag{3.23}$$

and

$$T_{yz}(m,n) = \begin{bmatrix} \hat{n}_x(\vec{r}_S^{\,m}) & \text{if } m = n \\ 0, & \text{otherwise} \end{bmatrix}, \tag{3.24}$$

where $\vec{r}_S^{\,m}$ denotes the vector position of the mth point on Huygens' box. From (3.22b) and (3.22c), matrices $\mathbf{T}_{zx}$ and $\mathbf{T}_{zy}$ can be defined as

$$T_{zx}(m,n) = \begin{bmatrix} -\hat{n}_y(\vec{r}_S^{\,m}), & \text{if } m = n \\ 0, & \text{otherwise} \end{bmatrix}, \tag{3.25}$$

and

$$T_{zy}(m,n) = \begin{bmatrix} \hat{n}_x(\vec{r}_S^{\,m}), & \text{if } m = n \\ 0, & \text{otherwise} \end{bmatrix}. \tag{3.26}$$

Once we have the equivalent currents across the Huygens' box, the magnetic vector potential $\vec{A}$ and electric vector potential $\vec{F}$ from the equivalent currents are calculated as:

$$\vec{A}(\vec{r}) = -\frac{j\mu}{4} \int \int_S \vec{J}(\vec{r}') H_0^{(2)}(k|\vec{r} - \vec{r}'|) d\vec{r}', \tag{3.27a}$$

$$\vec{F}(\vec{r}) = -\frac{j\epsilon}{4} \int \int_S \vec{M}(\vec{r}') H_0^{(2)}(k|\vec{r} - \vec{r}'|) d\vec{r}'. \tag{3.27b}$$

For the 2-D TM case, the electric field is related to the vector potentials through the

following equation

$$\vec{E} = -j\omega\vec{A} - \frac{1}{\epsilon}\nabla \times \vec{F}. \tag{3.28}$$

Therefore, the electric field illuminating the stirrer is

$$E_z^i = -\frac{\omega\mu}{4} \int\int_S J_z^b(\vec{r}')H_0^{(2)}(k|\vec{r}-\vec{r}'|)d\vec{r}' + \frac{j}{4}\int\int_S M_y^b(\vec{r}')\frac{\partial H_0^{(2)}(k|\vec{r}-\vec{r}'|)}{\partial x}d\vec{r}'$$
$$-\frac{j}{4}\int\int_S M_x^b(\vec{r}')\frac{\partial H_0^{(2)}(k|\vec{r}-\vec{r}'|)}{\partial y}d\vec{r}'. \tag{3.29}$$

Invoking a point matching process upon both sides of equation (3.29), one can obtain

$$\mathbf{e}_z^i = \mathbf{Z}_{xz}\mathbf{m}_x^b + \mathbf{Z}_{yz}\mathbf{m}_y^b + \mathbf{Z}_{zz}\mathbf{j}_z^b, \tag{3.30}$$

where matrices $\mathbf{Z}$ represent the relationship between fields and currents and their elements are given as:

$$Z_{xz}(m,n) = -\frac{j}{4}\frac{\partial H_0^{(2)}(k|\vec{r}_m-\vec{r}_n|)}{\partial y}\triangle, \tag{3.31a}$$

$$Z_{yz}(m,n) = \frac{j}{4}\frac{\partial H_0^{(2)}(k|\vec{r}_m-\vec{r}_n|)}{\partial x}\triangle, \tag{3.31b}$$

$$Z_{zz}(m,n) = -\frac{\omega\mu}{4}H_0^{(2)}(k|\vec{r}_m-\vec{r}_n|)\triangle, \tag{3.31c}$$

where $\triangle$ is the sampling step size on S and the derivatives of the Hankel function are

$$\frac{\partial H_0^{(2)}(k|\vec{r}_m-\vec{r}_n|)}{\partial x} = -kH_1^{(2)}(k|\vec{r}_m-\vec{r}_n|)\frac{x_m-x_n}{|\vec{r}_m-\vec{r}_n|},$$

$$\frac{\partial H_0^{(2)}(k|\vec{r}_m-\vec{r}_n|)}{\partial y} = -kH_1^{(2)}(k|\vec{r}_m-\vec{r}_n|)\frac{y_m-y_n}{|\vec{r}_m-\vec{r}_n|},$$

where $H_1^{(2)}$ is the second kind Hankel function of order one.

From (3.21), (3.30), and the first two equations of (3.14), we have

$$\mathbf{e}_z^i = \mathbf{N}\mathbf{e}_z, \tag{3.32}$$

where

$$\mathbf{N} = \mathbf{Z}_{xz}\mathbf{T}_{zx}\mathbf{W}_z + \mathbf{Z}_{yz}\mathbf{T}_{zy}\mathbf{W}_z - \frac{1}{j\omega\mu}\mathbf{Z}_{zz}(\mathbf{T}_{xz}\mathbf{W}_x\mathbf{A}_x - \mathbf{T}_{yz}\mathbf{W}_y\mathbf{A}_y).$$

Eliminating $\mathbf{h}_x$ and $\mathbf{h}_y$ in (3.14c) using (3.14a) and (3.14b), and combining (3.14c) with (3.17) through (3.32), we obtain

$$\begin{bmatrix} \dfrac{4}{\omega\mu}\mathbf{N} & -\mathbf{L} \\ \mathbf{M} & \dfrac{1}{j\omega\epsilon}\mathbf{R} \end{bmatrix} \begin{bmatrix} \mathbf{e}_z \\ \mathbf{s} \end{bmatrix} = \begin{bmatrix} \mathbf{0} \\ -\dfrac{1}{j\omega\epsilon}\mathbf{j}_{zR}^1 \end{bmatrix}, \tag{3.33}$$

where

$$\mathbf{M} = \mathbf{I} + \frac{1}{\omega^2\mu\epsilon}\left(\mathbf{B}_x\mathbf{A}_x + \mathbf{B}_y\mathbf{A}_y\right).$$

For RC simulation, matrix $\mathbf{L}$ is usually of small scale because the electrical size of a stirrer is much smaller than that of the chamber. Therefore, we may eliminate $\mathbf{s}$ in (3.33) and derive the following matrix equation with respect to $\mathbf{e}_z$:

$$\left[\mathbf{M} + \frac{4}{j\omega^2\mu\epsilon}\mathbf{R}\mathbf{L}^{-1}\mathbf{N}\right]\mathbf{e}_z = -\frac{1}{j\omega\epsilon}\mathbf{j}_{zR}^1. \tag{3.34}$$

Equation (3.34) has impressed all the excitations and imposed all the boundary conditions. Therefore, we can obtain the unique solution of E_z by solving (3.34). Once E_z is obtained, all the other field components as well as the induced current can be computed accordingly. Since iterative solvers encounter convergence problems in RC simulation [23], a Gaussian elimination procedure provided by MATLAB® is used for

solving (3.34) in this chapter.

In the proposed hybrid method, radiated fields of equivalent currents are calculated on stirrer's surface. It is known that there is a singularity problem if a field point is very close to the source point. Furthermore, fields vary very rapidly when the observation points are near the source points, which incurs difficulty for accurate numerical calculation of radiated fields. In order to avoid the mentioned singularity and retain high accuracy, the surface of Huygens' box should be selected at some distance away from the stirrer. On the other hand, computational load increases as the size of Huygens' box becomes big.

It is difficult to derive a general rule for the optimal value of the box size since the optimal value is dependent on the shape of the stirrer. A simple criterion for determining the box size is to ensure that the minimum distance between Huygens' box and stirrer is larger than the DSC grid size. This choice not only avoids the singularity problem but also facilitates accurate numerical calculation of fields radiated by the equivalent currents.

3.3   Numerical Results

To show the validity of the proposed method, simulations are conducted and our results are compared with those from alternative methods. CPU time and memory requirement is also compared to show the advantage of our method. For the pure MoM, the pulse basis and point matching [98] are used, and the spatial sampling density is chosen to be at least one tenth λ, where λ is the wavelength at the frequency of interest for single frequency analysis. According to [75], grid sizes in the DSC method are chosen to be around one sixth λ. For wide frequency range analysis, frequency

sweep with uniform frequency step $\triangle f$ is used, and λ is determined as the wavelength at the highest frequency. All the simulations presented in this section are conducted on a personal computer with 2.66 GHz CPU and 2 GB RAM.
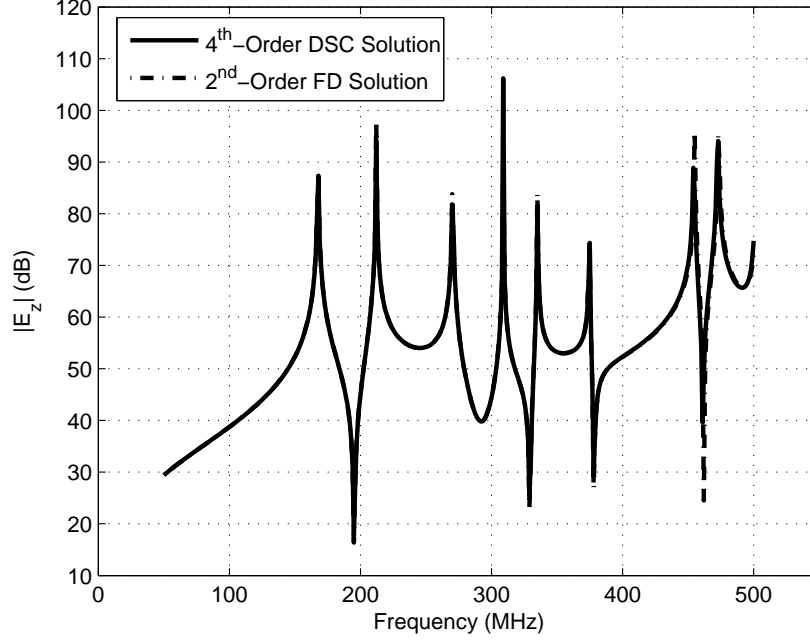
Figure 3.5: Magnitude of E_z at point (0.8 m,0.8 m) with a current source of 1 A/m^2 at point (0.53 m,0.5 m) in a 2-D TM cavity of dimension 3 m×1 m.

3.3.1 DSC Modeling of a 2-D TM Cavity

First, the high efficiency of the DSC method is shown through numerical simulations on a 2-D TM cavity. Geometry of the 2-D TM cavity is the same as that of the 2-D TM RC shown in Figure 3.1, except for that the stirrer is removed. The cavity is of dimension 3 m × 1 m, and it is excited by a current source placed at (0.53 m,0.5 m). Amplitude of the current source is 1 A/m^2.

Figure 3.5 illustrates the solution to the magnitude of E_z at point (0.8 m,0.8 m). The frequency range is from 50 MHz to 500 MHz. Good agreement is observed

between solutions from the fourth-order DSC method (M=2) and the FD method (M=1, σ=10^8). There are some differences at the sharp resonant frequency points. This is because fields change very rapidly near these points and they are hence hard to be accurately computed. It should be noted that, the grid size used in the DSC method is 0.1 m. Therefore, without the application of regularization technique, the source placed at (0.53 m,0.5 m) can not be captured using such coarse grids. Table 3.1 presents comparison of time and memory requirement between the fourth-order DSC method and the second-order FD method. The memory cost results are obtained from the MATLAB Profiler [99]. Obviously, the DSC method requires much less unknowns and it is more efficient than the FD method.

Table 3.1: Comparison Between DSC and FD methods for Analyzing the 2-D TM Cavity at One Frequency Point

Method	Grid Size	Number of Unknowns	CPU Time	Memory Usage
DSC method	0.1 m	300	4.7 seconds	12 KB
FD method	0.025 m	4800	60.2 seconds	120 KB

3.3.2 Analysis of a 2-D TM Cavity with a Small Cylinder

The high efficiency of the DSC method was demonstrated in Section 3.3.1. In order to examine the performance of the hybrid method, a 2-D TM cavity with a small square cylinder is considered in this section. Figure 3.6 illustrates the geometry and dimensions of this test model. The side length of the cylinder is 1 mm. The structure is excited by a line current source of amplitude 1 A/m^2, whose location is noted in Figure 3.6. We choose this test model because the induced current on the cylinder has been computed and reported by De Zutter et al. [29]. Since the cylinder is small, it is hard to resolve it with the coarse grids used in the DSC method. However, our
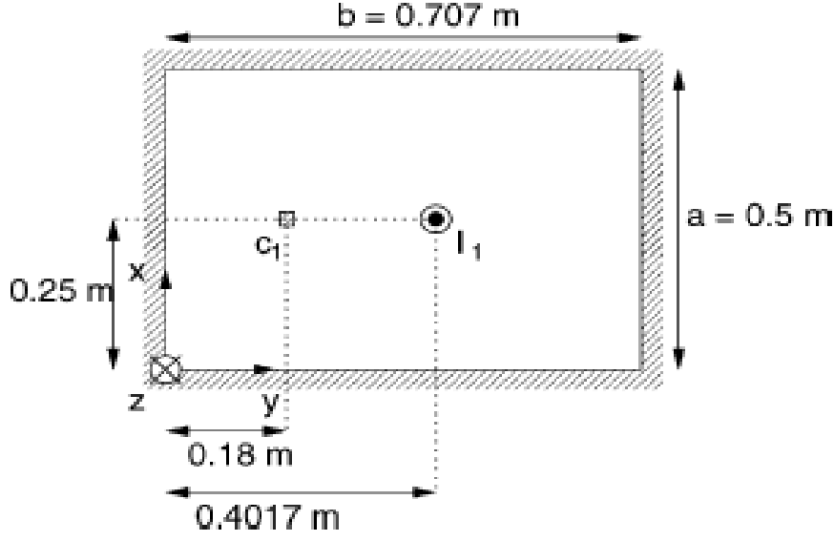
Figure 3.6: Geometry of a 2-D TM cavity with a small square cylinder inside.

hybrid technique can model this structure easily. In the hybrid method, the Huygens'
box is a square with side length 5 cm, which is concentric with the cylinder.

Figure 3.7 shows the induced current J_z^2 on the cylinder over two frequency ranges.
Good agreement is observed between our results and those from the pure MoM, as
well as published ones. In both our method and the pure MoM, the small cylinder
is described using four pulse bases. In the pure MoM, grid sizes of $d_x = 2.94$ cm and
$d_y = 2.95$ cm, leading to 86 unknowns, are adopted for the low frequency range, where
d_x and d_y represent spatial steps used to model the x-directed and y-directed cavity
walls, respectively. For the higher frequency range, $d_x = 1.85$ cm and $d_y = 1.86$ cm
are used, leading to 134 unknowns. In the DSC implementation, $\triangle_x = 2.5$ cm and
$\triangle_y = 2.52$ cm are adopted for both frequency ranges, and the number of unknowns is
513. Over the low frequency range, our method takes about 48 seconds with a fourth-
order DSC, while a pure MoM requires about 180 seconds. The advantage of the hybrid
technique is not significant over the low frequency range. For the higher frequency
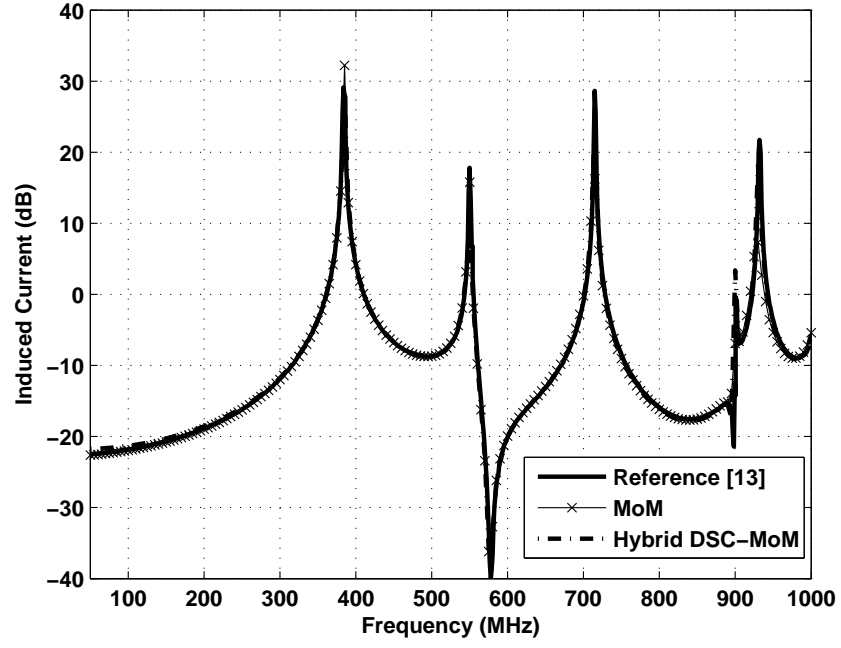
(a) 50-1000 MHz
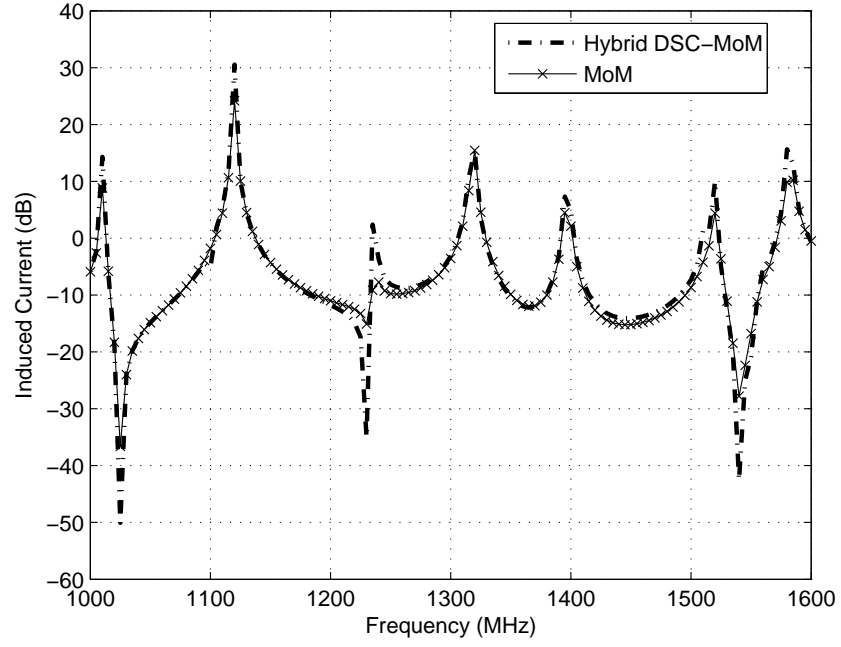
(b) 1000-1600 MHz

Figure 3.7: Current induced on the small cylinder in two frequency ranges ($\triangle f = 5$ MHz).

43

Table 3.2: Time and Memory Cost Comparisons Between Our Hybrid Technique and a Pure MoM for One Stirrer Position

Frequency range	Methods	Number of field points	CPU time	Memory	Grid size
200 MHz	Pure MoM	41	5 seconds	2 MB	$d_x = 0.1$ m, $d_y = 0.0996$ m
		201	7.8 seconds	2 MB	$d_x = 0.1$ m, $d_y = 0.0996$ m
	Our method	201	0.8 second	2 MB	$\triangle_x = 0.25$ m, $\triangle_y = 0.2525$ m
50-200 MHz	Pure MoM	1	625 seconds	2 MB	$d_x = 0.1$ m, $d_y = 0.0996$ m
	Our method	1	84 seconds	2 MB	$\triangle_x = 0.25$ m, $\triangle_y = 0.2525$ m

range, the mesh size for the pure MoM should be reduced and the computation time increases dramatically to about 310 seconds. However, with our hybrid method, the same mesh can be used for the DSC method and the computation time is 36 seconds. It should be mentioned that comparison with MoM adopting the cavity Green's function [29] is not made because the information about CPU time was not reported in [29].

3.3.3 Modeling of a 2-D TM RC

A 2-D TM RC is simulated in this section. Geometry of the 2-D TM RC is shown in Figure 3.1. Its dimensions are: $a = 5$ m, $b = 7.07$ m, $l = 0.5$ m, $x_0 = 3$ m, and $y_0 = 3.5$ m. Furthermore, the middle point of the stirrer is located at the point (3 m, 2 m) and the current source is of 1 A/m².

At the frequency $f = 200$ MHz, magnitudes of E_z along two lines are calculated and plotted in Figure 3.8 and Figure 3.9 for different rotating angles ϕ. A wide frequency range analysis, usually required in RC modeling, is also conducted and magnitudes of E_z at the point (2 m, 4 m) from 50 to 200 MHz are plotted in Figure 3.10 for

(a) $\phi = 0^o$

(b) $\phi = 45^o$
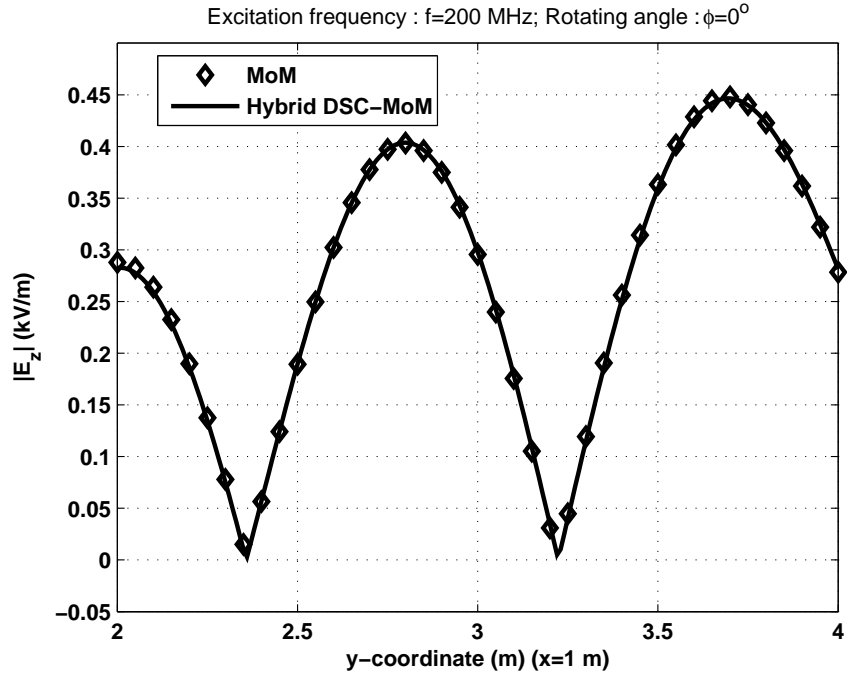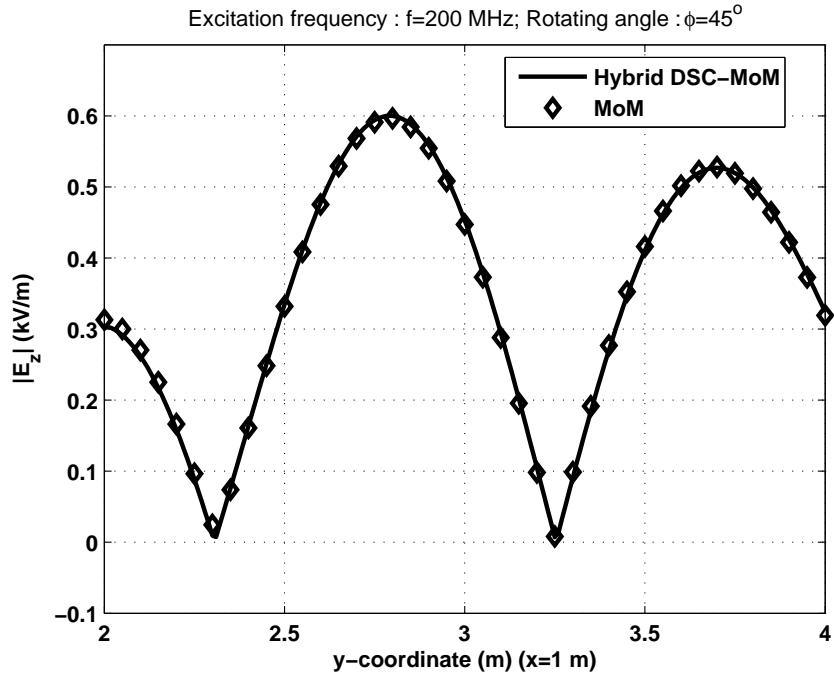
Figure 3.8: Observed $|E_z|$ along the line between two points (1 m, 2 m) and (1 m, 4 m) for different rotating angles.

(a) $\phi = 0^o$

(b) $\phi = 45^o$
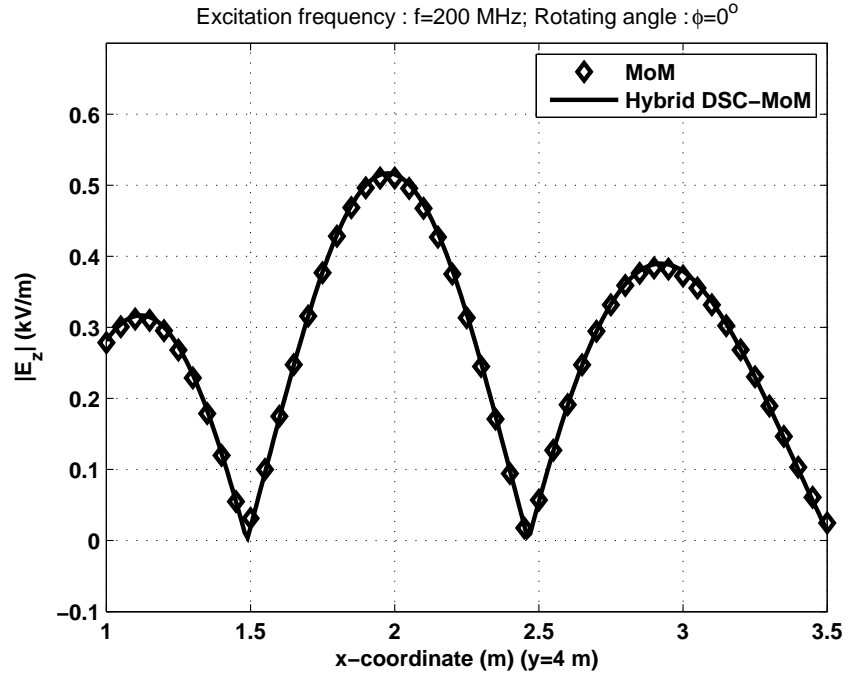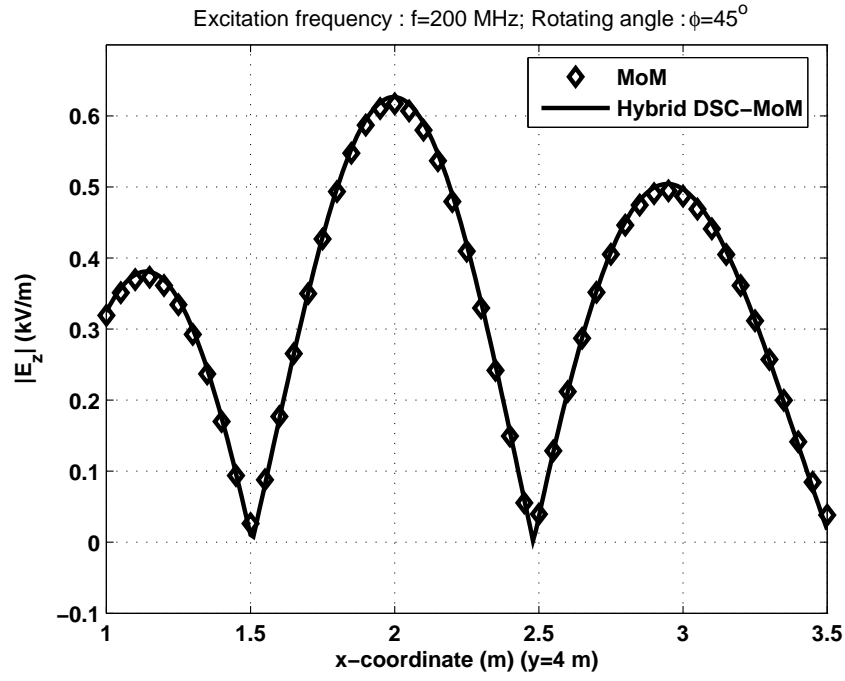
Figure 3.9: Observed $|E_z|$ along the line between two points (1 m, 4 m) and (3.5 m, 4 m) for different rotating angles.

(a) $\phi = 0^o$

(b) $\phi = 45^o$
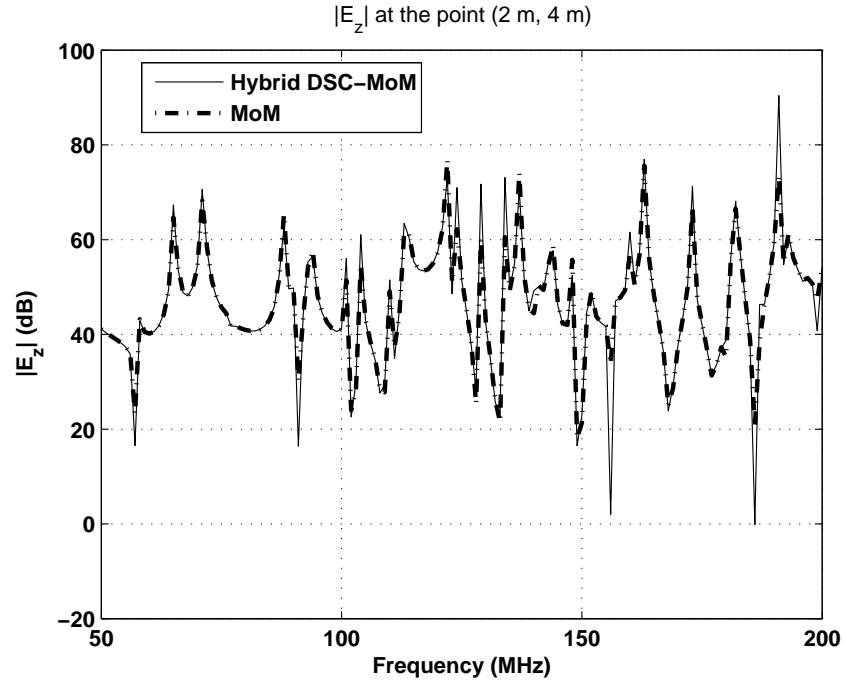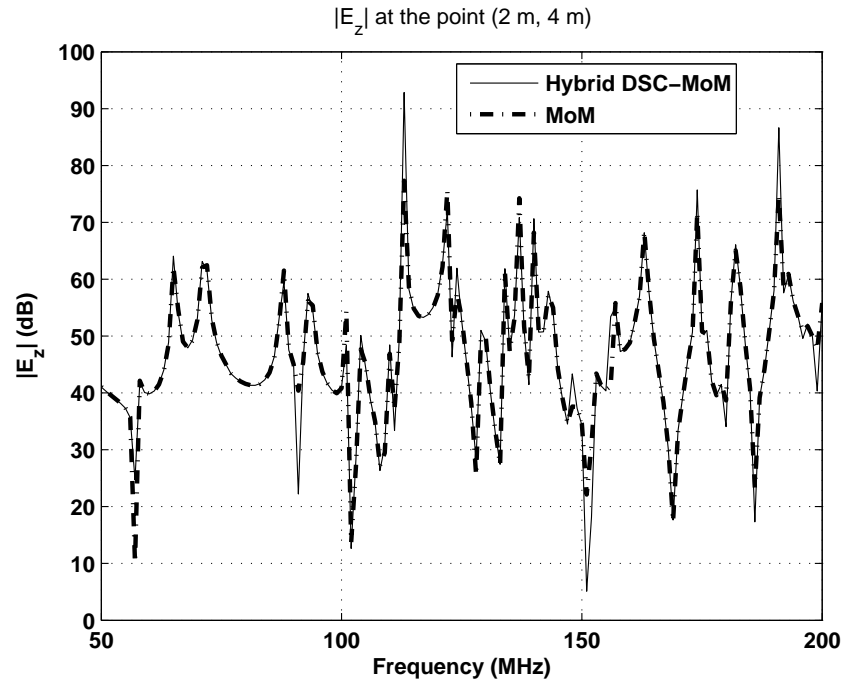
Figure 3.10: Observed $|E_z|$ at the point (2 m, 4 m) from 50 MHz to 200 MHz ($\triangle f = 1$ MHz) for different rotating angles.

two stirrer positions. In all these cases, our results agree well with those from a pure MoM.

513 and 261 unknowns are used in our proposed method and the pure MoM, respectively. Table 3.2 compares the time and memory cost between our hybrid technique and the pure MoM. Table 3.2 also shows the grid sizes used for modeling the cavity. To make the efficiency comparisons more convincing, the stirrer is modeled with 20 pulse bases in both our method and the pure MoM. It is seen that memory requirements of our method and a pure MoM are approximately the same. This is because memory cost in our method is mainly determined by inverting the left-hand side matrix of (3.34), which is not as sparse as the differentiation matrices. However, our method is at least six times as fast as a pure MoM. Moreover, it is observed that when the number of field points is increased from 41 to 201, computation time with the pure MoM is increased by more than 50%. This is because when the number of field points is large, computation of the Hankel function and integration on the current will incur a heavy extra computational load in the MoM. However, in our hybrid technique, only simple interpolation is needed and little extra computation will be introduced for the near-field computation. Hence, when the number of field points is the same, our method is nearly ten times as fast as a pure MoM.

Finally, in order to illustrate the efficiency of our proposed method in modeling a large RC, we also show the results obtained at higher frequencies. Wide frequency range analysis of the 2-D TM RC is conducted from 350 to 500 MHz. At the frequency of 500 MHz, the chamber is of electrical size 8.3 $\lambda \times$ 11.8 λ. The magnitudes of E_z for two stirrer positions are plotted in Figure 3.11. It is observed that the magnitude of E_z is strongly dependent on ϕ at these higher frequencies. For this problem, $\triangle_x$ and $\triangle_y$ are chosen to be 0.1 m and 0.0996 m, respectively, and the interpolation basis used
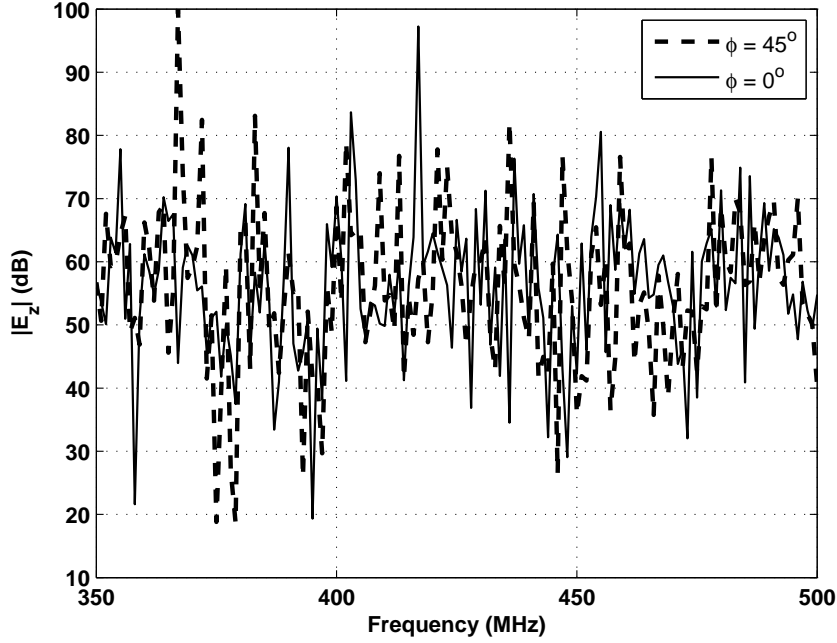
Figure 3.11: Observed $|E_z|$ at the point (2 m, 4 m) from 350 MHz to 500 MHz ($\triangle f = 1$ MHz) for different rotating angles.

is of order 12. The stirrer is modeled with 20 pulse bases. The number of unknowns is 3430. In modeling this large RC, the CPU time by our proposed method is 610 seconds for one stirrer position. With the same number of frequency points, modeling the large RC with our proposed method requires even less CPU time than modeling the smaller RC with a pure MoM (cf. Table 3.2).

3.4 Concluding Remarks

In this chapter, a hybrid technique has been proposed for efficient modeling of a 2-D TM RC. We have considered the stirrer as a current sheet where tangential electric fields are enforced to be zero. The original problem is then decomposed into two sub-problems. One is a large cavity excited by the original source in addition to the current sheet, which is modeled using the DSC method. The other is to enforce the

tangential fields along the stirrer to be zero, and it is solved with the MoM. The two sub-problems are coupled together through the equivalence principle and they are solved simultaneously.

Numerical results have been presented to show the validity and advantage of the proposed method. The high efficiency of the DSC method was first shown through comparison with the FD method. Advantages of the proposed hybrid method was demonstrated through comparisons with a pure MoM. In all the simulations, results from the hybrid method agree well with those from the pure MoM as well as published ones. Taking advantage of the DSC method's high efficiency, the proposed hybrid technique is shown to be much more efficient than a pure MoM with approximately the same memory cost. Another advantage of the hybrid method is the efficient computation of fields at a large number of points with simple interpolation. On the other hand, computation of a Hankel function and integration on the current are required in a pure MoM for a near-field computation, which will be time consuming when the number of near-field points is large. Furthermore, the proposed hybrid method overcame the inflexibility of the DSC method by modeling arbitrarily shaped structures using MoM. It was shown that the small square cylinder and the arbitrarily aligned stirrer could be easily modeled using the proposed hybrid method.

The high efficiency and flexibility of the 2-D hybrid method justify its promising potential for 3-D RC modeling. A 3-D hybrid technique combining the DSC method and MoM will be developed in the next chapter.

Chapter 4

Efficient Modeling of 3-D Medium-Sized RCs Using Hybrid DSC-MoM

4.1 Introduction

In Chapter 3, a 2-D hybrid DSC-MoM technique was developed and its advantages were demonstrated. This chapter presents a 3-D hybrid DSC-MoM method for efficient modeling of 3-D medium-sized RCs.

Similar to the 2-D case, the 3-D large cavity is efficiently modeled by the DSC method, and the stirrer is simulated by the flexible MoM. Different from the 2-D case, the triangular mesh is utilized to discretize the stirrer and the Huygens' box, and the RWG basis is adopted to expand the induced current on the stirrer and the equivalent current along Huygens' box. Exploiting the property of RWG basis, solutions from the two methods are combined together using the equivalence principle. The validity and advantages of the proposed 3-D hybrid technique are shown through comparisons with

51

the commercial software FEKO. Employing the high efficiency of the DSC method, the hybrid technique can analyze one stirrer position of a medium-sized RC in a few hundred seconds on a single personal computer, for which FEKO needs thousands of seconds CPU time. The memory requirement of the proposed method is also less than that of FEKO. Furthermore, our hybrid method provides efficient calculation of electric field strength at a large number of field points, which is of great interest in RC analysis. Simulations show that our method only takes 1.7 seconds to compute electric field strength at 4026 field points.

The rest of this chapter is organized as follows. Section 4.2 describes the proposed hybrid technique in detail. Section 4.3 demonstrates the validity and efficiency of our hybrid technique through numerical examples. Finally, Section 4.4 concludes the work described in this chapter.

4.2　Formulation

Figure 4.1 shows a 3-D RC, which consists of a large metallic cavity of $L_x \times L_y \times L_z$, and a mechanical stirrer S. A transmitting antenna is positioned at a corner of the RC. In practice, the transmitting antenna can be a horn or a log-periodic antenna. For simplicity, the transmitting antenna is replaced by a current source $\vec{J}_0$ in this work, which doesn't affect the analysis of the RC itself.

Similar to the 2-D case, the 3-D RC modeling can be decomposed into two sub-problems. The first is to force the tangential electric field along the surface of the stirrer to zero, which results in an integral equation. The second one is a large cavity excited by the original current source $\vec{J}_0$ and a current sheet $\vec{J}_S$, where $\vec{J}_S$ is the induced current on the stirrer. The first and second subproblems are solved using the
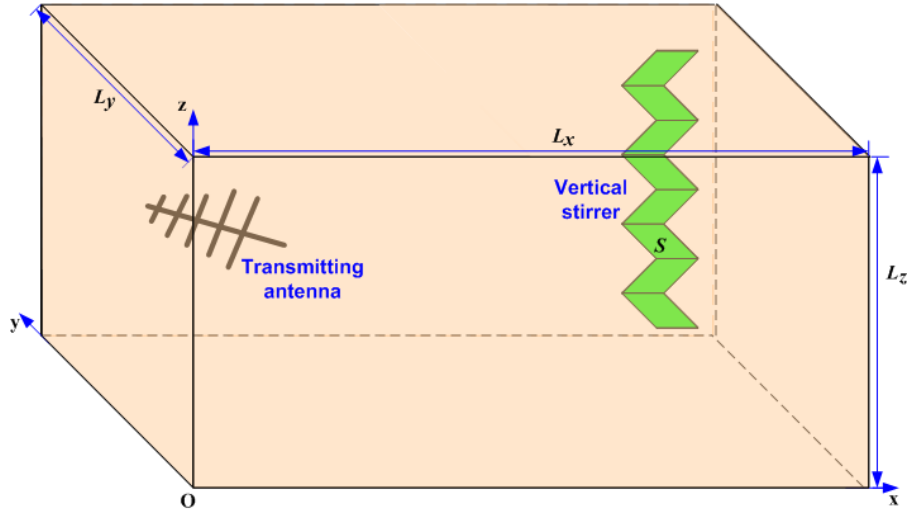
Figure 4.1: Geometry of a typical 3-D reverberation chamber.

MoM and the DSC method, respectively. As shown in Figure 4.2, by enclosing the stirrer with a Huygens' box S_b, the field impinging the stirrer is exactly the radiated field by the equivalent electric current $\vec{J}_b$ and magnetic current $\vec{M}_b$ along the Huygens' box. At the same time, $\vec{J}_b$ and $\vec{M}_b$ are related to the field solution of the second subproblem through the equivalence principle. The two subproblems are thus coupled together. By solving the two subproblems simultaneously, the induced current as well as the fields in the RC can be obtained.

4.2.1 The MoM Model

Figure 4.2 illustrates the MoM model. The conducting stirrer is illuminated by the radiated fields of the equivalent current along Huygens' box. In order to enforce the tangential electric field along the stirrer surface to zero, the following 3-D EFIE is applied along S

$$\hat{t}\left(\vec{r}\right) \cdot \int\int_S \left(1 + \frac{1}{k^2}\nabla\nabla\cdot\right) \vec{J}_S\left(\vec{r}'\right) G\left(\vec{r}, \vec{r}'\right) d\vec{r}' = -\frac{j}{\omega\mu} \left[\hat{t}\left(\vec{r}\right) \cdot \vec{E}^i\left(\vec{r}\right)\right], \text{ for } \vec{r} \in S,$$

(4.1)
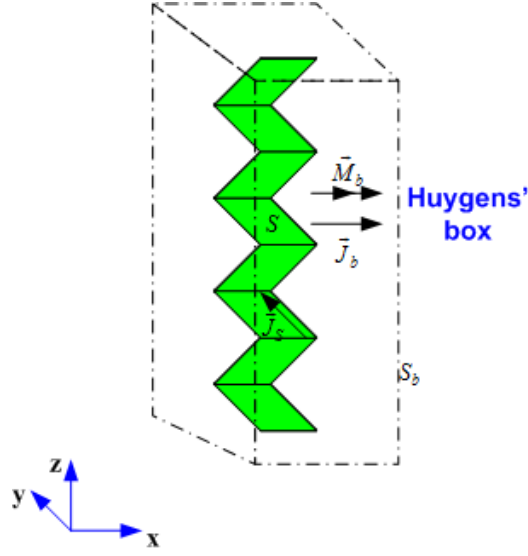
Figure 4.2: The MoM model: a metallic stirrer enclosed by a Huygens' box. The conducting stirrer is illuminated by the radiated fields of the equivalent current along Huygens' box.

where $\vec{E}^i$ is the electric field illuminating S, $\hat{t}(\vec{r})$ is the unit vector tangential to S at $\vec{r}$, k is the wavenumber, and G represents the free space Green's function [98]. It is known that the electric field illuminating the stirrer is radiated by the equivalent currents $\vec{J}_b$ and $\vec{M}_b$. $\vec{E}^i$ is then written as,

$$\vec{E}^i(\vec{r}) = -j\omega\mu \int\int_{S_b} \left(1 + \frac{1}{k^2}\nabla\nabla\cdot\right) \vec{J}_b(\vec{r}')\,G(\vec{r},\vec{r}')\,d\vec{r}'$$
$$-\nabla \times \int\int_{S_b} \vec{M}_b(\vec{r}')\,G(\vec{r},\vec{r}')\,d\vec{r}'. \tag{4.2}$$

Substituting (4.2) into (4.1), one can derive

$$\hat{t}(\vec{r}) \cdot \left[j\omega\mu \int\int_{S} \left(1 + \frac{1}{k^2}\nabla\nabla\cdot\right) \vec{J}_S(\vec{r}')\,G(\vec{r},\vec{r}')\,d\vec{r}'\right] =$$
$$-\hat{t}(\vec{r}) \cdot \left[j\omega\mu \int\int_{S_b} \left(1 + \frac{1}{k^2}\nabla\nabla\cdot\right) \vec{J}_b(\vec{r}')\,G(\vec{r},\vec{r}')\,d\vec{r}'\right]$$
$$-\hat{t}(\vec{r}) \cdot \left[\nabla \times \int\int_{S_b} \vec{M}_b(\vec{r}')\,G(\vec{r},\vec{r}')\,d\vec{r}'\right], \text{ for } \vec{r} \in S. \tag{4.3}$$
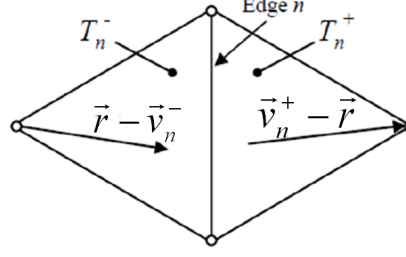
Figure 4.3: RWG basis function.

The stirrer surface S and the Huygens' box surface S_b can be discretized using a set of planar triangles. $\vec{J}_S$, $\vec{J}_b$, and $\vec{M}_b$ are then expanded with the famous RWG basis [50]. The RWG basis function is defined in a pair of triangles shown in Figure 4.3. The two triangles T_n^+ and T_n^- share edge n. The RWG basis function $\vec{f}_n(\vec{r})$ is defined as [50]

$$
\vec{f}_n(\vec{r}) = \left[
\begin{array}{ll}
\frac{l_n}{2A_n^+}\left(\vec{v}_n^+ - \vec{r}\right) & \vec{r} \text{ in } T_n^+ \\[2mm]
\frac{l_n}{2A_n^-}\left(\vec{r} - \vec{v}_n^-\right) & \vec{r} \text{ in } T_n^- \\[2mm]
0 & \text{otherwise}
\end{array}
\right], \tag{4.4}
$$

where v_n^+ and v_n^- are vertices of T_n^+ and T_n^- opposite edge n, respectively. l_n is the length of edge n, and A_n^+ and A_n^- are areas of T_n^+ and T_n^-, respectively. The surface divergence of $f_n(\vec{r})$ is

$$
\nabla \cdot \vec{f}_n(\vec{r}) = \left[
\begin{array}{ll}
-\frac{l_n}{A_n^+} & \vec{r} \text{ in } T_n^+ \\[2mm]
\frac{l_n}{A_n^-} & \vec{r} \text{ in } T_n^- \\[2mm]
0 & \text{otherwise}
\end{array}
\right]. \tag{4.5}
$$

In order to use RWG basis function, the surface of an object is first discretized into a set of triangles. The RWG basis function is then defined on two adjacent triangles sharing a edge. Since the divergence of the current is proportional to the surface charge density through the equation of continuity, (4.5) indicates that the total charge density associated with adjacent triangle pairs is zero. As there is no accumulation of charges

55

on an edge, the RWG function is said to be divergence conforming.

Invoking Galerkin method upon both sides of (4.3), one can obtain the following equation

$$\mathbf{Z^e j_b} + \mathbf{Z^c m_b} = \mathbf{Z j_S}, \tag{4.6}$$

where $\mathbf{j_b}$, $\mathbf{m_b}$, and $\mathbf{j_S}$ are vectors constituted by current expansion coefficients of $\vec{J}_b$, $\vec{M}_b$, and $\vec{J}_S$, respectively. Matrices $\mathbf{Z^e}$, $\mathbf{Z^c}$, and $\mathbf{Z}$ are defined as

$$
Z^e_{mn} = -j\omega\mu \int\int_{S_m} \vec{f}_m\left(\vec{r}\right) \cdot \int\int_{S^n_b} \vec{f}_n\left(\vec{r}'\right) G\left(\vec{r},\vec{r}'\right) d\vec{r}' d\vec{r}
$$
$$
-\frac{1}{j\omega\epsilon} \int\int_{S_m} \nabla \cdot \vec{f}_m\left(\vec{r}\right) \left[\int\int_{S^n_b} \nabla' \cdot \vec{f}_n\left(\vec{r}'\right) G\left(\vec{r},\vec{r}'\right) d\vec{r}'\right] d\vec{r}, \tag{4.7}
$$

$$
Z^c_{mn} = -\int\int_{S_m} \vec{f}_m\left(\vec{r}\right) \cdot \left[\nabla \times \int\int_{S^n_b} \vec{f}_n\left(\vec{r}'\right) G\left(\vec{r},\vec{r}'\right) d\vec{r}'\right] d\vec{r}, \tag{4.8}
$$

and

$$
Z_{mn} = j\omega\mu \int\int_{S_m} \vec{f}_m\left(\vec{r}\right) \cdot \left[\int\int_{S_n} \vec{f}_n\left(\vec{r}'\right) G\left(\vec{r},\vec{r}'\right) d\vec{r}'\right] d\vec{r}
$$
$$
+\frac{1}{j\omega\epsilon} \int\int_{S_m} \nabla \cdot \vec{f}_m\left(\vec{r}\right) \left[\int\int_{S_n} \nabla' \cdot \vec{f}_n\left(\vec{r}'\right) G\left(\vec{r},\vec{r}'\right) d\vec{r}'\right] d\vec{r}. \tag{4.9}
$$

In (4.7)-(4.9), S_m represents the domain of the mth RWG basis on the surface of the stirrer S, and S^n_b is the domain of the nth RWG basis on the surface of the Huygens' box S_b.

Matrix $\mathbf{Z}$ is the same as the interaction matrix in the conventional MoM solution of

the EFIE. Matrix $\mathbf{Z^e}$ only has a difference of negative sign from the interaction matrix in MoM solution of the EFIE. Except for a difference of negative sign, matrix $\mathbf{Z^c}$ is the same as the interaction matrix in the conventional MoM solution of the MFIE [98]. The calculation of matrix elements and the treatment of singularity are thus similar to those in the conventional MoM. In this work, the integral over a triangle is calculated with a Gaussian quadrature. Since the Huygens' box doesn't overlap with the stirrer, there is no singularity in matrices $\mathbf{Z^c}$ and $\mathbf{Z^e}$. The singularity encountered when filling the matrix $\mathbf{Z}$ is dealt with using the analytical and numerical integrations [98]. The numerical calculation of integrals in (4.7) to (4.9) and the treatment of singularity were well documented in [98]. For readers' convenience, Appendix C details the numerical calculation of integrals appearing in (4.7) to (4.9).

4.2.2   The DSC Model

The DSC model is shown in Figure 4.4, where the conducting stirrer has been replaced by a current sheet $\vec{J}_S$. The RC is then equivalent to a large cavity excited by current sources $\vec{J}_0$ and $\vec{J}_S$, which can be efficiently modeled using the DSC method. It should be explained that $\vec{J}_0$ is the original current source replacing the transmitting antenna. Maxwell's equations governing the fields in the DSC model are

$$\nabla \times \vec{E}_{DSC} = -j\omega\mu\vec{H}_{DSC}, \tag{4.10a}$$

$$\nabla \times \vec{H}_{DSC} = \vec{J}_S + \vec{J}_0 + j\omega\epsilon\vec{E}_{DSC}. \tag{4.10b}$$

Taking curl on both sides of (4.10a), and eliminating $\nabla \times \vec{H}_{DSC}$ using (4.10b), one can obtain

$$\nabla \times \nabla \times \vec{E}_{DSC} - \omega^2\mu\epsilon\vec{E}_{DSC} = -j\omega\mu\left(\vec{J}_S + \vec{J}_0\right). \tag{4.11}$$
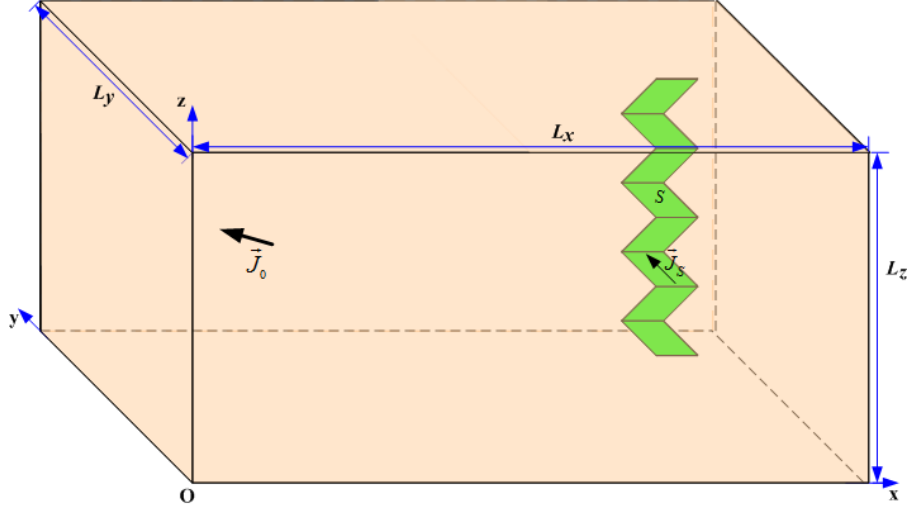
Figure 4.4: The DSC model: a large cavity excited by the original source $\vec{J_0}$ and the current sheet $\vec{J_s}$. For simplicity, the transmitting antenna has been replaced by a current source $\vec{J_0}$. This is reasonable when the main concern is the analysis of the RC itself.

In (4.11), there are totally six differential operators, and they are expanded as follows in the DSC method. First, using the interpolation basis, arbitrary field component f can be expanded as

$$f(x, y, z) = \sum_{i=-M+1}^{M} \sum_{j=-M+1}^{M} \sum_{k=-M+1}^{M} K_M^{i,j,k}(x, y, z) f(x_i, y_j, z_k), \qquad (4.12)$$

where

$$K_M^{i,j,k}(x, y, z) = L_{M,i}(x) L_{M,j}(y) L_{M,k}(z),$$

L represents regularized Lagrange interpolation bases, and $2M$ is the order of the interpolation bases. The definition of L can be found in equation (3.3), and it is omitted here for simplicity. (x_i, y_j, z_k) is a point neighboring to the point (x, y, z), and i, j, and k are local indexes of the point in x-, y-, and z-directions, respectively. Hence, at a point (x_0, y_0, z_0), these differential operators can be expressed as shown in (4.13) (on the top of next page), where L' and L'' represent ordinary like derivatives

58

$$\frac{\partial^2 f(x,y,z)}{\partial x^2} = \sum_{i=-M+1}^{M} L''_{M,i}(x) f(x_i, y_0, z_0), \qquad (4.13\text{a})$$

$$\frac{\partial^2 f(x,y,z)}{\partial y^2} = \sum_{j=-M+1}^{M} L''_{M,j}(y) f(x_0, y_j, z_0), \qquad (4.13\text{b})$$

$$\frac{\partial^2 f(x,y,z)}{\partial z^2} = \sum_{k=-M+1}^{M} L''_{M,k}(z) f(x_0, y_0, z_k), \qquad (4.13\text{c})$$

$$\frac{\partial^2 f(x,y,z)}{\partial x \partial y} = \sum_{i=-M+1}^{M} \sum_{j=-M+1}^{M} L'_{M,i}(x) L'_{M,j}(y) f(x_i, y_j, z_0), \qquad (4.13\text{d})$$

$$\frac{\partial^2 f(x,y,z)}{\partial x \partial z} = \sum_{i=-M+1}^{M} \sum_{k=-M+1}^{M} L'_{M,i}(x) L'_{M,k}(z) f(x_i, y_0, z_k), \qquad (4.13\text{e})$$

$$\frac{\partial^2 f(x,y,z)}{\partial y \partial z} = \sum_{j=-M+1}^{M} \sum_{k=-M+1}^{M} L'_{M,j}(y) L'_{M,k}(z) f(x_0, y_j, z_k), \qquad (4.13\text{f})$$

of the first and second orders, respectively. Differentials of interpolation bases can be numerically computed with a recursive procedure [97].

For numerical implementation of the DSC method, Yee's grid [48] can be used to discretize the computational domain. Since the current sources $\vec{J}_0$ and $\vec{J}_S$ may not be conformal with the structured grids, the regularization technique [96] can be adopted to express the current sources on the structured grids. The validity of the regularization technique has been rigorously proved by Tornberg [96] with more details. The regularization technique was applied in Chapter 3 for the development of a 2-D hybrid method.

Discretizing the computational domain with Yee's grids, expressing the current sources on the Yee's grid with the regularization technique, and approximating the differential operators with (4.13), the partial differential equation (4.11) can be trans-

formed to a set of linear equations for the unknown scalar field quantities

$$(\mathbf{D} + C_1\mathbf{I})\,\mathbf{e_{DSC}} = C_2\,(\mathbf{R_S}\mathbf{j_S} + \mathbf{R_0}\mathbf{j_0})\,, \tag{4.14}$$

where $C_1 = -\omega^2\mu\epsilon$, and $C_2 = -j\omega\mu$. $\mathbf{e_{DSC}}$ is the unknown spatial expansion coefficients for the electric field. $\mathbf{D}$ is the differentiation matrix [97], and $\mathbf{I}$ is the identity matrix. Definition of matrix $\mathbf{D}$ is elucidated in Appendix A.2. $\mathbf{j_0}$ is the vector constituted by discrete sampling of $\vec{J}_0$. $\mathbf{R_S}$ and $\mathbf{R_0}$ are regularization matrices for $\vec{J}_S$ and $\vec{J}_0$, respectively. Numerical computations of $\mathbf{R_S}$ and $\mathbf{R_0}$ are detailed in the next two paragraphs.

For an arbitrary current $\vec{J}_S$ distributed on a three-dimensional surface S, using the regularization technique, the regularized current $\vec{J}_S^R$ at the mth DSC grid point $\vec{r}_m$ can be computed as

$$\vec{J}_S^R(\vec{r}_m) = \int\int_S \zeta_\epsilon(\vec{r}_m - \vec{r}')\vec{J}_S(\vec{r}')d\vec{r}', \tag{4.15}$$

where

$$\zeta_\epsilon(\vec{r}_m - \vec{r}') = \zeta_\epsilon(x_m - x')\zeta_\epsilon(y_m - y')\zeta_\epsilon(z_m - z'),$$

ζ_ϵ represents the regularized Dirac function defined in [96]. (x', y', z') and (x_m, y_m, z_m) are coordinates of $\vec{r}'$ and $\vec{r}_m$, respectively. Substituting the expansion of $\vec{J}_S$ into (4.15), one can derive

$$\vec{J}_S^R(\vec{r}_m) = \sum_{n=1}^{N_S} j_S^n \int\int_{S_n} \zeta_\epsilon(\vec{r}_m - \vec{r}')\vec{f}_n(\vec{r}')d\vec{r}'. \tag{4.16}$$

Depending on the direction of the field component designated at $\vec{r}_m$, different components should be extracted in (4.16). From (4.16), one can obtain the definition of $\mathbf{R_S}$

as

$$R_S\left(m,n\right) = \int\int_{S_n} \zeta_\epsilon(\vec{r}_m - \vec{r}')\hat{a} \cdot \vec{f}_n(\vec{r}')d\vec{r}', \tag{4.17}$$

where the unit vector $\hat{a}$ represents the direction of the electric field component designated to the mth DSC grid point.

$\vec{J}_0$ may be a surface or line current source. When $\vec{J}_0$ is a surface current source, it can be expanded using the RWG basis, and then its regularization matrix will be the same as (4.17). If $\vec{J}_0$ is a line current source, its regularized form $\vec{J}_0^R$ at $\vec{r}_m$ is

$$\vec{J}_0^R(\vec{r}_m) = \int_C \zeta_\epsilon(\vec{r}_m - \vec{r}')\vec{J}_0(\vec{r}')d\vec{r}', \tag{4.18}$$

where C represents the domain of $\vec{J}_0$. C can be of arbitrary shape. Expanding $\vec{J}_0$ with pulse function basis and replacing the integration with a trapezoidal rule, (4.18) becomes

$$\vec{J}_0^R(\vec{r}_m) = \sum_{n=1}^{N_C} \zeta_\epsilon(\vec{r}_m - \vec{r}_n)\vec{J}_0(\vec{r}_n)C_n, \tag{4.19}$$

where N_C is the total number of discrete segments for C, and C_n is the length of the nth segment. $\vec{r}_n$ is the center of C_n. Therefore, matrix $\mathbf{R_0}$ has the form of

$$R_0\left(m,n\right) = \zeta_\epsilon(\vec{r}_m - \vec{r}_n)\hat{a} \cdot \vec{J}_0\left(\vec{r}_n\right) \frac{1}{|\hat{a} \cdot \vec{J}_0\left(\vec{r}_n\right)|}C_n. \tag{4.20}$$

If $\vec{J}_0$ is a point current source, the integral in (4.18) will reduce to a product.

In order to enforce the boundary condition of the conducting rectangular cavity, symmetric extension is used for normal electric or tangential magnetic field compo-

61

nents near cavity walls. For tangential electric or normal magnetic field components near cavity walls, anti-symmetric extension is used to force them to be zero along the conducting walls.

4.2.3 Hybridization

On the surface S_b of Huygens' box, the equivalent currents $\vec{J}_b$ and $\vec{M}_b$ are related to the field solution in the DSC model by the equivalence principle

$$\vec{J}_b(\vec{r}) = \hat{n} \times \vec{H}_{DSC}^b(\vec{r}), \ \vec{r} \in S_b,$$

$$\vec{M}_b(\vec{r}) = -\hat{n} \times \vec{E}_{DSC}^b(\vec{r}), \ \vec{r} \in S_b, \tag{4.21}$$

where $\hat{n}$ is the inward unit vector normal to the Huygens' box. $\vec{H}_{DSC}^b$ and $\vec{E}_{DSC}^b$ denote the magnetic and electric fields on Huygens' box, respectively. In the MoM model, $\vec{M}_b$ and $\vec{J}_b$ are expanded using the RWG basis. In order to relate the current expansion coefficients with $\vec{H}_{DSC}^b$ and $\vec{E}_{DSC}^b$, one may invoke a Galerkin's matching process upon (4.21). However, that will introduce extra computation. On the other hand, an interesting property of RWG basis is that the expansion coefficient for the nth basis happens to be the value of the current component normal to the nth shared edge. Utilizing the aforementioned property of the RWG basis, one can easily obtain

$$j_b^n = \hat{n}^{ne} \cdot \left(\hat{n} \times \vec{H}_{DSC}^b(\vec{r}_n) \right), \tag{4.22a}$$

$$m_b^n = -\hat{n}^{ne} \cdot \left(\hat{n} \times \vec{E}_{DSC}^b(\vec{r}_n) \right), \tag{4.22b}$$

where j_b^n and m_b^n are the nth current expansion coefficients for $\vec{J}_b$ and $\vec{M}_b$. $\hat{n}^{ne}$ is the unit vector normal to the nth shared edge, which lies in T_n^+ and points towards the free vertex of T_n^+, as shown in Figure 4.5. $\vec{r}_n$ can be an arbitrary point on the nth shared edge. In this work, $\vec{r}_n$ is chosen to be the middle point of the nth edge. The
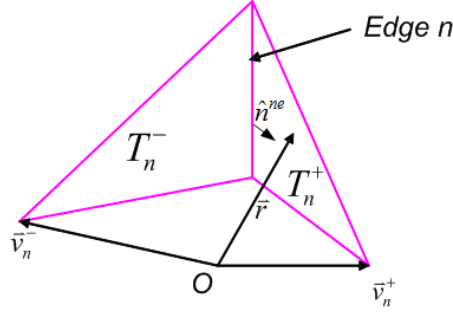
Figure 4.5: Illustration of the vector $\hat{n}^{ne}$.

matrix form of (4.22) is

$$\mathbf{j_b} = \mathbf{T_{hj}} \mathbf{h^b_{DSC}}, \tag{4.23a}$$

$$\mathbf{m_b} = \mathbf{T_{em}} \mathbf{e^b_{DSC}}, \tag{4.23b}$$

where $\mathbf{h^b_{DSC}}$ and $\mathbf{e^b_{DSC}}$ are, respectively, vectors constituted by values of magnetic and electric fields at the centers of shared edges. Furthermore,

$$\mathbf{j_b} = \begin{bmatrix} j_{b,1} & j_{b,2} & ... & j_{b,N_b} \end{bmatrix}^T, \tag{4.24}$$

and

$$\mathbf{h^b_{DSC}} = \begin{bmatrix} h^{bx}_{DSC,1}, & ..., & h^{bx}_{DSC,N_b}, & h^{by}_{DSC,1}, & ..., & h^{by}_{DSC,N_b}, & h^{bz}_{DSC,1}, & ..., & h^{bz}_{DSC,N_b} \end{bmatrix}^T, \tag{4.25}$$

where $j_{b,k}$ is the kth expansion coefficient of $\vec{J}_b$, and $h^{b\xi}_{DSC,k}$ denotes the value of ξ-component of magnetic field at the center of the kth shared edge. N_b is the total number of shared edges on Huygens' box, and ξ can be x, y, or z. The form of $\mathbf{m_b}$ is the same as $\mathbf{j_b}$. Replacing 'j' by 'm', one can obtain the expression of $\mathbf{m_b}$ from (4.24). Furthermore, the expression of $\mathbf{e^b_{DSC}}$ can be obtained from (4.25) by

63

replacing 'h' with 'e'. Matrices $\mathbf{T_{hj}}$ and $\mathbf{T_{em}}$ represent the translation between fields and currents, and they are obtained from equation (4.22) as follows. Using the vector identity $\vec{a} \cdot (\vec{b} \times \vec{c}) = (\vec{a} \times \vec{b}) \cdot \vec{c}$, (4.22) is rewritten as

$$j_b^n = \hat{u}^n \cdot \ \vec{H}_{DSC}^b(\vec{r}_n),$$

$$m_b^n = -\hat{u}^n \cdot \ \vec{E}_{DSC}^b(\vec{r}_n), \tag{4.26}$$

where $\hat{u}^n = \hat{n}^{ne} \times \hat{n}$. Since both the magnetic and electric fields have three components, one can observe from (4.26) that matrices $\mathbf{T_{hj}}$ and $\mathbf{T_{em}}$ are of size $N_b \times 3N_b$, and they are defined as

$$T_{hj}(m,n) = \left[\begin{array}{ll} u_x^m, & \text{for } m = n, \\ u_y^m, & \text{for } m = n - N_b, \\ u_z^m, & \text{for } m = n - 2N_b, \\ 0 & \text{otherwise.} \end{array} \right],$$

and $\mathbf{T_{em}} = -\mathbf{T_{hj}}$. u_x^m, u_y^m, and u_z^m are the x, y, and z components of the vector $\hat{u}^m$, respectively.

Since $\vec{r}_n$ may not happen to be a grid point in the DSC model, interpolation may be required to obtain the electric and magnetic fields at $\vec{r}_n$. By the field expansion (4.12), ξ-component of $\vec{H}_{DSC}^b(\vec{r}_n)$ and $\vec{E}_{DSC}^b(\vec{r}_n)$ can be calculated as

$$H_{DSC}^{b\xi}(\vec{r}_n) = \sum_{\substack{i=-M \\ i\neq 0}}^{M} \sum_{\substack{j=-M \\ j\neq 0}}^{M} \sum_{\substack{k=-M \\ k\neq 0}}^{M} w_{i,j,k}^{h\xi} H_{DSC}^{(i,j,k)\xi}, \tag{4.27a}$$

$$E_{DSC}^{b\xi}(\vec{r}_n) = \sum_{\substack{i=-M \\ i\neq 0}}^{M} \sum_{\substack{j=-M \\ j\neq 0}}^{M} \sum_{\substack{k=-M \\ k\neq 0}}^{M} w_{i,j,k}^{e\xi} E_{DSC}^{(i,j,k)\xi}, \tag{4.27b}$$

where the superscript ξ represents the direction of the field component, and it can be x, y, or z. $E_{DSC}^{(i,j,k)\xi}$ and $H_{DSC}^{(i,j,k)\xi}$ are values of ξ-component of electric and magnetic
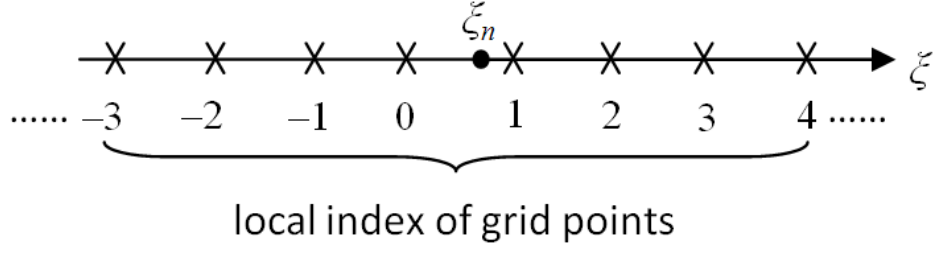
Figure 4.6: Definition of local indexes (ξ can be x, y, or z, and ξ_n is the ξ-component of $\vec{r}_n$).

fields at the (i, j, k)th grid point around $\vec{r}_n$. i, j, and k are local indexes in x, y, and z-directions for DSC grid points surrounding $\vec{r}_n$. Figure 4.6 illustrates how the local index of the grid points is defined. $w_{i,j,k}^{e\xi}$ and $w_{i,j,k}^{h\xi}$ represent interpolating weights for ξ-component of electric and magnetic fields, respectively.

It should be noted that all field components have mutually different grid points in Yee's grids. Therefore, with the same index (i,j,k), the values of interpolating weight are different for every field component. Equation (4.27) can be written in the matrix form as

$$\mathbf{h_{DSC}^b} = \mathbf{W^h}\mathbf{h_{DSC}}, \qquad (4.28a)$$

$$\mathbf{e_{DSC}^b} = \mathbf{W^e}\mathbf{e_{DSC}}, \qquad (4.28b)$$

where vector $\mathbf{h_{DSC}}$ is constituted by the expansion coefficients of magnetic field at DSC grid points. Construction of interpolation matrices $\mathbf{W^h}$ and $\mathbf{W^e}$ is described in detail in Appendices B.2 and B.3, respectively. Using (4.28), (4.23) can be rewritten as

$$\mathbf{j_b} = \mathbf{T_{hj}}\mathbf{W^h}\mathbf{h_{DSC}}, \qquad (4.29a)$$

$$\mathbf{m_b} = \mathbf{T_{em}}\mathbf{W^e}\mathbf{e_{DSC}}. \qquad (4.29b)$$

65

Using (4.29), $\mathbf{j_b}$ and $\mathbf{m_b}$ in (4.6) can be eliminated, resulting in

$$\mathbf{Z^e T_{hj} W^h h_{DSC}} + \mathbf{Z^c T_{em} W^e e_{DSC}} = \mathbf{Z j_S}. \tag{4.30}$$

$\mathbf{h_{DSC}}$ in (4.30) can be eliminated with $\mathbf{e_{DSC}}$ utilizing (4.10a). By discretizing the curl operator in (4.10a) with the DSC method, the following relationship is obtained

$$\mathbf{h_{DSC}} = \frac{1}{C_2} \mathbf{D^e e_{DSC}}, \tag{4.31}$$

where $\mathbf{D^e}$ is a differentiation matrix arising from the curl operator of (4.10a), and its evaluation is detailed in Appendix A.3. Using (4.31), (4.30) can be further simplified as

$$\mathbf{P_S e_{DSC}} = \mathbf{Z j_S}, \tag{4.32}$$

where

$$\mathbf{P_S} = \frac{1}{C_2} \mathbf{Z^e T_{hj} W^h D^e} + \mathbf{Z^c T_{em} W^e}.$$

Combining (4.32) with (4.14) and rearranging the equations, one can easily obtain

$$\begin{bmatrix} \mathbf{D} + C_1 \mathbf{I} & -C_2 \mathbf{R_S} \\ \mathbf{P_S} & -\mathbf{Z} \end{bmatrix} \begin{bmatrix} \mathbf{e_{DSC}} \\ \mathbf{j_S} \end{bmatrix} = \begin{bmatrix} C_2 \mathbf{R_0 j_0} \\ \mathbf{0} \end{bmatrix}. \tag{4.33}$$

By solving (4.33), the electric field $\mathbf{e_{DSC}}$ and the induced current $\mathbf{j_S}$ can be obtained. In (4.33), the differentiation matrix $\mathbf{D}$ is sparse, and therefore most part of the left-hand-side matrix in (4.33) is sparse. At the same time, it is known that iterative solvers have the problem of slow convergence in solving matrix equation arising from RC modeling due to its resonant nature. Hence, in this work, the direct sparse matrix

66

solver from UMFPACK [100] is employed for the solution of (4.33).

The derivation so far is based on the assumption that the RC is lossless. In practice, an RC has losses due to the cavity wall, the aperture leakage, a receiving antenna, and the loss in the equipment under test [42]. In order to take the small loss into account, the homogeneous loss model by Kildal [28] is adopted in this work. In the loss model by Kildal, the permittivity is assumed to be complex, and its value is calculated from the quality factor Q of an RC by

$$\epsilon' = \epsilon_0 \left(1 - \frac{j}{Q} \right), \tag{4.34}$$

where ϵ_0 and ϵ' represent the permittivity of free space and the lossy material, respectively. In order to consider the loss, one only needs to replace ϵ_0 with ϵ' in the previous formulation. It is known that the loss from a receiving antenna dominates the value of quality factor Q at low frequencies [42]. Therefore, Q can be calculated as [42]

$$Q = \frac{16\pi^2 V}{\lambda^3}, \tag{4.35}$$

where V is the volume of the cavity, and λ is the wavelength at the frequency of interest.

4.3   Numerical Examples

Numerical examples are presented in this section to demonstrate the validity and advantages of our proposed method. A C++ code is written to implement our hybrid method. The performance of the hybrid method is compared with the commercial software FEKO. Unless otherwise stated, simulations are conducted on a personal computer with a 2.67 GHz CPU and a 3.25 GB RAM. In FEKO and our MoM model,

the maximum length of the triangle edge is chosen to be one-tenth of λ. For multi-frequency analysis, frequency sweeping with a uniform frequency step size is adopted, and λ is chosen to be the wavelength at the highest frequency of interest. All integrals are calculated with a four-point Gaussian quadrature. Because iterative solvers have the problem of slow convergence [23], the direct solver is used in FEKO. In simulations that follow, the source current $\vec{J}_0$ is chosen to be a point source.

4.3.1 Performance Comparison

Using an RC with a single-plate stirrer, the hybrid code is first validated against FEKO, and its advantages over FEKO are demonstrated.

The geometry of the RC is shown in the inset of Figure 4.7. The single-plate stirrer is 4.25 m away from the bottom of the cavity, and it is parallel to the bottom surface of the cavity. The longer side of the plate is along the y-direction. The current source $\vec{J}_0$ is located at the point (2 m, 2 m, 1.6 m), and all the three orthogonal components of $\vec{J}_0$ are set to be 1 A/m². The dimension of the large cavity is 8.5 m×12.5 m×6 m. Starting from 41 MHz, the mode density of the cavity is above 1 mode per MHz. Therefore, the RC can theoretically operate from 41 MHz. According to [30], the most interesting frequency band for this RC would be 41 MHz to 82 MHz, where its performance needs analysis and optimization.

At the frequency of 82 MHz, $|E_x|$ is calculated along the line shown in the inset of Figure 4.7. According to (4.34) and (4.35), the permittivity is set to be $\epsilon' = \epsilon_0 \left(1 - j4.8643 \times 10^{-4}\right)$. h- and p-refinements are first conducted. Figure 4.7 presents the L_2 error of $|E_x|$ using different spatial sampling densities. The reference results are obtained using the grid size of $\lambda/d_{max} = 9.7561$, where $d_{max} = \max\{d_x, d_y, d_z\}$. d_x, d_y,
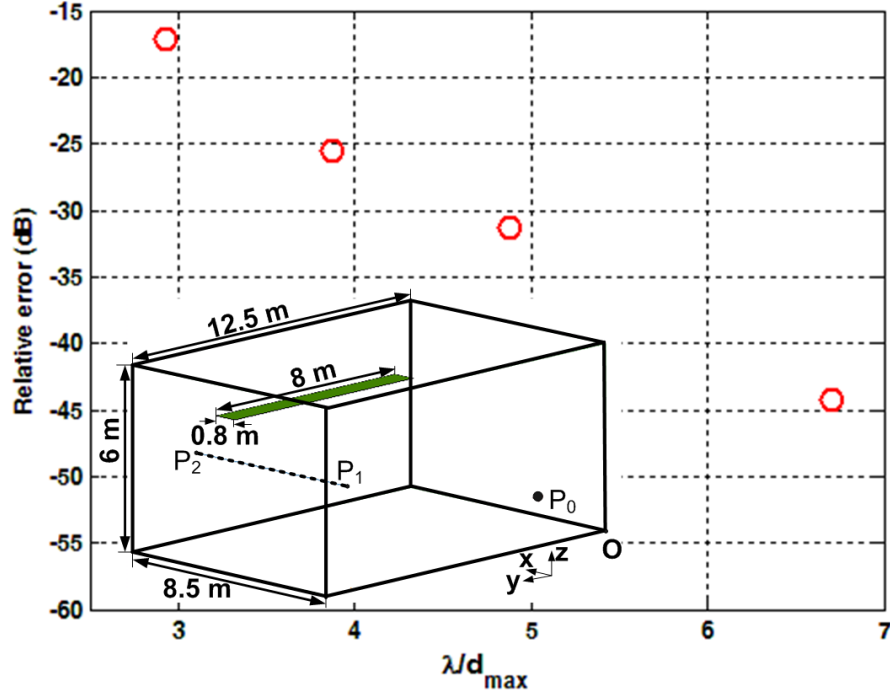
Figure 4.7: L_2 error of $|E_x|$ along a line inside the RC shown in the inset. The cavity is of dimension 8.5 m×12.5 m×6 m. The stirrer is a rectangular plate of dimension 8 m× 0.8 m, and its center is located at the point (6.6 m, 6.25 m, 4.25 m). A point current source is located at P_0 (2 m, 2 m, 1.6 m). All three orthogonal components of the current source is set to be 1 A/m^2. Field strength is observed along the straight line connecting points P_1 (1 m, 10.5 m, 3 m) and P_2 (7.5 m, 10.5 m, 3 m). d_{max} denotes the maximum grid size in x-, y-, and z-directions.

and d_z represent the grid size in x-, y-, and z-directions, respectively. RC modeling usually requires statistical analysis, where a lot of simulations are needed and computational efficiency becomes very important. Since the computational load increases rapidly with a decreasing grid size, the grid size is chosen to be around five points per wavelength to retain the good computational efficiency while achieving acceptable accuracy. The order of basis function is twelve in conducting the h-refinement. Figure 4.8 illustrates the error versus the order of basis function. The computational efficiency doesn't degrade a lot as the order of basis function increases and one may choose the order according to the desired accuracy. In this work, the order of ba-
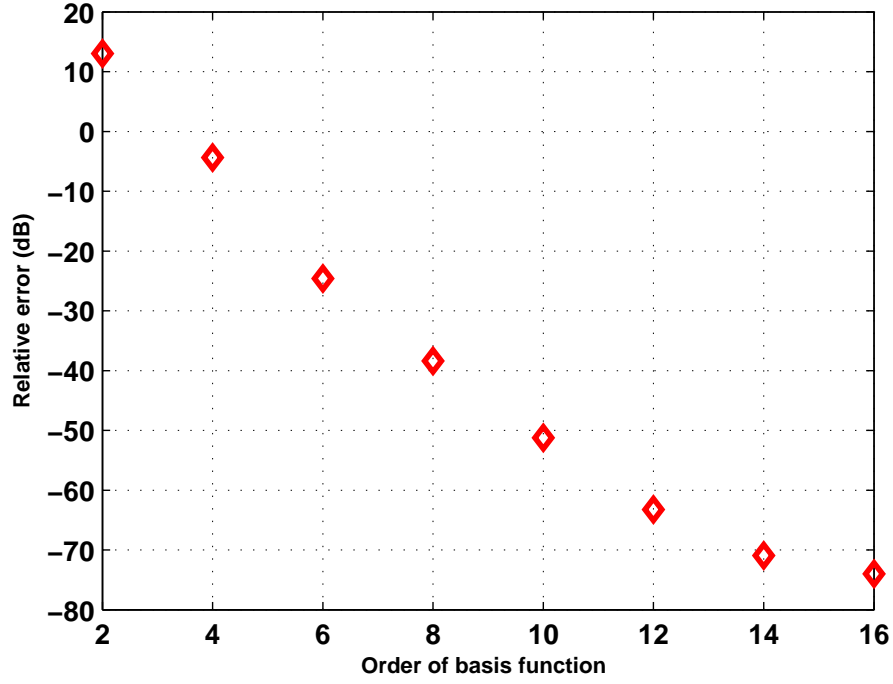
Figure 4.8: L_2 error of $|E_x|$ versus the order of basis function. $|E_x|$ is calculated along the line shown in the inset of Figure 4.7. The reference results are obtained using the 32nd order basis function.

sis function is chosen to be twelve. Therefore, all simulation results that follow are obtained with DSC order of twelve and grid size around $\lambda/5$.

Figures 4.9 to 4.11 present the field distribution along the straight line indicated in the inset of Figure 4.7 at the frequency of 82 MHz. Results from our proposed hybrid method agree well with those from FEKO. Figure 4.12 presents the observed electric field strength at the center of the RC from 40 MHz to 82 MHz. The frequency step is 0.1 MHz. Good agreement is again obtained between our proposed hybrid method and FEKO.

Another observation from Figure 4.12 is that the proposed method doesn't produce spurious modes. When spurious modes are present, there will be spurious resonant
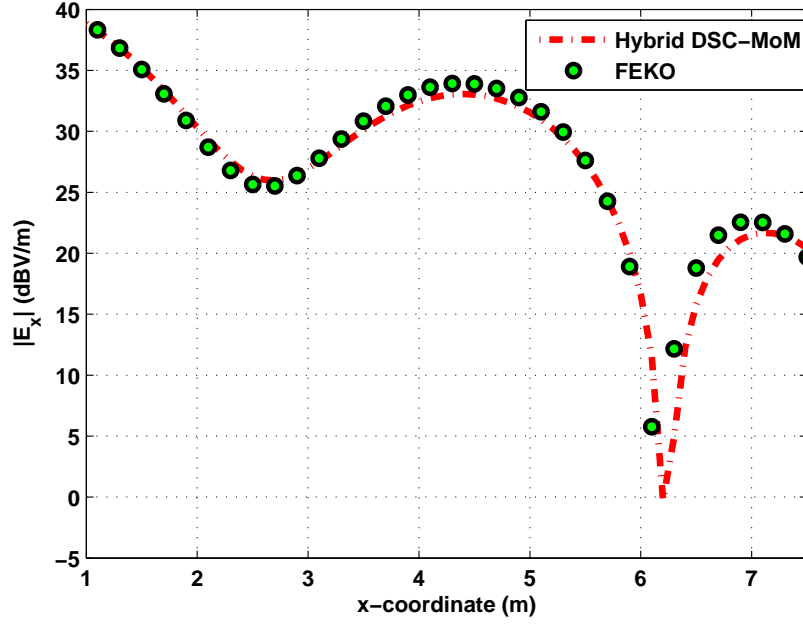
Figure 4.9: $|E_x|$ along the straight line between points P_1 and P_2 in the RC shown in the inset of Figure 4.7.
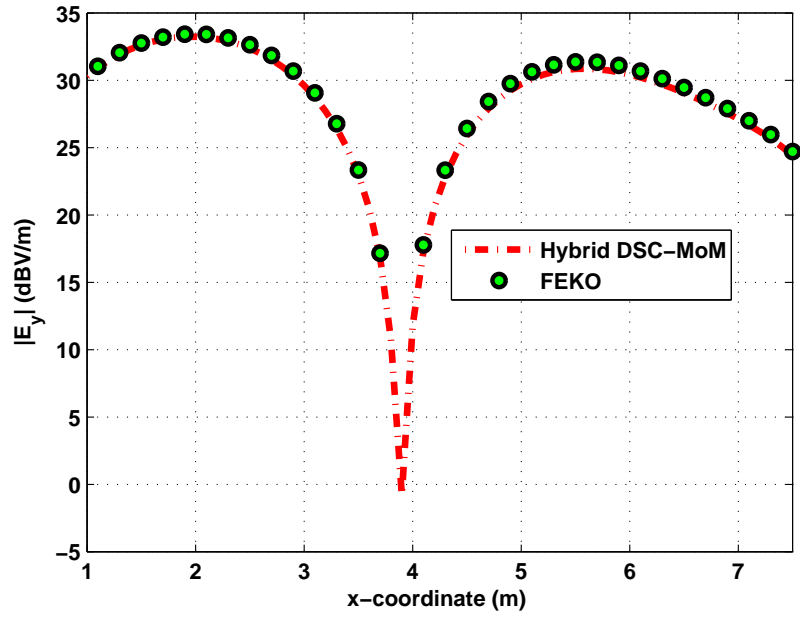
Figure 4.10: $|E_y|$ along the straight line between points P_1 and P_2 in the RC shown in the inset of Figure 4.7.
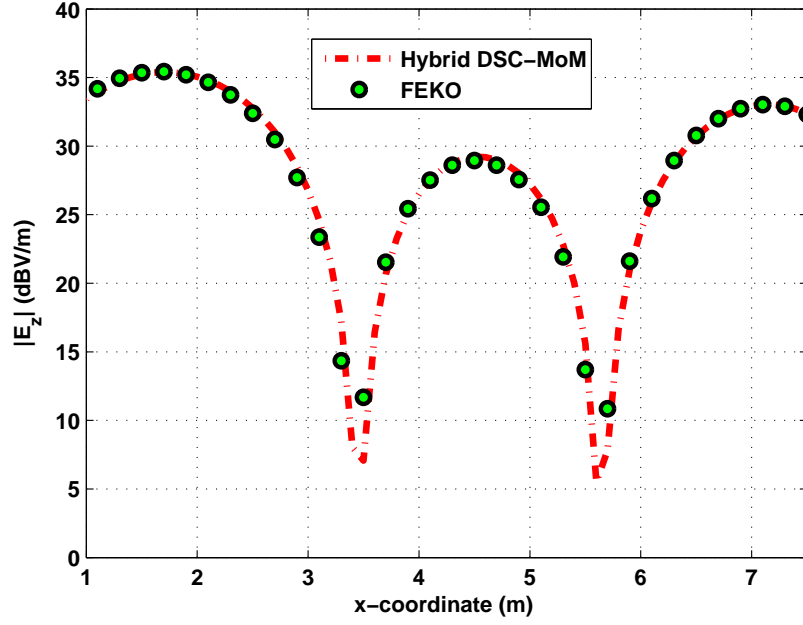
Figure 4.11: $|E_z|$ along the straight line between points P_1 and P_2 in the RC shown in the inset of Figure 4.7.
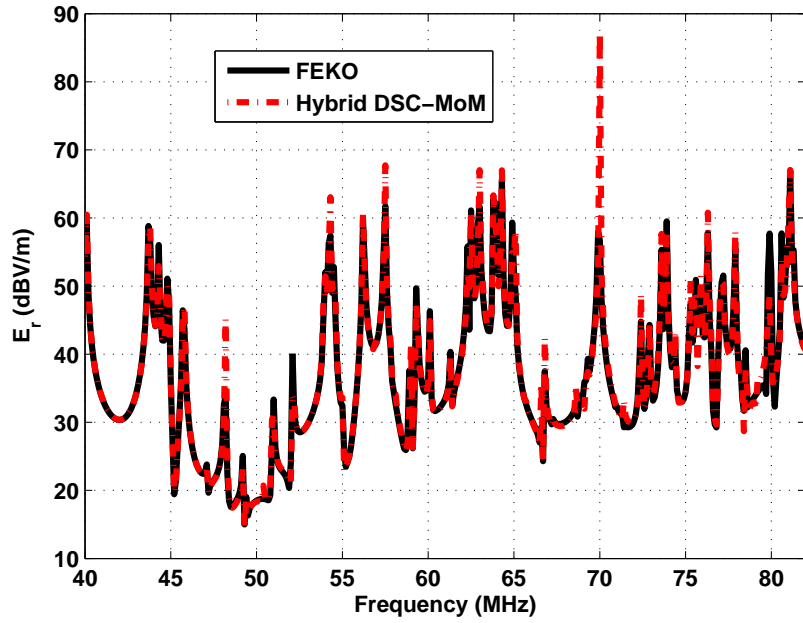
Figure 4.12: E_r ($E_r = \sqrt{|E_x|^2 + |E_y|^2 + |E_z|^2}$) at the center of the RC (illustrated in the inset of Figure 4.7) from 40 MHz to 82 MHz.

Table 4.1: Time and Memory Cost Comparisons Between Our Hybrid Method and FEKO for One Stirrer Position and One Frequency Point

Method	Grid size (m)*	Number of unknowns	CPU time (seconds)	Peak memory (GB)
Hybrid DSC-MoM	d_x=0.7727 d_y=0.7353 d_z=0.75 l_{max}=0.3659	3915	183	0.66
FEKO	l_{max}=0.3659	16424	2130.97	2.019

* l_{max} denotes the maximum length of triangle edge in the MoM.

frequencies and the frequency response will become messy [101]. Figure 4.12 shows that the proposed method doesn't generate any spurious resonant frequencies. The DSC method has also been applied to calculate the resonant frequencies of a microstrip line with a rectangular shield [74], where no spurious solution was observed. Spurious solutions in higher-order finite difference methods have been studied in [102]. It has been found that exact differentiation doesn't produce any spurious modes. However, using higher-order basis may introduce spurious modes when asymmetric approximation (e.g. one-sided finite difference) is used to deal with complicated boundaries. In modeling the rectangular conducting cavity, there is no need to use asymmetric approximation. Therefore, the proposed method doesn't produce spurious solution for RC modeling.

Table 4.1 summarizes CPU time and memory cost comparisons between our proposed method and FEKO. The proposed hybrid method is about ten times faster than FEKO. In FEKO, filling the interaction matrix requires calculation of integrals over the cavity. Furthermore, the LU decomposition of a full matrix is time consuming. In the proposed hybrid technique, integral over the surface of a large cavity is avoided. In modeling the cavity, the differentiation matrix **D** in this example has a sparsity of 95.55%, and its filling is fast. Meanwhile, LU decomposition of a sparse matrix is
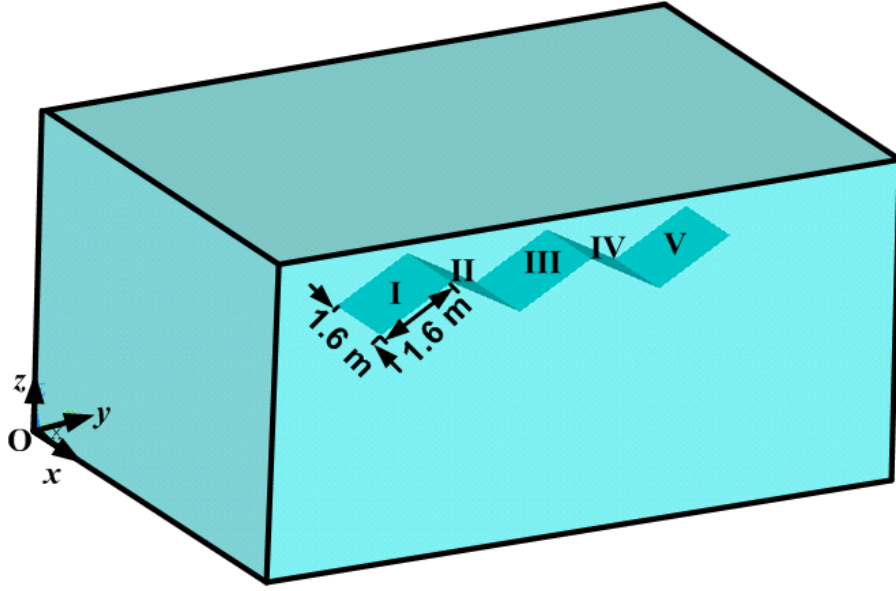
Figure 4.13: Geometry of an RC with a five-paddle stirrer. Dimension of the five paddles is the same. Angle between two adjacent paddles is 122.09^o. The center of paddle III is located at (6.6 m, 6.25 m, 4.25 m). The dimension of the cavity is the same as the one shown in the inset of Figure 4.7.

efficient as well. More importantly, with coarse grids in the DSC method, the number of unknowns is reduced to one-fourth of that in FEKO. The memory usage of the proposed method is only one third of that by FEKO. It should be noted that the memory cost in the proposed hybrid method is mainly caused by the LU solver. This is different from the case in FEKO, where both interaction matrix and LU solver consume a lot of memory.

4.3.2 Study of Stirring Effect

After having validated the proposed hybrid method and demonstrated its high efficiency, the proposed method is used to study the stirring effect of three stirrers. The first stirrer is the one shown in the inset of Figure 4.7, which is a single-plate stirrer of dimension 0.8 m×8 m. The second one is a larger single-plate stirrer of dimension 1.6 m×8 m. The third one is a five-paddle stirrer consisting of five equal-sized square

74
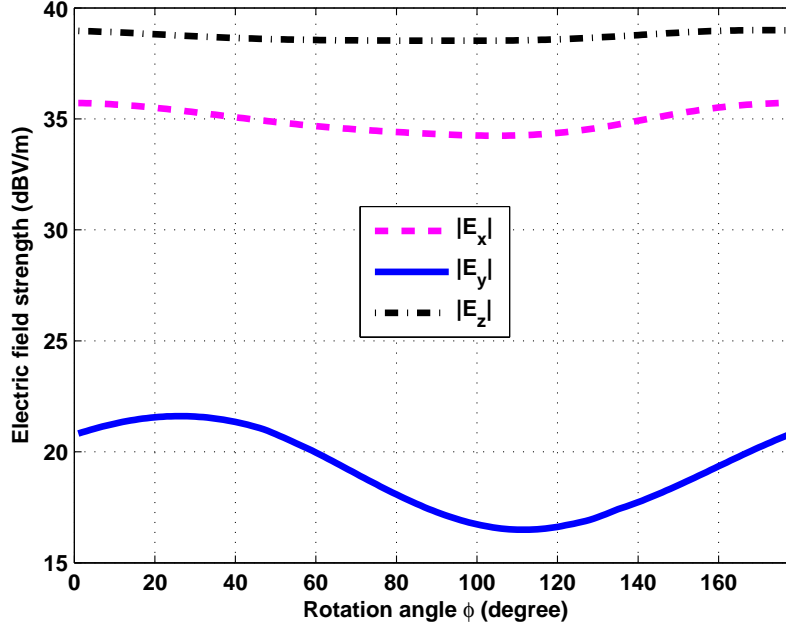
Figure 4.14: Electric field strength at the point (4.25 m, 6.36 m, 3 m) during one stirrer rotation cycle with a single-plate stirrer of dimension 0.8 m×8 m. The excitation frequency is 82 MHz.

plates of side length 1.6 m. Geometry of the third stirrer is shown in Figure 4.13. For the single-plate stirrers, the center of the stirrer is located at the point (6.6 m, 6.25 m, 4.25 m). For the five-paddle stirrer, the center of paddle III is located at the point (6.6 m, 6.25 m, 4.25 m). All three stirrers are assumed to be rotated clockwise (looking toward the positive y-direction) around a y-directed straight line passing through the point (6.6 m, 6.25 m, 4.25 m). The angle by which a stirrer has been rotated is named as the rotation angle ϕ.

Figures 4.14-4.16 illustrate the strength of the three orthogonal electric field components at the point (4.25 m, 6.36 m, 3 m) during one stirrer rotation cycle. In all three cases, a point source is adopted as the excitation. The definition of the point source is the same as in Section 4.3.1. The step size of rotation angle is 1 degree. For single-plate stirrers, 180 stirrer positions are considered, because a single-plate
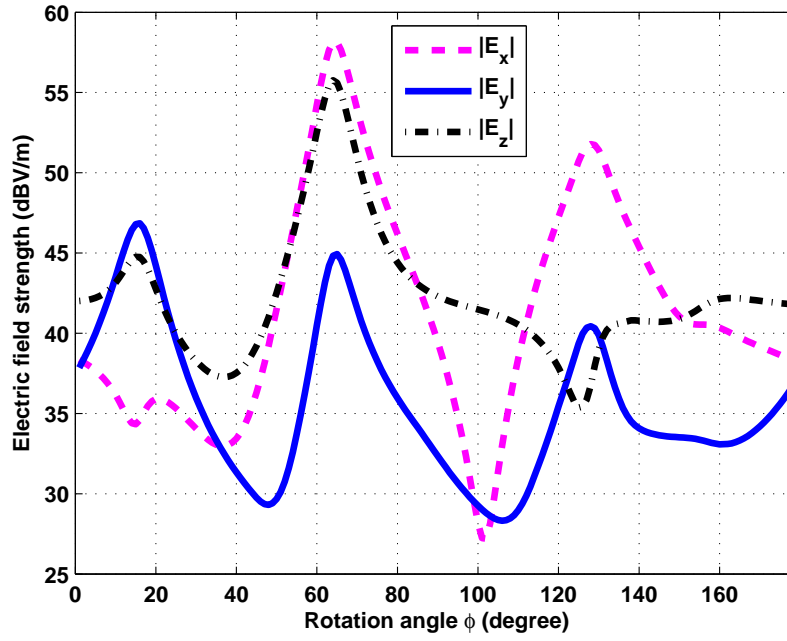
Figure 4.15: Electric field strength at the point (4.25 m, 6.36 m, 3 m) during one stirrer rotation cycle with a single-plate stirrer of dimension 1.6 m×8 m. The excitation frequency is 82 MHz.
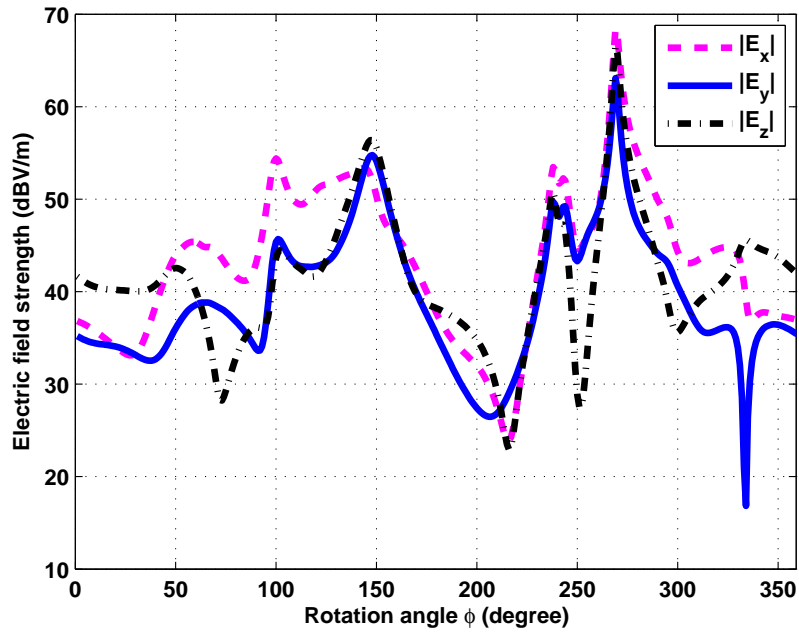
Figure 4.16: Electric field strength at the point (4.25 m, 6.36 m, 3 m) during one stirrer rotation cycle with the five-paddle stirrer illustrated in Figure 4.13. The excitation frequency is 82 MHz.
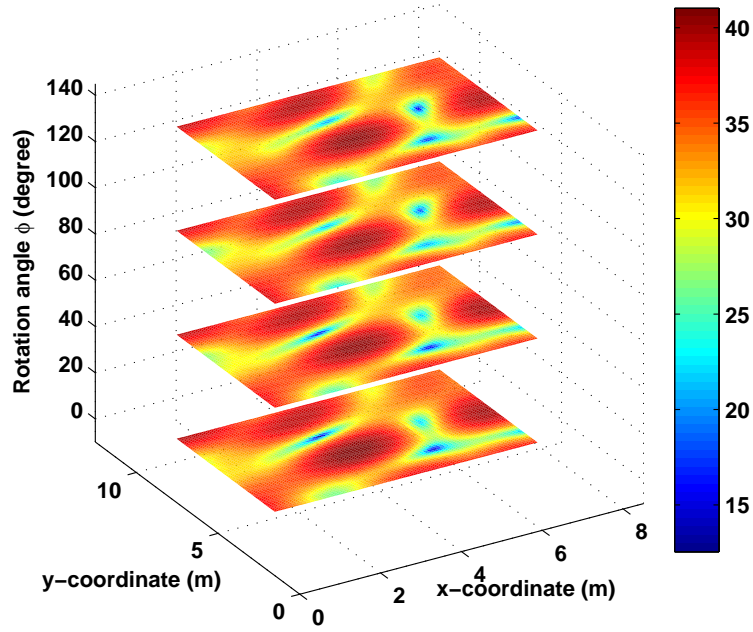
Figure 4.17: Distribution of E_r along a plane in the RC at four stirrer positions with excitation frequency of 82 MHz. The stirrer is the single-plate stirrer of dimension 0.8 m$\times$ 8 m.

stirrer goes back to its original position after being rotated by 180 degrees. For the five-paddle stirrer, 360 stirrer positions are considered. From Figures 4.14-4.16, one can easily observe different stirring effects of the three stirrers. A single-plate stirrer of dimension 0.8 m$\times$8 m has little stirring effect, though its length is several wavelengths. When the width of the single-plate stirrer is increased to 1.6 m, field strengthes change a lot during one stirrer rotation cycle. This phenomena indicates that the width of the stirrer should be large enough to make the stirrer effective. With the five-paddle stirrer, more drastic variations are observed during one stirrer rotation cycle. This is reasonable and expected, since the five-paddle stirrer introduces more irregularities during one stirrer rotation cycle.

Figures 4.17-4.19 show the electric field strength distribution along a plane (x$\in$[1 m, 7.5 m], y$\in$[4 m, 10 m], and z=3 m) in the RC. The electric field strength distribution
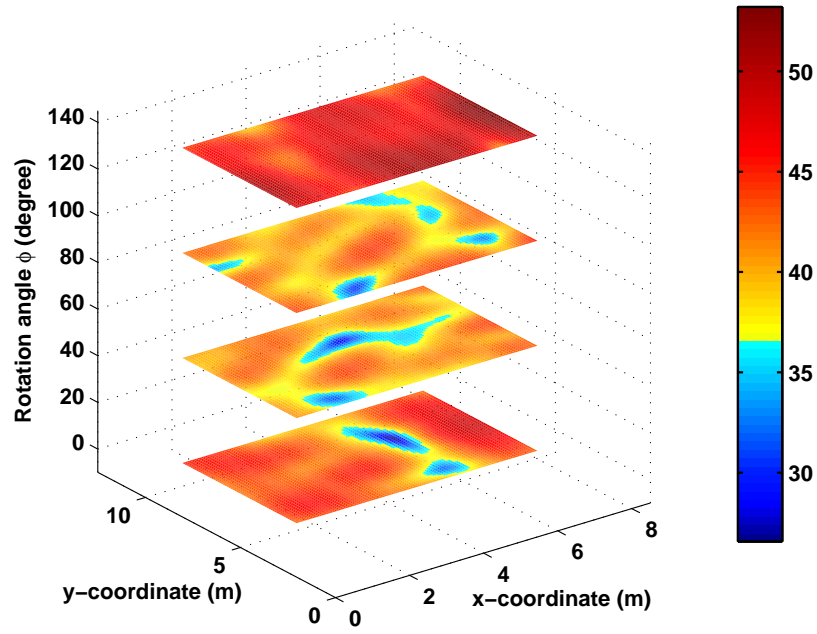
Figure 4.18: Distribution of E_r along a plane in the RC at four stirrer positions with excitation frequency of 82 MHz. The stirrer is the single-plate stirrer of dimension 1.6 m× 8 m.
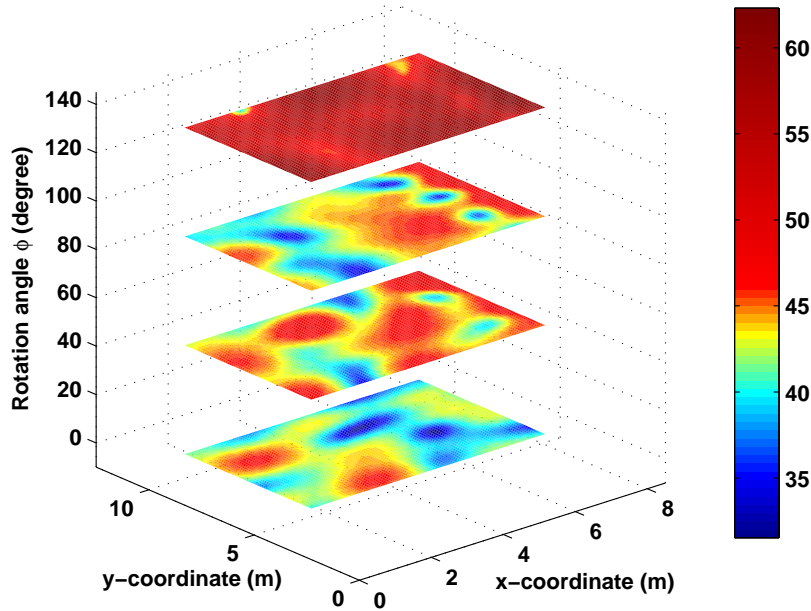
Figure 4.19: Distribution of E_r along a plane in the RC at four stirrer positions with excitation frequency of 82 MHz. The stirrer is the five-paddle stirrer illustrated in Figure 4.13.

is plotted at four stirrer positions, which are $\phi = 0^o$, 45°, 90°, and 135°. Figure 4.17 indicates that the small single-plate stirrer doesn't cause noticeable variation of the electric field strength distribution. With the larger single-plate stirrer and the five-paddle stirrer, the electric field strength distribution changes a lot as the stirrer rotates, which can be observed in Figures 4.18 and 4.19. When calculating the electric field strength, the spatial step size is 0.1 m in both x- and y-directions. Therefore, for one stirrer position, the electric field strength is calculated at 4026 points. If FEKO is used, it will take a long time to calculate the electric field strength at such a large number of field points. This is because FEKO needs to calculate the integral over a large cavity in computing the electric field strength. In the proposed method, electric field strength can be quite efficiently calculated using the field expansion (4.12). In calculating the electric field strength at 4026 points, the proposed method only takes 1.7 seconds. Therefore, the proposed method renders efficient calculation of electric field strength at a large number of field points, which is of great interest in RC modeling.

To further evaluate the performance of each stirrer, the number of independent samples is calculated using the first-order autoregressive model presented in [103]. The number of independent samples N' is calculated using the following formula [103]:

$$N' = N \times \frac{1 - \rho}{1 + \rho} \times 0.52^2 \times \left(\frac{\hat{\mu}_y}{\hat{\sigma}_y}\right)^2, \tag{4.36}$$

where

$$\hat{\mu}_y = \frac{1}{N} \sum_{t=1}^{N} y_t,$$

$$\hat{\sigma}_y^2 = \frac{1}{N - 1} \sum_{t=1}^{N} (y_t - \hat{\mu}_y)^2,$$

$$\rho = \frac{Cov(Y_1, Y_2)}{\sqrt{(Var(Y_1)Var(Y_2))}}.$$

Table 4.2: Number of Independent Samples for Different Stirring Approaches Using Various Stirrers

	Independent sample size-M*(E_x)	Independent sample size-MP3*	Independent sample size-MPOS8*(E_x)
Single-plate stirrer (1.6 m× 8 m)	2	5	10
Five-paddle stirrer	3	8	16

* M: mechanical stirring only; MP3: mechanical stirring and three-axis polarization stirring; MPOS8: mechanical stirring and position stirring at eight positions.

N is the total number of samples. y_t is the t-th sample. Y_1 is the collection of y_t, and Y_2 is obtained by cyclic exchange of Y_1. Namely,

$$Y_1 = [y_1, y_2...y_{N-1}, y_N], Y_2 = [y_2, y_3...y_N, y_1].$$

The terms $'Cov'$ and $'Var'$ denote the covariance and variance, respectively.

N' is calculated for different stirrers with three stirring approaches, which are mechanical stirring, mechanical and polarization stirring, and mechanical and position stirring. For mechanical stirring, the magnitude of E_x is sampled at the center of the RC for every stirrer position. In mechanical and polarization stirring, the magnitudes of three orthogonal field components are sampled at the center of the RC for every stirrer position. Mechanical and position stirring samples the magnitude of E_x at a few locations for one stirrer position. In this work, field points for positions stirring are chosen as the eight corners of a cuboid centered at (4 m, 6.5 m, 3 m). Dimensions of the cuboid are 2 m, 1.5 m, and 3 m in the x, y, and z-directions, respectively.

Table 4.2 presents the number of independent samples obtained using different stirrers with various stirring approaches. Results for the single-plate stirrer (0.8 m× 8

Table 4.3: Time and Memory Cost for One Stirrer Position and One Frequency Point with the Proposed Hybrid Method

Stirrer type	Number of Unknowns[*]	Total CPU time (seconds)	Peak memory (GB)
Single-plate stirrer (0.8 m×8 m)	3915	183	0.66
Single-plate stirrer (1.6 m×8 m)	4155	289	0.85
Five-paddle stirrer	4206	329	0.88

[*] Grid sizes are the same as those given in Table 5.1.

m) are not shown since it fails to generate independent samples. Table 4.2 shows that N' can be increased by combining mechanical stirring with other stirring methods. Furthermore, the five-paddle stirrer generates larger N' than the single-plate stirrer. However, N' is not large for all cases, which indicates that the stirring efficiency is not good. Optimized design of the stirrer may improve the stirring efficiency.

Table 4.3 presents the memory cost and total CPU time for one stirrer position. For the three RCs, the proposed method achieves the analysis of one stirrer position in a few hundred seconds, while FEKO may take thousands of seconds CPU time. The maximum peak memory cost in the three cases is 0.88 GB. It should be noted that the memory cost and CPU time are affected not only by the number of unknowns, but also by the sparsity of the left hand side matrix of (4.33). Therefore, the memory cost and CPU time for the second and third stirrers are different, though the numbers of unknowns are similar. However, the left hand side matrix of (4.33) is always sparse, because its major part is the differentiation matrix. Therefore, the memory costs presented in this work are representative.

Lastly, the proposed method is used to model the RC with five-paddle stirrer at 164
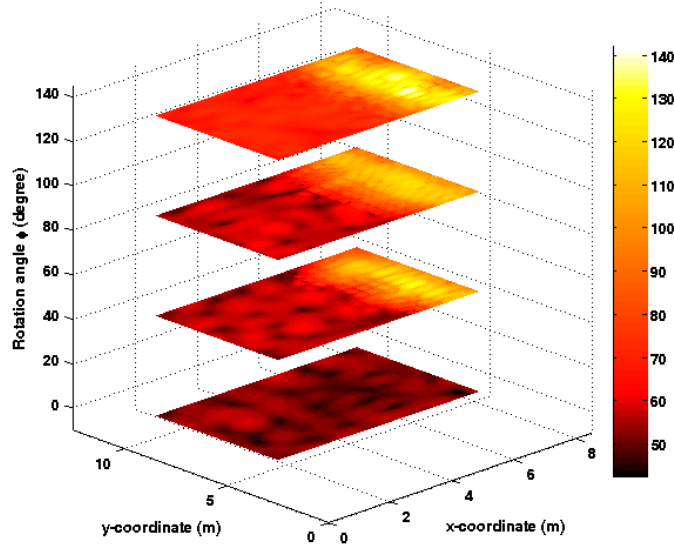
Figure 4.20: Distribution of E_r along a plane in the RC at four stirrer positions with excitation frequency of 164 MHz. The stirrer is the five-paddle stirrer illustrated in Figure 4.13.

MHz to investigate its ability in modeling a larger RC. The simulation is conducted on an IBM x3950M2 server with 48 cores and 256 GB RAM. Every core has a clock speed of 2.66 GHz, and one core is used in this work. For this example, the number of unknowns is 34943. Four stirrer positions are simulated. Figure 4.20 illustrates the field distribution along a plane (x∈[1 m, 7.5 m], y∈[4 m, 10 m], and z=3 m) in the RC at four stirrer positions. For one stirrer position, the simulation takes 1.94 hours CPU time and 45.57 GB memory. In this simulation, the memory cost is dominated by the solution of matrix equation. To avoid the solution of matrix equation, the matrix free method [94] can be used, and its application to the proposed method will be discussed in the next chapter.

4.4 Concluding Remarks

This chapter has described a new hybrid technique combining the DSC method and MoM for efficient modeling of a 3-D RCs. The RC modeling has been implemented

in two steps by replacing the metallic stirrer with a current sheet and enforcing the tangential electric field along the stirrer surface to be zero. In the first step, the tangential electric field along the stirrer surface is enforced to be zero by the application of an EFIE. In the second step, the current sheet and the original current source are taken as the excitation of the large metallic cavity. The MoM is used to solve the EFIE in the first step, and the DSC method is adopted to solve the cavity problem in the second step. The two steps are combined together by the equivalence principle.

The proposed hybrid method combines the flexibility of the MoM and the high efficiency of the DSC method. Employing the geometry flexibility of RWG basis, it can be used to model stirrers of arbitrary shape. With the high efficiency of the DSC method, the proposed hybrid method has been shown to be ten times as fast as FEKO. The memory cost by the proposed method is also less than that of FEKO. With a single personal computer, it takes the proposed hybrid method a few hundred seconds in analyzing one stirrer position of a practical medium-sized RC, for which FEKO may need thousands of seconds CPU time. Meanwhile, with the field expansion (4.12), the proposed method can efficiently calculate the electric field strength at a large number of field points.

For simplicity, only a point source is considered in this chapter. However, with the flexibility of the regularization technique, line or surface sources can be easily modeled using the proposed method. Furthermore, transmitting antennas can also be taken into account using the hybrid method, which will be discussed in the next chapter. Due to the usage of a direct solver, the memory requirement is high in solving a large scale matrix equation. In chapter 5, the matrix free method [94] will be combined with proposed method to reduce the memory usage drastically.

Chapter 5

Memory-Efficient Modeling of RCs Using Hybrid RUDSC-MoM

5.1 Introduction

Memory requirement of RC modeling is usually high due to the usage of direct solvers. Among existing methods, the cavity Green's function method [20, 28] greatly reduces the memory requirement through avoiding direct modeling of the cavity. However, as the size of the object inside the cavity increases, filling the interaction matrix may require long CPU time in cavity Green's function method. Although the hybrid DSC-MoM technique presented in the last chapter consumes less memory compared to many conventional numerical methods, its memory requirement is still high due to the usage of a direct solver, which limits the frequency range of RC modeling.

A recent advancement in cavity modeling is the RUDSC method. The recursive update (RU) method [94] is also known as the matrix free method [95], which means it doesn't need to solve a matrix equation. Therefore, the RU method is very useful when conventional iterative solvers fail. Furthermore, the RUDSC method renders low

memory consumption because it only needs storing two sparse differentiation matrices. On the other hand, the RU method can not be directly applied in the hybrid DSC-MoM method because the matrix free method is developed for solving differential equations only.

This chapter presents a hybrid RUDSC-MoM method for memory-efficient analysis of RCs. In the hybrid RUDSC-MoM method, the cavity is efficiently modeled by the RUDSC method, and antennas and stirrers are simulated using the flexible MoM. In order to solve DSC and MoM unknowns separately, a layer-based elimination algorithm is utilized to eliminate the DSC unknowns. The MoM unknowns are then solved using a direct solver. Once the solution for the MoM model is obtained, the original RC is equivalent to a cavity excited by known current sources. The equivalent problem is finally solved using the RUDSC method. The proposed method avoids the non-convergence problem encountered by conventional iterative solvers in RC analysis. Taking advantage of the layer-based elimination algorithm and the RU technique, the memory requirement of the new hybrid method is much smaller than that of using a direct solver, which extends RC analysis to higher frequencies. Numerical simulations are presented to show the efficacy of the proposed method.

The rest of this chapter is organized as follows. Section 5.2 describes the proposed method in detail and analyzes its complexity. Section 5.3 demonstrates the validity and efficiency of our proposed method through numerical examples. Efficacy of RUDSC method for cavity modeling is demonstrated, and choice of parameters in RUDSC method is studied. Results from the hybrid RUDSC-MoM method are compared with those from alternative methods to validate the proposed method. Advantages of the new hybrid method are demonstrated through comparison with existing methods. Numerical experiments are conducted to study the computational and

storing requirement of the proposed method. Finally, Section 5.4 concludes the work descried in this chapter.

5.2 Formulation

In this section, the hybrid DSC-MoM method is extended to take the transmitting antenna into consideration. RUDSC modeling of a cavity is also introduced and its hybridization with MoM is described. Algorithm complexity of the proposed hybrid method is finally analyzed.

5.2.1 Hybrid DSC-MoM Analysis of an RC

In the last chapter, the hybrid DSC-MoM method was developed for the analysis of 3-D RCs excited using a point current source. In this subsection, the hybrid DSC-MoM method is extended to account for the transmitting antenna. In the hybrid method, Maxwell's equations of differential form are used to describe fields in a cavity, and integral equations are adopted to simulate the conducting stirrer and antenna inside the RC. Discretizing differential and integral equations and coupling solutions of these equations using the equivalence principle, one can obtain the following matrix equation

$$\mathbf{A}\mathbf{x} = \mathbf{b}, \tag{5.1}$$

where $\mathbf{x} = \begin{bmatrix} \mathbf{e_{DSC}} & \mathbf{j_S} & \mathbf{i_a} \end{bmatrix}^T$, $\mathbf{b} = \begin{bmatrix} \mathbf{0} & \mathbf{0} & -\mathbf{e_0^i} \end{bmatrix}^T$, and

$$\mathbf{A} = \begin{bmatrix} \mathbf{D} + C_1\mathbf{I} & -C_2\mathbf{R_S} & -C_2\mathbf{R_a} \\ \mathbf{P_S} & -\mathbf{Z} & \mathbf{0} \\ \mathbf{P_a} & \mathbf{0} & -\mathbf{Z_a} \end{bmatrix}. \tag{5.2}$$
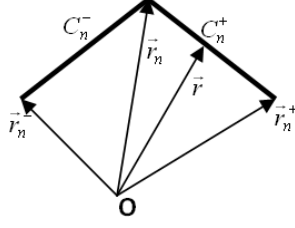
Figure 5.1: Two wire segments C_n^+ and C_n^-.

The superscript T denotes the transpose operation. $\mathbf{e_{DSC}}$, $\mathbf{j_S}$, and $\mathbf{i_a}$ are unknown expansion coefficients of the electric field, induced current on stirrer and excitation source from the antenna, respectively. $\mathbf{e_{DSC}}$ represents the DSC unknowns. $\mathbf{j_S}$ and $\mathbf{i_a}$ constitute the MoM unknowns. $\mathbf{D} = \mathbf{D_h}\mathbf{D_e}$, $C_1 = -\omega^2\mu\epsilon$, and $C_2 = -j\omega\mu$. $\mathbf{I}$ is the identity matrix. $\mathbf{D_h}$ and $\mathbf{D_e}$ are differentiation matrices arising from curl operators on magnetic and electric fields, respectively. Definition of matrices $\mathbf{R_S}$, $\mathbf{Z}$ and $\mathbf{P_S}$ can be found in Chapter 4. Matrix $\mathbf{Z_a}$ is the MoM interaction matrix for a wire antenna[1], and $\mathbf{e_0^i}$ is the excitation vector due to the voltage source of the wire antenna. Details on calculation of $\mathbf{Z_a}$ and $\mathbf{e_0^i}$ can be found in [98]. Computation of $\mathbf{R_a}$ and $\mathbf{P_a}$ is elucidated in the next two paragraphs.

Since $\vec{I}_a$ is a line current source, its regularized form $\vec{I}_a^R$ at $\vec{r}_m$ is [96]

$$\vec{I}_a^R(\vec{r}_m) = \int_C \zeta_\epsilon(\vec{r}_m - \vec{r}')\vec{I}_a(\vec{r}')d\vec{r}', \tag{5.3}$$

where C represents the domain of $\vec{I}_a$. $\vec{r}_m$ is the position of the mth DSC grid point, and ζ_ϵ represents the regularized Dirac function defined in [96]. With a triangle basis function, $\vec{I}_a$ is expanded as

$$\vec{I}_a(\vec{r}) = \sum_{n=1}^{N_a} i_a^n \vec{s}_n(\vec{r}), \tag{5.4}$$

---

[1]In this work, we assume that the transmitting antenna for the RC is a wire antenna. Other types of antennas can be considered in a similar way as long as they can be modeled using the MoM.

where N_a is the total number of basis functions. $\vec{s}_n(\vec{r})$ represents the triangle basis function [98], which is defined as

$$\vec{s}_n(\vec{r}) = \left[\begin{array}{cc} \frac{\vec{r}_n^+ - \vec{r}}{l_n^+} & \vec{r} \in C_n^+ \\[2mm] \frac{\vec{r} - \vec{r}_n^-}{l_n^-} & \vec{r} \in C_n^- \\[2mm] 0 & \text{otherwise} \end{array}\right]. \tag{5.5}$$

C_n^+ and C_n^- are two wire segments as shown in Figure 5.1 . $\vec{r}_n^\pm$ represents the node of $C_n^\pm$ opposite to the common node of C_n^+ and C_n^-. $l_n^\pm$ is the length of $C_n^\pm$. Substituting (5.4) into (5.3), one obtains

$$\vec{I}_a^R(\vec{r}_m) = \sum_{n=1}^{N_a} i_a^n \int_{C_n} \zeta_\epsilon(\vec{r}_m - \vec{r}\,')\vec{s}_n(\vec{r}\,')d\vec{r}\,', \tag{5.6}$$

where C_n denotes the support of $\vec{s}_n$. Replacing the segmental integral with a Gaussian quadrature, (5.6) becomes

$$\vec{I}_a^R(\vec{r}_m) = \sum_{n=1}^{N_a} i_a^n \sum_{g=1}^{G} w_g \zeta_\epsilon(\vec{r}_m - \vec{r}\,'_{n,g})\vec{s}_n(\vec{r}\,'_{n,g}), \tag{5.7}$$

where $\vec{r}\,'_{n,g}$ is position of the gth integral point on C_n, and w_g is the weight for the gth integral point. Therefore, the regularization matrix $\mathbf{R_a}$ is defined as

$$R_a(m,n) = \frac{1}{2\pi a} \sum_{g=1}^{G} w_g \zeta_\epsilon(\vec{r}_m - \vec{r}\,'_{n,g})\vec{s}_n(\vec{r}\,'_{n,g}), \tag{5.8}$$

where a is the radius of the wire. The term $1/2\pi a$ is due to the conversion from $\vec{I}_a$ to $\vec{J}_a$.

Following the procedure in obtaining matrix $\mathbf{P_S}$ (refer to equations (4.21) to (4.32)

in Chapter 4), one can write matrix $\mathbf{P_a}$ as

$$\mathbf{P_a} = \frac{1}{C_2}\mathbf{Z_a^e}\mathbf{T_{hj}^a}\mathbf{W_a^h}\mathbf{D^e} + \mathbf{Z_a^c}\mathbf{T_{em}^a}\mathbf{W_a^e},$$

where elements in matrices $\mathbf{Z_a^c}$ and $\mathbf{Z_a^e}$ are defined as

$$Z_a^c(m,n) = -\int\int_{C_m} \vec{s}_m\left(\vec{r}\right) \cdot \left[\nabla \times \int\int_{S_b^n} \vec{f}_n\left(\vec{r}'\right) G\left(\vec{r},\vec{r}'\right) d\vec{r}'\right] d\vec{r}, \qquad (5.9)$$

$$Z_a^e(m,n) = -j\omega\mu\int\int_{C_m} \vec{s}_m\left(\vec{r}\right) \cdot \int\int_{S_b^n} \vec{f}_n\left(\vec{r}'\right) G\left(\vec{r},\vec{r}'\right) d\vec{r}' d\vec{r}$$

$$-\frac{1}{j\omega\epsilon}\int\int_{C_m} \nabla \cdot \vec{s}_m\left(\vec{r}\right) \left[\int\int_{S_b^n} \nabla' \cdot \vec{f}_n\left(\vec{r}'\right) G\left(\vec{r},\vec{r}'\right) d\vec{r}'\right] d\vec{r}. \qquad (5.10)$$

In (5.9) and (5.10), $\vec{s}_m$ is the triangle basis function used to expand the current on wire structures [98], and C_m denotes the support domain of $\vec{s}_m$. $\vec{f}_n$ is the RWG basis function [98] utilized to express the current on Huygens' box, and S_n is the effective domain of $\vec{f}_n$. Matrices $\mathbf{T_{hj}^a}$, $\mathbf{W_a^h}$, $\mathbf{T_{em}^a}$, and $\mathbf{W_a^e}$ have the same definition as $\mathbf{T_{hj}}$, $\mathbf{W^h}$, $\mathbf{T_{em}}$, and $\mathbf{W^e}$, respectively. Procedures for obtaining these matrices can be found in Chapter 4.

5.2.2 RUDSC Modeling of a Cavity

The RUDSC method starts with the time-domain Maxwell's equations of differential form

$$\frac{\partial \vec{E}(t)}{\partial t} = \frac{1}{\epsilon}\nabla \times \vec{H}(t) - \frac{\sigma}{\epsilon}\vec{E}(t) - \frac{1}{\epsilon}\vec{J}(t), \qquad (5.11)$$

$$\frac{\partial \vec{H}(t)}{\partial t} = -\frac{1}{\mu}\nabla \times \vec{E} - \frac{\sigma^*}{\mu}\vec{H}(t), \qquad (5.12)$$
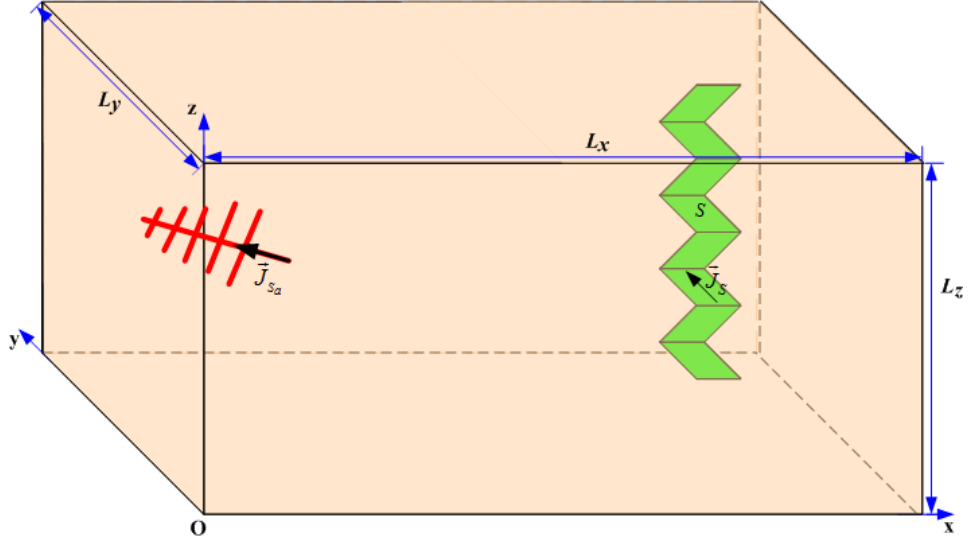
Figure 5.2: A cavity excited by known current sources.

where σ and σ^* denote the electric and magnetic conductivities, respectively. In this work, the current excitation $\vec{J}(t)$ includes the induced current on the stirrer and the excitation source from the antenna, which are denoted by $\vec{J}_S(t)$ and $\vec{J}_{S_a}(t)$, respectively, as shown in Figure 5.2.

With a time periodic excitation of angular frequency ω, time domain electromagnetic fields have the form $\vec{E}(t) = \hat{E}(t)e^{j\omega t}$, and $\vec{H}(t) = \hat{H}(t)e^{j\omega t}$, where $\hat{E}(t)$ and $\hat{H}(t)$ are constants in the steady state. Meanwhile, the excitation $\vec{J}(t)$ is written as $\hat{J}e^{j\omega t}$. Replacing temporal derivatives with respect to $\vec{E}(t)$ and $\vec{H}(t)$ by the FD, the following equations are obtained

$$\frac{\hat{E}^{n+1}e^{j\omega\frac{\tau}{2}} - \hat{E}^n e^{-j\omega\frac{\tau}{2}}}{\tau} = \frac{1}{\epsilon}\nabla \times \hat{H}^{n+\frac{1}{2}} - \frac{\sigma}{\epsilon}\hat{E}^{n+1}e^{j\omega\frac{\tau}{2}} - \frac{1}{\epsilon}\hat{J}e^{-j\omega\frac{\tau}{2}}, \tag{5.13}$$

$$\frac{\hat{H}^{n+\frac{1}{2}}e^{j\omega\frac{\tau}{2}} - \hat{H}^{n-\frac{1}{2}}e^{-j\omega\frac{\tau}{2}}}{\tau} = -\frac{1}{\mu}\nabla \times \hat{E}^n - \frac{\sigma^*}{\mu}\hat{H}^{n+\frac{1}{2}}e^{j\omega\frac{\tau}{2}}, \tag{5.14}$$

where τ denotes the marching step size, n is the index of marching steps, $\hat{E}^n$ and $\hat{H}^{n+\frac{1}{2}}$ are the values of $\hat{E}(t)$ and $\hat{H}(t)$ at points $n\tau$ and $n\tau + \frac{\tau}{2}$, respectively. Rearranging

equations (5.13) and (5.14), one can derive the following RU scheme

$$\hat{E}^{n+1} = C_3 \left(\hat{E}^n + \frac{\tau}{\epsilon} e^{j\omega \frac{\tau}{2}} \nabla \times \hat{H}^{n+\frac{1}{2}} - \frac{\tau}{\epsilon} \hat{J} \right), \tag{5.15}$$

$$\hat{H}^{n+\frac{1}{2}} = C_4 \left(\hat{H}^{n-\frac{1}{2}} e^{-j\omega \frac{\tau}{2}} - \frac{\tau}{\mu} \nabla \times \hat{E}^n \right), \tag{5.16}$$

where

$$C_3 = \frac{\epsilon}{\epsilon + \sigma\tau} e^{-j\omega\tau}, \text{ and } C_4 = \frac{\mu}{\mu + \sigma^*\tau} e^{-j\omega \frac{\tau}{2}}.$$

It has been shown that the RU scheme in equations (5.15) and (5.16) is convergent as long as

$$\tau \leq h\sqrt{\frac{\epsilon\mu}{8}}, \tag{5.17}$$

where h is the spatial grid size [94]. It can be shown that $\hat{E}^n$ and $\hat{H}^{n+\frac{1}{2}}$ will be solutions of the frequency-domain Maxwell's equations if the following two conditions are satisfied

$$\tau \leq \frac{\text{tol}_1}{\omega}, \tag{5.18}$$

$$\frac{||\hat{E}^{n+1} - \hat{E}^n||_2}{||\hat{E}^n||_2} \leq \text{tol}_2, \text{ and } \frac{||\hat{H}^{n+\frac{1}{2}} - \hat{H}^{n-\frac{1}{2}}||_2}{||\hat{H}^{n-\frac{1}{2}}||_2} \leq \text{tol}_2. \tag{5.19}$$

In this work, the value of τ is chosen according to (5.17) and (5.18), and the RU is continued until (5.19) is satisfied. The choice of tol_1 and tol_2 will be studied in Section 5.3.1, and it will be shown that tol_1 and tol_2 can be set to 6×10^{-2} and 1×10^{-4}, respectively.

In order to numerically find the steady state values of $\hat{E}^{n+1}$ and $\hat{H}^{n+\frac{1}{2}}$, the DSC method [75] is adopted to approximate the curl operators. Advantages of RUDSC over RU finite difference (RUFD) [94, 95] will be demonstrated in Section 5.3. Similar

91

to hybrid DSC-MoM in Chapters 3 and 4, the regularization technique [96] is used to model arbitrarily oriented current sources in structured grids. Applying the DSC method to equations (5.15) and (5.16), the following equations are obtained

$$\mathbf{e}^{n+1} = C_3 \left(\mathbf{e}^n + \frac{\tau}{\epsilon} e^{j\omega\frac{\tau}{2}} \mathbf{D}_h \mathbf{h}^{n+\frac{1}{2}} - \frac{\tau}{\epsilon} \left(\mathbf{R_a i_a} + \mathbf{R_S j_S} \right) \right), \tag{5.20}$$

$$\mathbf{h}^{n+\frac{1}{2}} = C_4 \left(\mathbf{h}^{n-\frac{1}{2}} e^{-j\omega\frac{\tau}{2}} - \frac{\tau}{\mu} \mathbf{D}_e \mathbf{e}^n \right), \tag{5.21}$$

where $\mathbf{e}^{n+1}$ and $\mathbf{h}^{n+\frac{1}{2}}$ are vectors consisting of the spatial expansion coefficients of $\hat{E}^{n+1}$ and $\hat{H}^{n+\frac{1}{2}}$, respectively. Starting from $n = 0$, equations (5.20) and (5.21) are recursively updated until condition (5.19) is satisfied. Solution to the DSC unknowns is then obtained. It should be noted that the initial values of $\mathbf{e}^{n+1}$ and $\mathbf{h}^{n+\frac{1}{2}}$ will affect the convergence of RU method. As suggested in [94], a robust choice is to set the initial values to zeros.

5.2.3 Hybridization of RUDSC and MoM

The RU method can not be used to solve MoM unknowns because it is developed for solving differential equations only. In order to hybridize RUDSC with MoM, the DSC unknowns are first eliminated using a layer-based elimination algorithm, and the MoM unknowns are obtained using a direct solver. The DSC unknowns can then be derived using the RU method.

The layer-based elimination algorithm was first proposed by Jin for finite element (FE) modeling of scattering from a large cavity [104–106], and it has been widely used in the FE analysis of scattering from large objects with a deep cavity [107–110]. Analyzing scattering from a large open cavity is a challenging problem in CEM, and it is similar to RC modeling because an internal cavity is modeled in both problems.

Besides layer-based elimination algorithm, the connection scheme [111] is another way of modeling scattering from a deep open cavity, and it was used together with MLFMA for efficient analysis of scattering from a large object with a deep cavity [112]. In either layer-based elimination algorithm or connection scheme, the cavity is divided into a few sections along its longest direction, and the whole cavity is modeled section by section to reduce the memory cost.

In this thesis, a layer-based elimination algorithm is developed to eliminate the DSC unknowns with low memory cost. This section first introduces the layer division of a cavity and then describes the elimination of DSC unknowns in a layer-by-layer manner.

In (5.2), the bandwidth of matrix $\mathbf{D}$ will be limited if the elements of $\mathbf{e_{DSC}}$ are arranged properly. Therefore, one may utilize the characteristics of matrix $\mathbf{D}$ to eliminate unknowns $\mathbf{e_{DSC}}$ with low memory consumption. Figure 5.3 illustrates one way to order the DSC unknowns. The cavity is divided into many layers along its longest dimension, which is the z-axis. In Yee's grid, grid points of the three orthogonal electric field components E_x, E_y and E_z are allocated as follows: E_x and E_y grid points will be laid on the same plane, which is denoted as E_x, E_y sub-layer. E_z grid points will be on another plane, which is named as E_z sub-layer. As shown in Figure 5.3, a E_z sub-layer is $0.5d_z$ away from its neighboring E_x, E_y sub-layer, where d_z is the DSC grid size in the z-direction. In Figure 5.3, the first E_x, E_y sub-layer and the first E_z sub-layer constitutes the first layer. The next two sub-layers will form the second layer. Following this way and going from the bottom towards the top of the cavity, one will have N_L layers, where $N_L = L_z/d_z$. Besides the N_L layers, there is another E_z sub-layer remaining (c.f. Figure 5.3). It is denoted as the last sub-layer of E_z, which contains N_{S_z} unknowns.

93
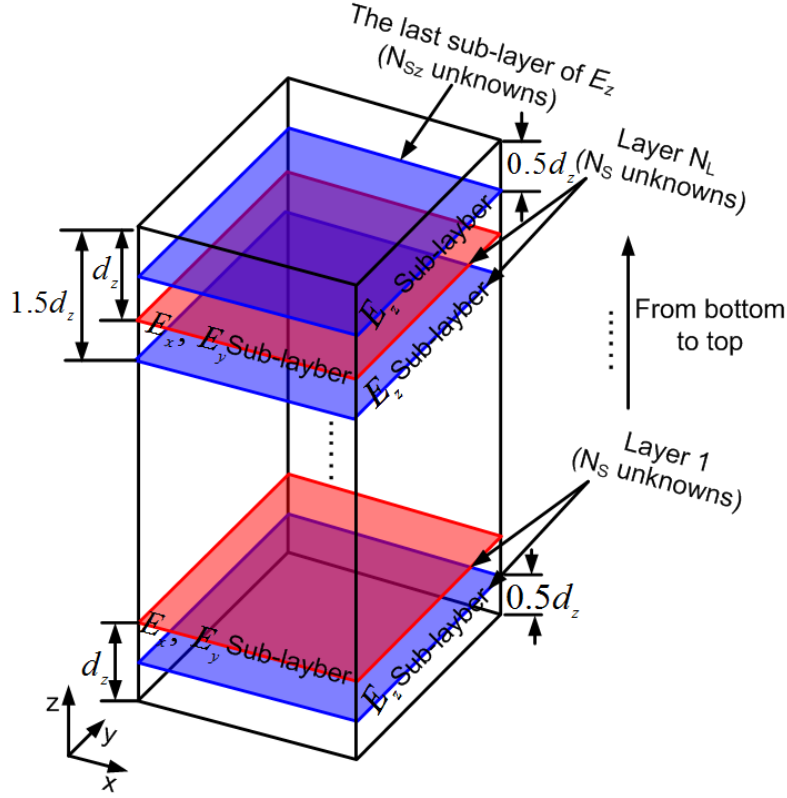
Figure 5.3: Layer division of a cavity along its longest direction. E_x, E_y sub-layer denotes a sub-layer where E_x and E_y grid points are defined, and E_z sub-layer represents a sub-layer where E_z grid points are located. One layer consists of a E_x, E_y sub-layer and a E_z sub-layer.

Arranging the elements of $\mathbf{e_{DSC}}$ as shown Figure 5.3, matrix $\mathbf{D}$ will be bandlimited, and its half bandwidth is $(M+1)N_S$, where $M = 0.5O_N^z$. O_N^z is the order of the basis function in the z-direction, and N_S is the number of unknowns in one layer. Utilizing the limited bandwidth of $\mathbf{D}$, $\mathbf{e_{DSC}}$ can be eliminated from the bottom to the top in a layer-by-layer manner. When eliminating the first N_S unknowns (unknowns in the first layer), only a small portion of matrix $\mathbf{A}$ is involved due to the limited bandwidth of matrix $\mathbf{D}$. The memory requirement of eliminating unknowns in one layer is thus not large. After the first N_S unknowns are eliminated, the second N_S unknowns (unknowns in the second layer) are eliminated in the same way, and the memory can

be reused. This process is repeated from the bottom to the top of the cavity until the first N_{DSC} unknowns are eliminated, where $N_{DSC} = N_L N_S + N_{S_z}$ is the number of unknowns in the DSC model. The aforementioned elimination process will change (5.1) into a new matrix equation

$$
\begin{bmatrix}
\mathbf{D}' & -C_2 \mathbf{R}'_{\mathbf{S}} & -C_2 \mathbf{R}'_{\mathbf{a}} \\
\mathbf{0} & -\mathbf{Z}'_{\mathbf{S}} & \mathbf{Z}'_{\mathbf{Sa}} \\
\mathbf{0} & \mathbf{Z}'_{\mathbf{aS}} & -\mathbf{Z}'_{\mathbf{a}}
\end{bmatrix}
\begin{bmatrix}
\mathbf{e_{DSC}} \\
\mathbf{j_S} \\
\mathbf{i_a}
\end{bmatrix}
=
\begin{bmatrix}
\mathbf{0} \\
\mathbf{0} \\
-\mathbf{e_0^i}
\end{bmatrix}.
\tag{5.22}
$$

From equation (5.22), one can solve $\mathbf{j_S}$ and $\mathbf{i_a}$ using a direct solver, because N_{MoM} is relatively small, where N_{MoM} is the total length of $\mathbf{j_S}$ and $\mathbf{i_a}$. It should be noted that matrix $\mathbf{D}'$ is not sparse after the layer-by-layer elimination process. Matrices $\mathbf{R}'_{\mathbf{S}}$ and $\mathbf{R}'_{\mathbf{a}}$ are of large dimension, and they are not stored in the memory. For the convenience of understanding, the aforementioned algorithm is described in detail using a pseudocode in Algorithm 1. In Algorithm 1, matrix $\mathbf{D}$ is divided into many blocks. One block represents the relationship between unknowns inside one layer or in two different layers. The first and second subscripts of a matrix variable denote the block numbers in row and column directions, respectively. The symbol '←' denotes the assignment operation, and '$m : n$' means from m to n. '$*$' represents matrix multiplication operation. Furthermore, $\mathbf{P}=[\mathbf{P_S}\ \mathbf{P_a}]^T$, $\mathbf{R}=[-C_2\mathbf{R_S}\ -C_2\mathbf{R_a}]$, $\mathbf{D^t} = \mathbf{D} + C_1\mathbf{I}$, and

$$
\mathbf{Z_{Sa}} =
\begin{bmatrix}
-\mathbf{Z} & \mathbf{0} \\
\mathbf{0} & -\mathbf{Z_a}
\end{bmatrix}.
\tag{5.23}
$$

Matrices $\mathbf{P}$ and $\mathbf{R}$ are divided into N_L+1 blocks along their column and row directions, respectively. The first N_L blocks of matrices $\mathbf{P}$ and $\mathbf{R}$ are of dimension $N_{MoM} \times N_S$

Algorithm 1 The Layer-Based Elimination Algorithm

$\mathbf{D}^F \leftarrow \mathbf{D}^\mathbf{t}_{1:M+1,1:M+1}$

$\mathbf{P}^F \leftarrow \mathbf{P}_{1,1:M+1}$

$\mathbf{R}^F \leftarrow \mathbf{R}_{1:M+1,1}$

for $i = 1 : N_L$ **do**

  Invert $\mathbf{D}^F_{1,1}$ and store the inverse in $\mathbf{DI}$ $O(N_S^3)$; $O(N_S^2 N_{MoM})$

  $\mathbf{F} \leftarrow -\mathbf{DI} * \mathbf{R}^F_{1,1}$

  for $R = 2 : M + 1$ **do** $O(N_S^2 N_{MoM})$

    $\mathbf{R}^F_{R-1,1} \leftarrow \mathbf{R}^F_{R,1} + \mathbf{D}^\mathbf{t}_{R,1} * \mathbf{F}$ $O(MN_S^2 N_{MoM})$

  end for

  $\mathbf{Z_{Sa}} \leftarrow \mathbf{Z_{Sa}} + \mathbf{P}_{1,1} * \mathbf{F}$ $O(N_{MoM}^2 N_S)$

  for $C = 2 : M + 1$ **do** $O(N_S^3)$

    $\mathbf{F} \leftarrow -\mathbf{DI} * \mathbf{D}^F_{1,C}$ Most time consuming part

    for $R = 2 : M + 1$ **do** $O(MN_S^3)$; $O(N_{MoM}N_S^2)$

      $\mathbf{D}^F_{R-1,C} \leftarrow \mathbf{D}^F_{R,C} + \mathbf{D}^F_{R,1} * \mathbf{F}$ $O[M(N_S^3 + MN_S^3 + N_{MoM}N_S^2)]$

    end for

    $\mathbf{P}^F_{1,C} \leftarrow \mathbf{P}^F_{1,C} + \mathbf{P}^F_{1,1} * \mathbf{F}$

  end for

  Replace $\mathbf{D}^F_{1:M,1:M}$ with $\mathbf{D}^F_{1:M,2:M+1}$

  Replace $\mathbf{P}^F_{1,1:M}$ with $\mathbf{P}^F_{1,2:M+1}$

  if $i + M + 1$ leq $N_z + 1$ **then**

    $\mathbf{D}^F_{1:M,M+1} \leftarrow \mathbf{D}^\mathbf{t}_{i+1:i+M,i+M+1}$

    $\mathbf{D}^F_{M+1,1:M+1} \leftarrow \mathbf{D}^\mathbf{t}_{i+M+1,i+1:i+M+1}$

  end if

end for

Invert $\mathbf{D}^F_{1,1}(1 : N_z, 1 : N_z)$ and store the inverse in $\mathbf{DI}$

$\mathbf{F} = -\mathbf{DI} * \mathbf{R}^F_{1,1}(1 : N_z, 1 : N_{MoM})$

$\mathbf{Z_{Sa}} = \mathbf{Z_{Sa}} + \mathbf{P}_{1,1}(1 : N_{MoM}, 1 : N_z) * \mathbf{F}$

$\mathbf{x} = \mathbf{Z_{Sa}^{-1}} * \mathbf{b}(N_{DSC} + 1 : N_{DSC} + N_{MoM})$

$O\{N_S^3 + N_S^2 N_{MoM} + MN_S^2 N_{MoM} +$
$N_{MoM}^2 N_S + M(N_S^3 + MN_S^3 + N_{MoM}N_S^2)\}$
$= O\{N_S^3 + N_S^2(N_{MoM} + MN_S) +$
$2MN_S^2 N_{MoM} + N_{MoM}^2 N_S + M^2 N_S^3\}$
$= O\{N_S^3 + N_S^2(N_{MoM} + MN_S) +$
$N_S(N_{MoM} + MN_S)^2\}$

and $N_S \times N_{MoM}$, respectively. Dimensions of the last blocks of matrices $\mathbf{P}$ and $\mathbf{R}$ are respectively $N_{MoM} \times N_{Sz}$ and $N_{Sz} \times N_{MoM}$.

Considering the complexity of matrix inversion and counting the number of multiplication operations, one can estimate the computational complexity of the layer-based elimination algorithm from Algorithm 1.

The proposed layer-based elimination algorithm has a similar concept with the one in [104]. They are different in the following two aspects. First, the former is designed

for the hybrid DSC-MoM, and the latter is for the FEM. Therefore, definition of a layer is different in these two cases. Second, the method presented in [104] is developed for analyzing scattering from a deep cavity. In that case, the external and internal problems are separated by the conducting cavity, and they are coupled through the opening of the cavity. Therefore, the layer-based elimination process is independent of the external problem in the case of scattering analysis. In RC modeling, the MoM and DSC unknowns are directly coupled. Therefore, the MoM interaction matrices are affected by the elimination process.

For scattering problems, one is not interested in fields inside the cavity. On the other hand, fields inside the cavity are of the main interest in RC modeling. Since matrices $\mathbf{D}'$, $\mathbf{R}'_{\mathbf{S}}$, and $\mathbf{R}'_{\mathbf{a}}$ are not stored during the layer-based elimination process, $\mathbf{e_{DSC}}$ remains unsolved after the MoM solution is obtained, and it is derived using the RUDSC method.

5.2.4 Complexity Analysis

The most costly part in our proposed method is the layer-based elimination algorithm. In eliminating unknowns of one layer, $(MN_S + N_{MoM})$ columns of $(MN_S + N_{MoM})$ rows in matrix $\mathbf{A}$ are rewritten and stored. In the meanwhile, rows and columns corresponding to unknowns currently to be eliminated need storage. In order to store these elements, the memory requirement is $O\left[(MN_S + N_S + N_{MoM})^2\right]$. Therefore, the memory requirement of the layer-based elimination algorithm is quadratically dependent on M, N_S and N_{MoM}. In the pseudocode of Algorithm 1, the computational complexity of every matrix multiplication operation is indicated and the most time consuming part of Algorithm 1 is highlighted. The computational complexity for eliminating unknowns in one layer is $O\left[N_S^3 + N_S^2(MN_S + N_{MoM}) + N_S(MN_S + N_{MoM})^2\right]$
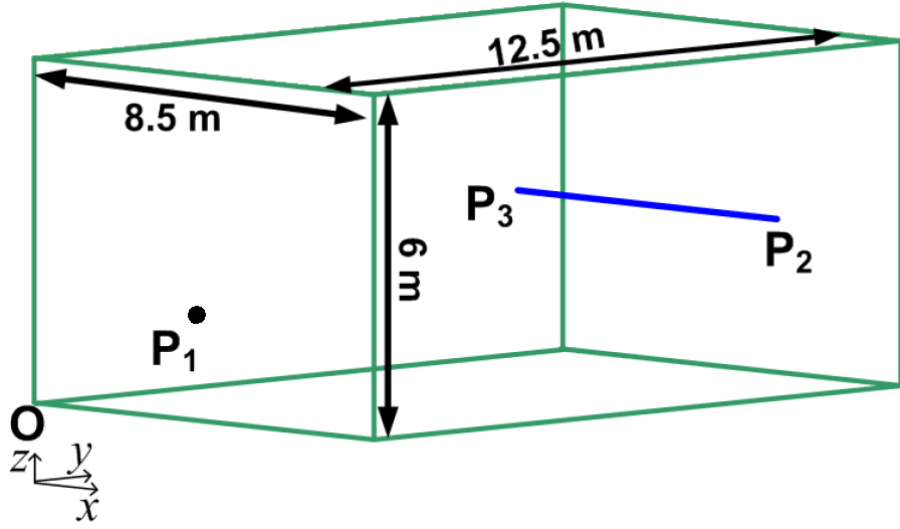
Figure 5.4: An empty cavity excited by a point current source. The current source is located at point P_1 (2 m, 2 m, 1.6 m). All three orthogonal components of the current is set to 1 A/m². Electric field is observed along the straight line connecting points P_2 (7.5 m, 10.5 m, 3 m) and P_3 (1 m, 10.5 m , 3 m).

(c.f. Algorithm 1 for derivation of computational complexity). Hence, the CPU time for the elimination of unknowns in one layer is cubically proportional to N_S, and quadratically dependent on M and N_{MoM}. Since the CPU time for every layer is approximately the same, the total CPU time is linearly dependent on N_L. With a fixed basis order, the memory requirement of RUDSC method is linearly dependent on N_{DSC}, and its computational complexity is $O(N_{DSC})$ for one step of update.

5.3 Numerical Simulations

Simulation results are presented in this section to demonstrate the performance of our proposed method. The RUDSC method is first studied via simulations on a cavity. The hybrid RUDSC-MoM is validated through comparison with existing methods. Complexity of the proposed method is then studied in detail. Numerical examples on a full-scale RC are presented to demonstrate the application of the proposed method. Unless otherwise stated, a twelfth-order basis is used in the DSC method, and grid
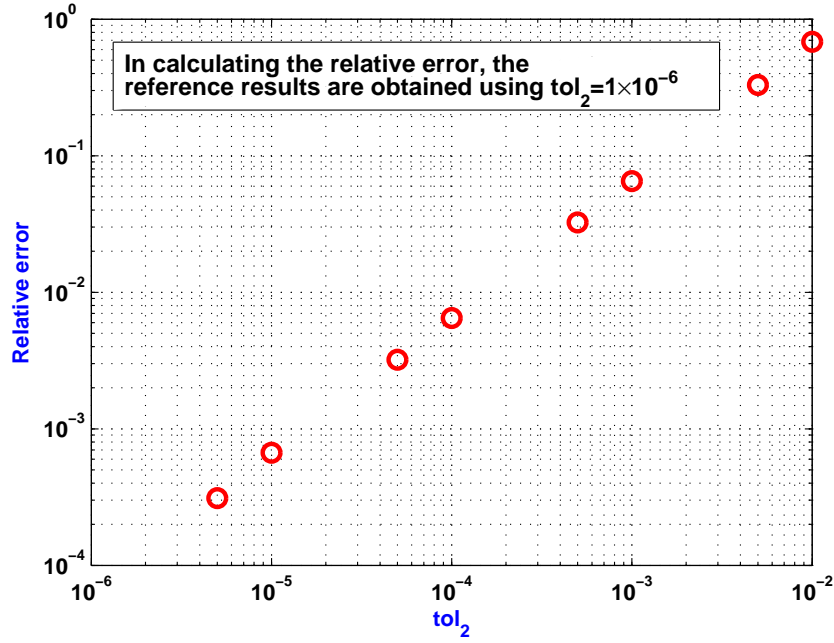
Figure 5.5: Accuracy of RUDSC method using different values of tol_2.

sizes of the DSC method and MoM are set to one fifth and one tenth of the wavelength, respectively. If not specified, a personal computer with two quad-core CPUs and a 8 GB RAM is used in this section, and one core is utilized to run the simulations.

5.3.1 Modeling a Cavity Using RUDSC Method

This subsection first discusses how to choose the values of tol_1 and tol_2. The RUDSC method is then validated against a direct solver and the commercial software FEKO, and its advantages are demonstrated through comparison with the RUFD method and the biconjugate gradient method. For all simulations in this subsection, the test model is a conducting cavity shown in Figure 5.4. σ^* and σ are set to zero and 2.218×10^{-6} S/m, respectively. All simulations in this subsection are conducted on a personal computer with a 2.66 GHz CPU and a 2 GB RAM.

tol_1 is chosen to ensure that $\sin(\frac{\omega\tau}{2})$ is in its linear region and the imaginary part

99

Table 5.1: Time and Memory Cost Comparisons Between RUFD and RUDSC

Frequency	Method	Unknowns No.	CPU time	Memory	Grid size (m)
82 MHz	RUFD	67,971	1.47 hours	6.6 MB	$h_x = 0.3696$, $h_y=0.3788$, $h_z=0.3750$
	RUDSC	7,779	0.48 hour	2.7 MB	$h_x = 0.7727$, $h_y=0.7353$, $h_z=0.7500$
200 MHz	RUDSC	133,482	14 hours	61 MB	$h_x = 0.3036$, $h_y=0.2976$, $h_z=0.3000$

of $e^{j\frac{\omega\tau}{2}}$ is close to zero. It is known that the sinusoidal function is in its linear region if its argument is below 0.1. Therefore, the imaginary part of $e^{j\frac{\omega\tau}{2}}$ is $\frac{\omega\tau}{2}$ if $\omega\tau$ is below 0.2. In simulations that follow, tol_1 is chosen to be 6×10^{-2} so that the imaginary part of $e^{j\frac{\omega\tau}{2}}$ is below 3×10^{-2}. tol_2 is a measure of the convergence of the RU scheme. Figure 5.5 shows the relative error versus the value of tol_2 in modeling the conducting cavity shown in Figure 5.4. The excitation frequency is 82 MHz. Figure 5.5 indicates that tol_2 can be chosen to be 1×10^{-4} in order to obtain a relative error of 1×10^{-2}.

Figure 5.6(a) presents the solution vector $\mathbf{e}$ computed using different methods. Good agreement is observed between the RUDSC method and the direct solver. Figure 5.6(b) illustrates $|E_x|$ along a straight line (defined in Figure 5.4) in the conducting cavity. Also shown in 5.6(b) are the results obtained using the RUFD method. Grid sizes in RUDSC and RUFD methods are set to be one-fifth and one-tenth of the wavelength, respectively. It is seen that the RUDSC method can obtain good agreement with FEKO, while the RUFD method fails to get good results using the grid size of one-tenth of the wavelength. Table 5.1 presents the CPU time and memory cost by the RUDSC and RUFD methods. Even without refining the grids, the RUFD method requires more CPU time and memory than the RUDSC method.
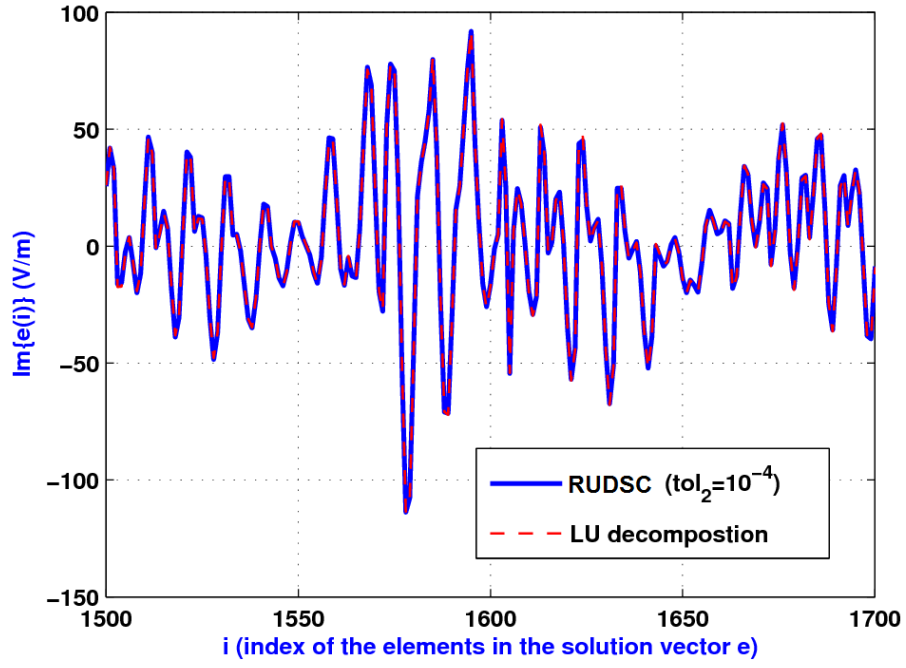
(a) Solution vector obtained using different methods.
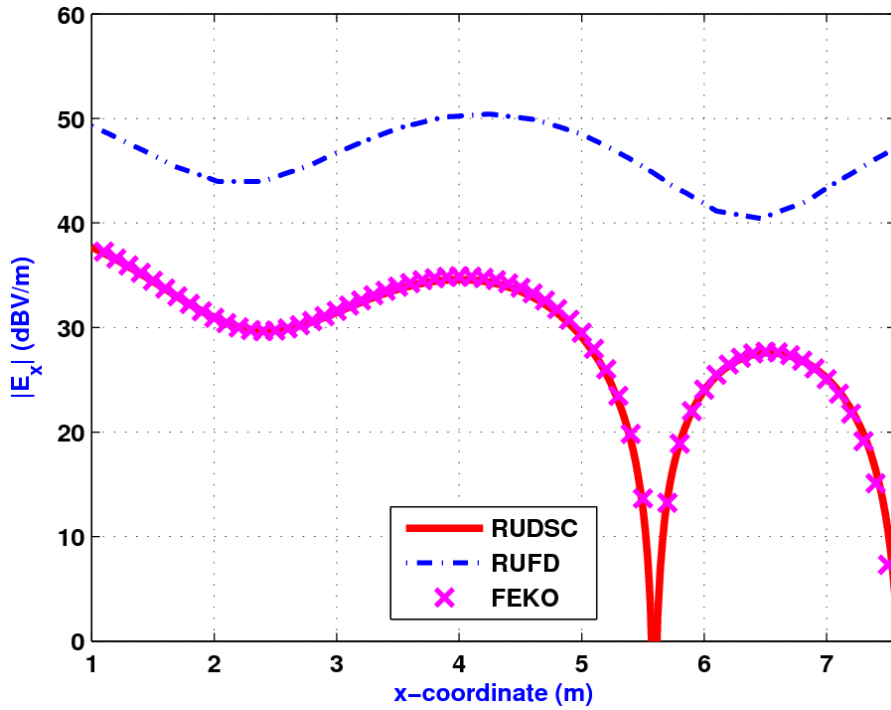
(b) $|E_x|$ in a conducting cavity excited by a current point source.

Figure 5.6: Validation of the RUDSC method.
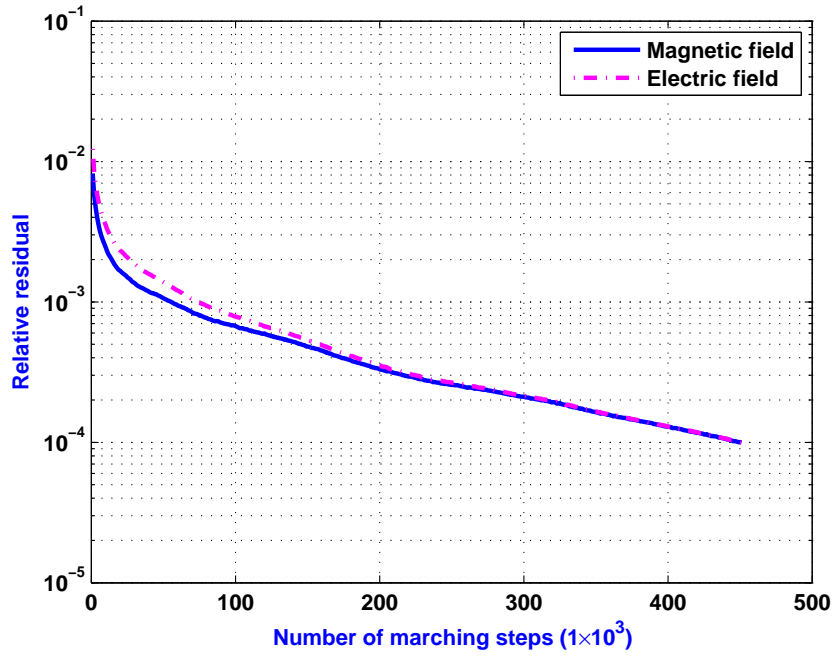
(a) The RUDSC method.
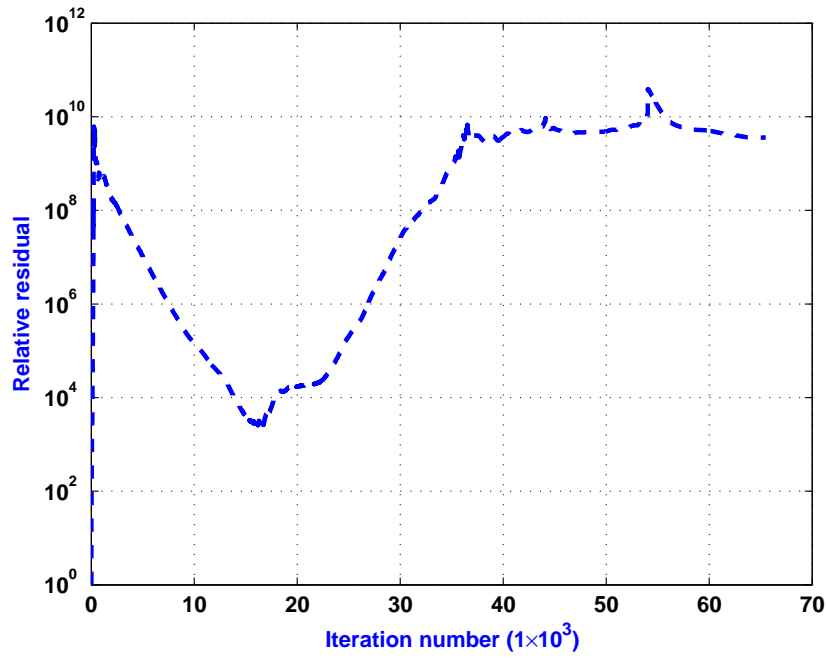
(b) Biconjugate gradient iterative solver.

Figure 5.7: Convergence behaviors of the RUDSC method and the biconjugate gradient iterative solver in modeling a conducting cavity.

Table 5.2: Time and Memory Cost Comparisons for One Stirrer Position and One Frequency Point

Method	Grid size (m)[*]	Number of un-knowns	CPU time (seconds)	Peak memory (GB)
Hybrid RUDSC-MoM	d_x=0.7727, d_y=0.7353 d_z=0.75, l_{max}=0.3659	3915	887	0.03
Hybrid DSC-MoM	The same as those shown in the row above	3915	183	0.66
FEKO	l_{max}=0.3659	16424	2130.97	2.019

[*] l_{max} denotes the maximum length of triangle edge in the MoM.

Lastly, the RUDSC method is used to model the same cavity at the frequency of 200 MHz. At this frequency, the cavity is more than eight-wavelength long, and the number of unknowns is 0.133482 million. Table 5.1 summarizes the computational resources required by the RUDSC method. Figure 5.7 presents the convergence behaviors of the RUDSC method and the biconjugate gradient iterative solver. It is seen that the memory usage of the RUDSC method is very low, even though the number of unknowns is very large. More importantly, the RUDSC method avoids the convergence problem encountered by conventional iterative solvers like the biconjugate gradient iterative solver.

5.3.2 Validation of Hybrid RUDSC-MoM Method

An RC with a single-plate stirrer is considered in order to validate the hybrid RUDSC-MoM method. It has the same geometry and dimension as the one considered in Section 4.3.1. The excitation frequency is 82 MHz, and the excitation and observation points are the same as those used in Section 4.3.1.
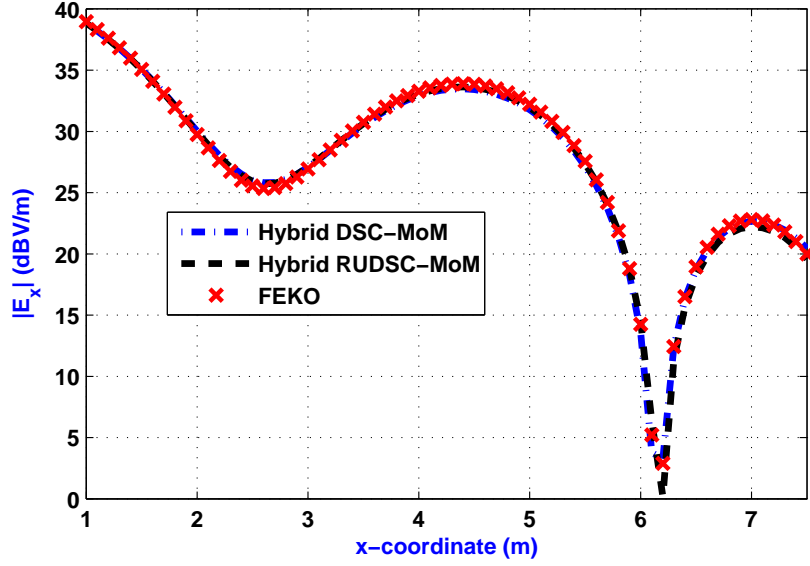
Figure 5.8: $|E_x|$ along a straight in the RC with a single-page stirrer.

Figures 5.8 to 5.10 illustrate the magnitudes of E_x, E_y, and E_z obtained using three different approaches. Good agreement is observed between results from different methods, which validates the hybrid RUDSC-MoM method. Table 5.2 presents the computational resources required by three different methods in modeling the RC with a single-plate stirrer. Simulations in this subsection are conducted on a personal computer with a 2.67 GHz CPU and a 3.25 GB RAM. Although the hybrid RUDSC-MoM requires more CPU time compared to the hybrid DSC-MoM, it is faster than the commercial software. More importantly, the hybrid RUDSC-MoM requires much less memory compared to the other two methods. Therefore, the hybrid RUDSC-MoM method can extend RC modeling to higher frequencies.

5.3.3 Performance Study

After the code validation, the complexity of the proposed hybrid method is studied in detail. The computational and storing requirement of the layer-based algorithm is
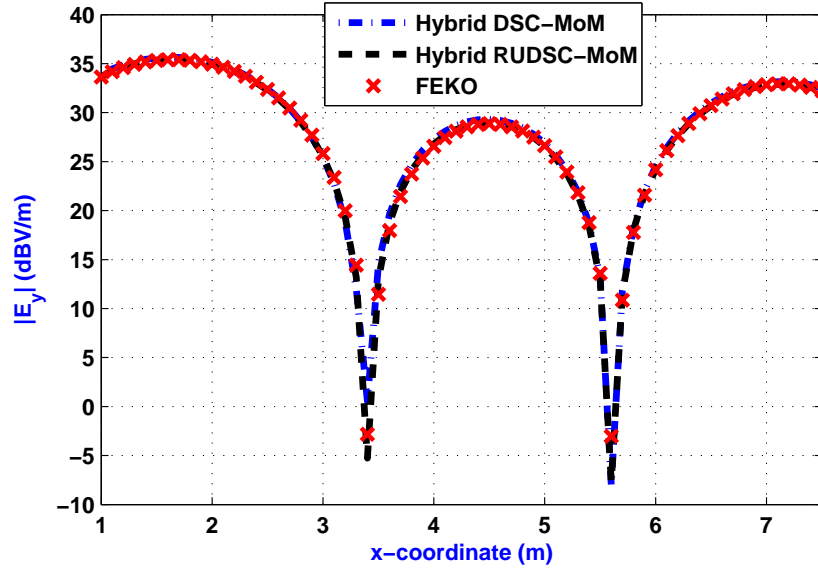
Figure 5.9: $|E_y|$ along a straight in the RC with a single-page stirrer.
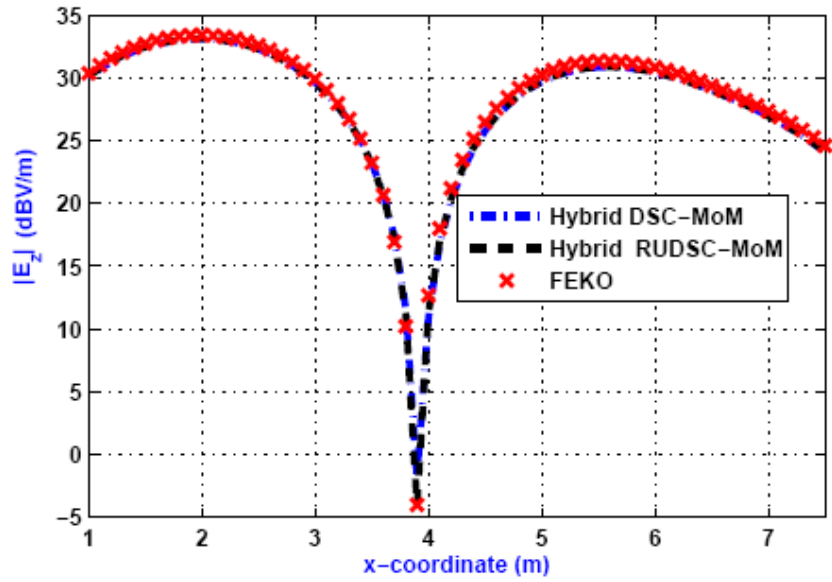
Figure 5.10: $|E_z|$ along a straight in the RC with a single-page stirrer.
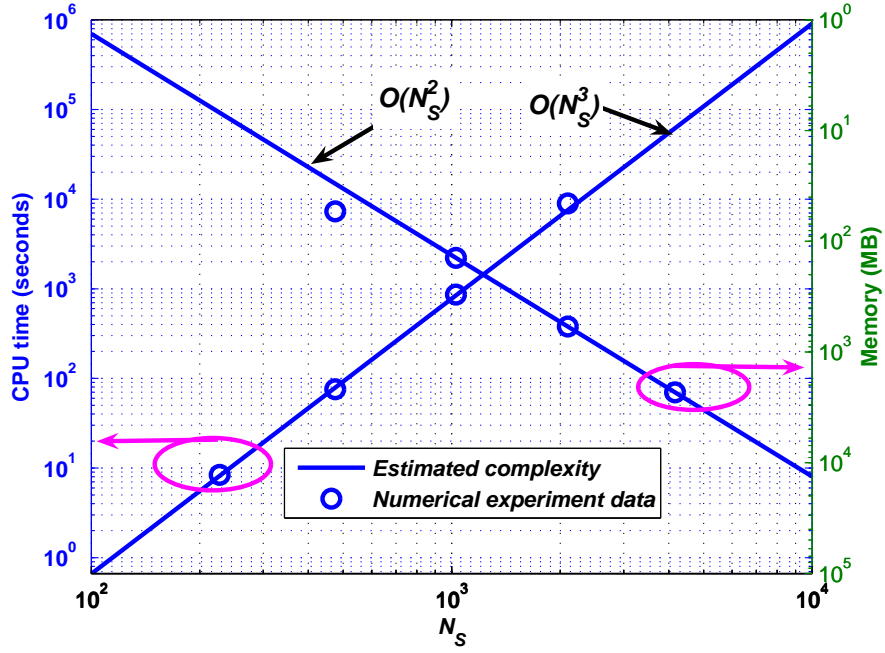
Figure 5.11: Computational and storing complexity of the proposed layer-based elimination algorithm against N_S for elimination of unknowns in one layer ($N_{MoM} = 173$).

first investigated. Figure 5.11 presents the complexity of the layer-based algorithm against N_S. It is seen that the computation and storage complexity for eliminating unknowns in one layer is $O(N_S^3)$ and $O(N_S^2)$, respectively, which agrees with the analysis in Section 5.2.4. Figure 5.12 illustrates the CPU time required by the layer-based elimination algorithm against N_L, which indicates that the CPU time is linearly dependent on N_L.

Figures 5.13 and 5.14 present the storage and computation complexity of the layer-based elimination algorithm against N_{MoM}. These two figures show that the algorithm complexity against N_{MoM} is $O(N_{MoM}^\alpha)$, where the value of α is dependent on the ratio between $(M+1)N_S$ and N_{MoM}. When $(M+1)N_S/N_{MoM}$ is smaller than one, α is close to two; otherwise it is smaller than one. This phenomenon can be explained using the complexity analysis in Section 5.2.4. It is known that the computational and stor-
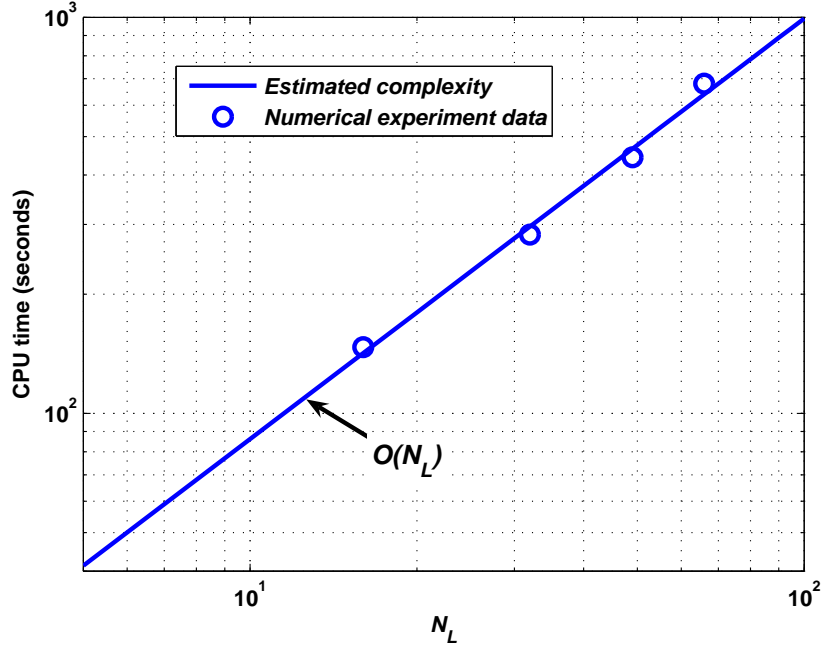
Figure 5.12: Computational complexity of the proposed layer-based elimination algorithm against N_L (N_S=227 and N_{MoM}=173).
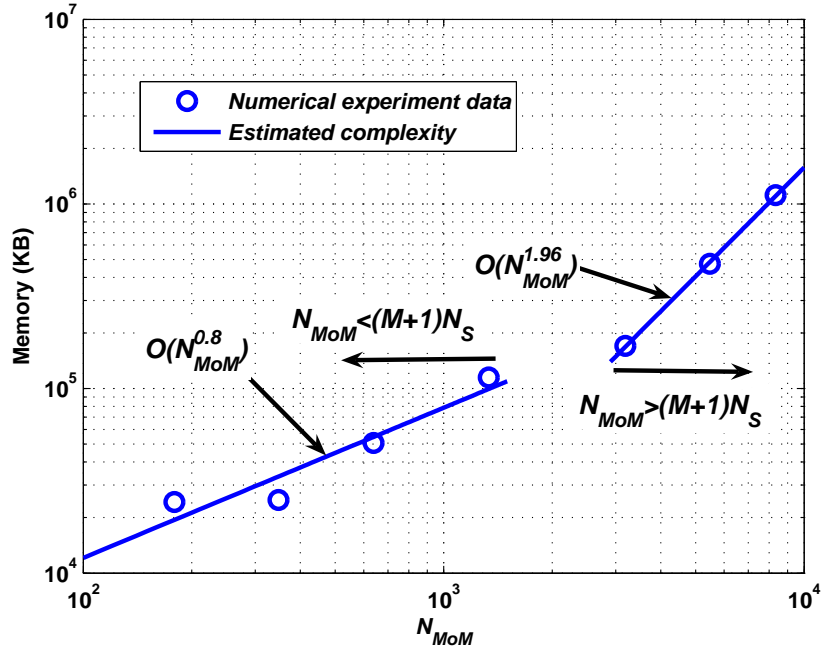
Figure 5.13: Storage requirement of the proposed layer-based elimination algorithm against N_{MoM} for elimination of unknowns in one layer ($N_S = 227$).
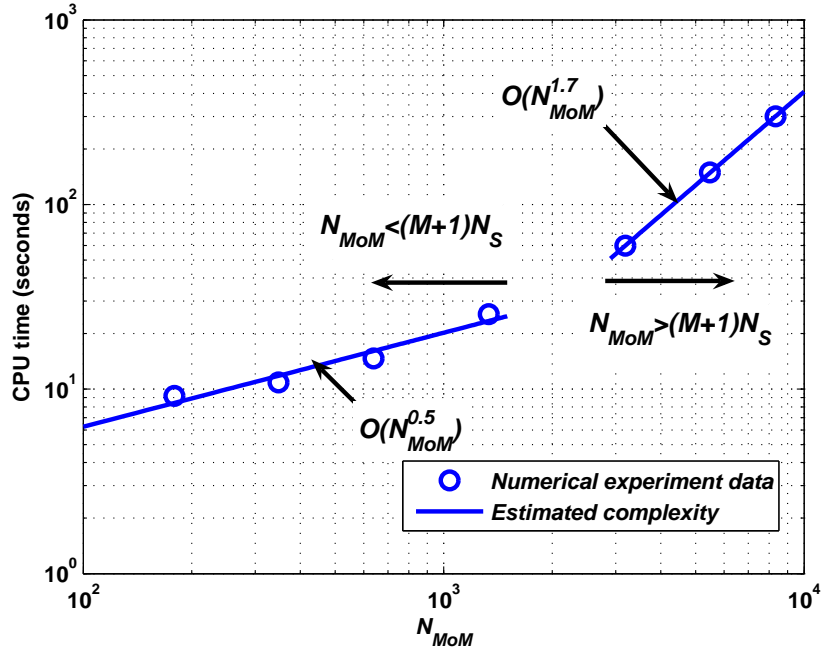
Figure 5.14: Computational requirement of the proposed layer-based elimination algorithm against N_{MoM} for elimination of unknowns in one layer ($N_S = 227$).

ing complexity of the layer-based elimination algorithm is $O\left[(MN_S + N_S + N_{MoM})^2\right]$ and $O\left[N_S^3 + N_S^2(MN_S + N_{MoM}) + N_S(MN_S + N_{MoM})^2\right]$, respectively. When N_{MoM} is smaller than $(M+1)N_S$, the CPU time and memory cost is less sensitive to the value of N_{MoM} and the value of α is smaller. If N_{MoM} is larger than $(M+1)N_S$, the value of N_{MoM} will dominate the CPU time and memory cost, and the value of α is close to 2.

The complexity of RUDSC method is illustrated in Figure 5.15. As expected, both CPU time and memory cost are linearly dependent on N_{DSC} in the RUDSC method. Meanwhile, it can be observed that the memory requirement of RUDSC method is very low compared to the layer-based elimination algorithm. Hence, the memory requirement of the layer-based elimination algorithm can be considered as the memory requirement of the hybrid RUDSC-MoM method.

108
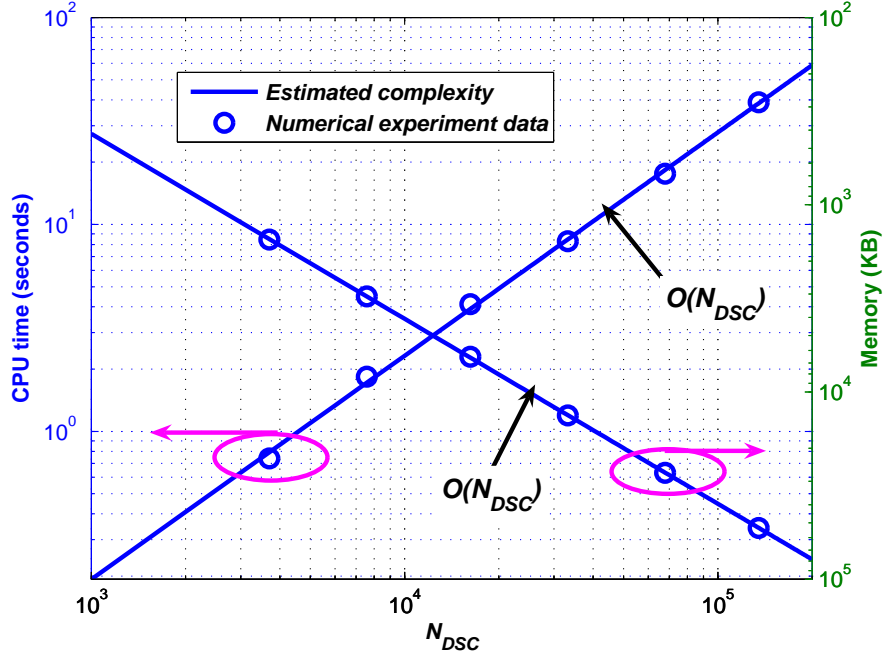
Figure 5.15: Computational and storing complexity of the RUDSC method. The CPU time is for RU of 1000 steps.

In summary, the numerically estimated complexity agrees well with the algorithm analysis in Section 5.2.4. The storage requirement of the proposed method is only quadratically dependent on N_S and N_{MoM}, and it is independent of N_L. It should be noted that O_N^z also affects the complexity of the proposed method. Since O_N^z can be fixed in practice, its effect is therefore not studied here.

5.3.4   An RC with a Five-Paddle Stirrer

Finally, the hybrid RUDSC-MoM is applied for the modeling of an RC with a five-paddle stirrer, which is also simulated in Section 4.3.2. Figures 5.16 and 5.17 illustrate the distribution of $|E_z|$ inside the RC at 82 MHz and 200 MHz, respectively. The excitation is the same as the one used in Section 4.3.2. The field is observed along a straight line connecting points (1 m, 3 m, 10.5 m) and (7.5 m, 3 m, 10.5 m). The
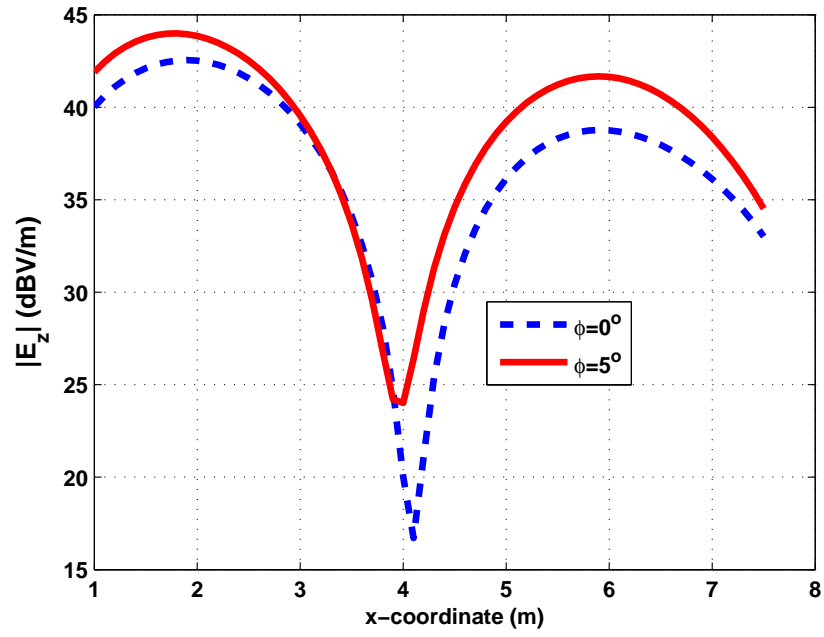
Figure 5.16: Field distribution in the RC with a five-paddle stirrer at 82 MHz.
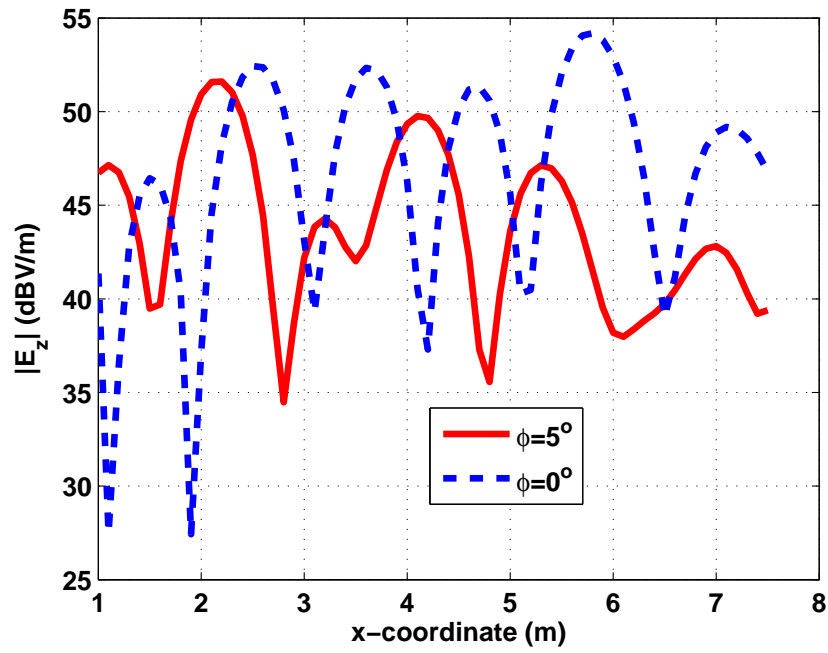
Figure 5.17: Field distribution in the RC with a five-paddle stirrer at 200 MHz.
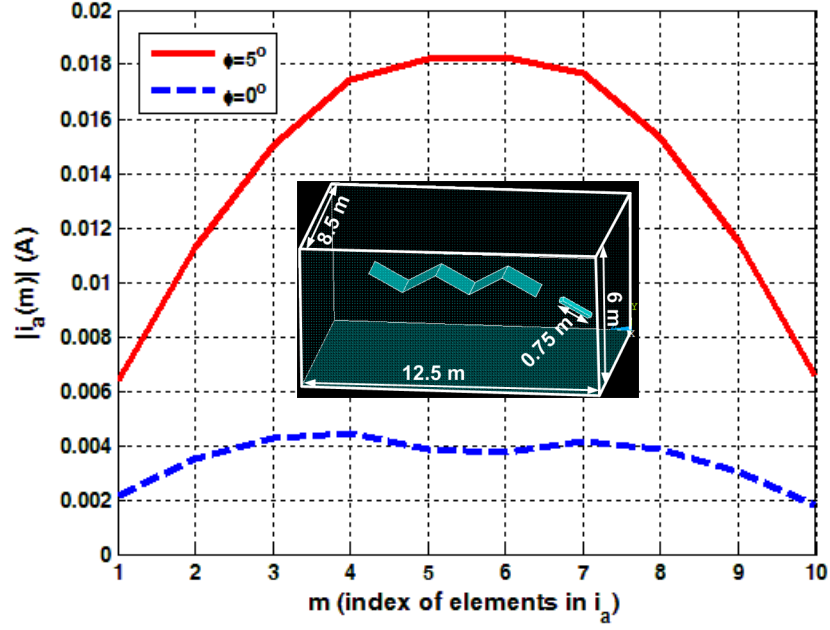
Figure 5.18: Current distribution along a dipole in the RC with a five-paddle stirrer at 200 MHz. The center of the dipole is at (2 m, 1.6 m, 2 m), and it is aligned in the direction (1, 1, 1).

rotation angle ϕ is the angle by which the stirrer is rotated. Field distribution at two stirrer positions ($\phi = 0°$ and $\phi = 5°$) is illustrated in Figures 5.16 and 5.17. At the frequency of 200 MHz, the distribution of $|E_z|$ changes significantly when the stirrer is rotated by 5°. On the other hand, distribution of $|E_z|$ does not change much at the frequency of 82 MHz. This is expected because the field distribution is more sensitive to the geometrical variation at higher frequency.

A dipole antenna is then used to excite the same RC. As the stirrer is rotated, the variation of current distribution along the dipole antenna is studied. The dipole is 0.75 m long, and it is aligned along the direction (1,1,1), as shown in the inset of Figure 5.18. A voltage source is used to excite the dipole antenna at its center. Figure 5.18 presents the current distribution along the dipole antenna at two different stirrer

positions. It is seen that the current distribution changes a lot due to the rotation of the stirrer. This indicates that the reflection coefficient of the dipole antenna may be different due to the rotation of the stirrer. The same phenomenon has been observed in measurements [113].

In modeling the RC at 200 MHz, 42,437 unknowns are used for the cavity, and 1,749 unknowns are utilized for the stirrer. The dipole antenna is discretized into 11 segments. The memory cost for modeling the RC excited by a current point source is 2.12 GB, and the CPU time for one stirrer position is 17.5 hours. The CPU time and memory cost is 2.46 GB and 18 hours for modeling one stirrer position of the RC excited by a dipole antenna. If a pure MoM is used, the number of unknowns is estimated to be 139,350, and more than 144 GB memory would be needed to store the interaction matrix. Solving the matrix equation with a direct solver may double the memory cost, which is far beyond the capacity of a modern personal computer.

5.4 Concluding Remarks

This chapter has described a hybrid technique combining the RUDSC method and MoM for memory-efficient modeling of RCs. The hybrid DSC-MoM method has first been extended to model the transmitting antenna of an RC. The RUDSC method has been proposed for efficient modeling of a cavity. A layer-based elimination algorithm has been developed to eliminate the DSC unknowns with low memory cost. The MoM unknowns have then been solved using a direct solver, and the RC is finally equivalent to a cavity excited by known current sources, which is efficiently modeled using the RUDSC method.

Efficiency of the proposed method has been compared with alternative methods.

It has been shown that the hybrid RUDSC-MoM consumes much less memory and achieves faster speed than a pure MoM-based commercial software. The complexity of the proposed method has been analyzed, and numerical simulations have been conducted to study its CPU time and memory requirement. Numerically estimated complexity result agrees well with the one from algorithm analysis. It has been shown that the memory requirement of the proposed method is independent of the RC's depth. The hybrid RUDSC-MoM substantially reduces memory requirement of RC modeling, which extends the frequency range of RC analysis to what is impossible with a pure MoM-based commercial software. The proposed method has also taken the transmitting antenna into consideration, and it has been used to study the variation of current distribution along a dipole antenna at different stirrer positions. It has been found that the current distribution along the dipole antenna is greatly affected by a rotating stirrer, which will in turn influence the reflection coefficient of the dipole antenna.

Chapter 6

Conclusions and Recommendations

6.1 Conclusions

In this thesis, a thorough literature review on RC modeling has first been conducted in Chapter 2. It has been found that a lot of efforts have been made towards the development of efficient RC modeling techniques. Nevertheless, existing RC modeling techniques are not efficient or flexible enough to provide fast analysis of a full-scale RC. This is mainly because of the resonance nature of an RC, which leads to slow convergence problem when using iterative solvers. Meanwhile, most existing RC modeling methods utilize a single numerical method, and they have their respective strengthes and weaknesses in RC modeling. In order to accelerate the analysis of RC, hybrid technique has been proposed as the strategy to combine advantages of different methods and to overcome their weaknesses.

Recent advances in CEM have then been reviewed, which allows us to combine the strengthes of the state-of-the-art techniques. The MLFMA and HIE methods are found to be inapplicable to RC modeling due to the resonance nature of the RC. On the other hand, the DSC method, a generalized higher-order FD method, is

highly efficient in modeling the cavity of an RC. Nevertheless, the DSC method is not flexible in modeling the stirrers and antennas of an RC because of its structured grids. Furthermore, the RU method is found to be very useful for solving differential equations when conventional iterative solvers encounter slow convergence problem.

Considering the flexibility of MoM and the efficiency of the DSC method, hybridization of the DSC method and MoM has been developed in Chapter 3 for efficient RC analysis. The 2-D TM case is first considered for its simplicity. The hybrid method models the RC in two steps. In the first step, an EFIE is used to enforce the boundary condition along the surface of the stirrer, and it is solved using the MoM. In the second step, the stirrer is replaced by a current sheet, and the RC is equivalent to a cavity excited by a original source and the induced current on the stirrer. Fields in the cavity are governed by Maxwell's equations of differential form, which are numerically solved using the DSC method. In order to couple solutions of the two methods, the stirrer is enclosed using a Huygens' box, and the electric field illuminating the stirrer is connected to the field solution in the DSC method using the equivalence principle. In the meanwhile, the regularization technique for singular terms in differential equations is adopted to model arbitrarily distributed current sources in the structured grids of the DSC method.

Numerical simulations on 2-D TM RC have been conducted in order to explore the benefits of the hybrid DSC-MoM method. Advantages of the DSC method over the second order FD method has first been demonstrated. Compared to the FD method, the DSC method requires less number of unknowns and achieves faster analysis of a 2-D TM cavity using less memory. The hybrid method is then applied to calculate the induced current on a small square cylinder in a 2-D TM cavity, which was calculated and reported by Laermans et al. [29]. Results from the proposed hybrid method agree

well with those from alternative methods. The proposed method has also been used to model a 2-D TM RC, and good agreement has been observed between the proposed method and a pure MoM. Efficiency of the hybrid method has been compared against a pure MoM. Taking advantage of the high efficiency of the DSC method, the hybrid DSC-MoM method is shown to be at least six times faster than a pure MoM in modeling a 2-D TM RC. Meanwhile, the memory cost of the proposed method is approximately the same as that of a pure MoM.

After the success of the 2-D hybrid method, a 3-D hybrid DSC-MoM method has been developed in Chapter 4 in order to accelerate the analysis of 3-D RCs. Similar to the 2-D case, the 3-D hybrid method models the cavity and stirrer using the DSC method and MoM, respectively. In the 3-D hybrid method, surfaces of the stirrer and Huygens' box are discretized into a set of planar triangles. The induced current on the stirrer and the equivalent current along the Huygens' box are expanded using the RWG basis. The property of RWG basis is utilized to connect the DSC field solution with the expansion coefficients of the equivalent current, and the 3-D regularization technique is adopted to model arbitrarily distributed current sources in DSC's structured grids.

Using an RC with a single-plate stirrer, the 3-D hybrid method has been validated against a pure MoM-based commercial software. It has been observed that results from the proposed method agree well with those from the commercial software. Performance comparison has also been made between the proposed method and the commercial software. The proposed hybrid method has been shown to be more than ten times faster than the commercial software, and its memory consumption is only one third of that by the commercial software. The hybrid method has also been used to study the stirring effectiveness of three stirrers. It has been found that the width of the stirrer should be large enough to make the stirrer effective. Furthermore, irregularity of the

stirrer is helpful in enhancing the stirring effectiveness.

Despite its improved efficiency, the memory requirement of hybrid DSC-MoM method is still high, which limits the frequency range of RC modeling. In order to reduce the memory consumption and to extend the frequency range of RC modeling, a hybrid RUDSC-MoM method has been developed in Chapter 5. The assumption that a point current source is adopted as the excitation in Chapter 4 is eliminated by taking a practical transmitting antenna into consideration. The MoM for 3-D wire structures is incorporated into the hybrid RUDSC-MoM method. In the hybrid RUDSC-MoM method, a layer-based elimination algorithm is used to eliminate the MoM unknowns, and a direct solver can then be adopted to solve the MoM unknowns because the number of MoM unknowns is usually not large. The RUDSC method is then applied to obtain the solution to the DSC unknowns. The algorithm complexity of the hybrid RUDSC-MoM method has also been analyzed. The storing requirement has been shown to be independent of the cavity's depth.

The hybrid RUDSC-MoM method has been validated through comparison with alternative methods. Its CPU time and memory cost are compared against the hybrid DSC-MoM and a pure MoM-based commercial software. Numerical simulations have showed that the hybrid RUDSC-MoM method reduces the memory requirement by twenty times and sixty times compared to the hybrid DSC-MoM method and the commercial software, respectively. However, the hybrid RUDSC-MoM method is not as fast as the hybrid DSC-MoM method, but it is two times faster than the commercial software. Numerical experiments have been conducted to study the computational and storing complexity of the hybrid RUDSC-MoM method, and numerically estimated complexity result agrees well with the theoretical analysis. The hybrid RUDSC-MoM method substantially reduces the memory requirement of RC modeling, and it extends

RC modeling to higher frequencies.

In summary, the hybrid DSC-MoM method developed in Chapters 3 and 4 greatly accelerates the RC analysis, and the hybrid RUDSC-MoM method presented in Chapter 5 substantially reduces the memory requirement of RC analysis. Both methods are more efficient compared to a commercial software. The former can be used for fast analysis of RCs at low frequencies, and the latter should be adopted for RC modeling at higher frequencies.

6.2 Recommendations for Further Research

The hybrid RUDSC-MoM can be further improved in the following aspects. First, because of the local property of curl operators in Maxwell's equations, the RU method is naturally parallel. Hence, parallel computing can be easily used to accelerate the RU method. Second, since the hybrid RUDSC-MoM requires low memory, the graphics processing unit (GPU) can be used to reduce the computational burden. Third, if the memory usage of the hybrid RUDSC-MoM is beyond the capability of a GPU, CPU and GPU can be used simultaneously to conduct the computation. Most data will be stored in the main memory, and data required by GPU are stored in the video memory. In this way, one can utilize both the fast speed of GPU and the large memory of CPU.

Meanwhile, for wide-band analysis, time-domain methods are desired because wide-band information can be obtained using a single simulation. Hence, it is meaningful to extend the proposed hybrid technique to time-domain. The main challenge of developing time-domain hybridization of the DSC method and MoM is the stability, because the time-domain integral equation (TDIE) suffers from the late time

instability when marching on in time (MOT) method is used [114]. The MOT method adopts sub-sectional basis to describe temporal behavior of a signal. It leads to explicit marching scheme and does not need to solve matrix equation, which makes the MOT method efficient. However, when the signal decays very slowly, the MOT method needs a large number of marching steps and the TDIE becomes instable. Though there are many invariants of TDIE with improved stability [115–117], these methods usually need much more computational effort. The averaging technique introduces the least extra computational cost. However, it was found that the averaging technique postponed instead of eliminating the late time instability [118]. The marching on in degree (MOD) method eliminates the late time instability [119, 120]. It utilizes global time-domain basis functions which decay to zero as time goes to infinity. This ensures the stability of the time-domain solution. Nevertheless, it requires solving matrix equation, which incurs heavy computational load in modeling the cavity of an RC [121]. In this case, one can use MOD and MOT for integral equation and differential equation, respectively. The hybridization of MOD and MOT may overcome the late time instability of TDIE and retain low computational load in modeling the cavity. Another possible way is to hybridize time-domain DSC (TDDSC) with frequency-domain MoM, which is similar to the hybrid FDTD-MoM [122]. In both hybrid MOD-MOT and hybrid TDDSC-MoM methods, iterations are required and convergence needs careful investigation.

Finally, there is usually a platform to support the EUT in practical RC measurements. In many cases, the platform is a wooden table, which greatly influences the field distribution in an RC [23]. Meanwhile, the chamber may be loaded in practice. Both the platform and the lossy loading are inhomogeneous media inside the cavity, and the hierarchical implicit derivative matching method [123] can be used together with the DSC method to deal with such inhomogeneous media. In order to make sim-

ulation comparable with measurement, the effect of the platform and loading should be taken into account, which may also be an important topic of further research.

Appendix A

Definition of Differentiation Matrices

This Appendix first takes the example of differentiation matrix $\mathbf{A_x}$ in (3.14a) to describe how the differentiation matrix is calculated. Explicit expression of all other differentiation matrices is then presented. Since the differentiation matrix is sparse, only non-zero elements are defined.

A.1 2-D TM Case

Take matrix $\mathbf{A_x}$ as an example to illustrate how to fill differentiation matrix. $\mathbf{A_x}$ arises from the differential operator $\frac{\partial E_z}{\partial y}$ calculated at the position of H_x. Figure A.1 shows Yee's grid of E_z and H_x for a 2-D TM cavity. Grid points of H_x are indexed using i_{h_x} and j_{h_x} along x- and y-directions, respectively, where $i_{h_x} \in [1, N_x^{H_x}]$ and $j_{h_x} \in [1, N_y^{H_x}]$. $N_x^{H_x}$ and $N_y^{H_x}$ denote the number of H_x grid points along x- and y-directions, respectively. Grid points of E_z are indexed using i_z and j_z along x- and y-directions, respectively, where $i_z \in [1, N_x^{E_z}]$ and $j_z \in [1, N_y^{E_z}]$. $N_x^{E_z}$ and $N_y^{E_z}$ represent the number of E_z grid points in x- and y-directions, respectively. E_z is first
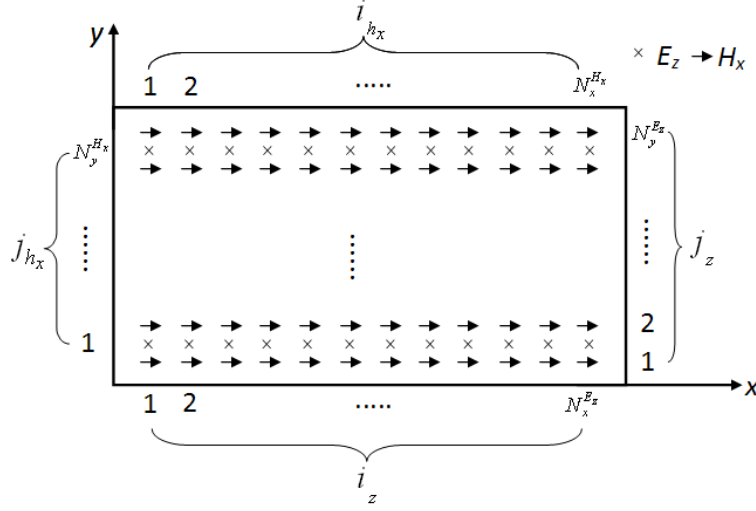
Figure A.1: Yee's Grid for E_z and H_x. Four edges of the rectangle are conducting walls of a cavity. $N_\xi^{H_x}$ and $N_\xi^{E_z}$ denote the number of H_x and E_z grid points along ξ-direction. i_z and j_z are global index of E_z grid points along x- and y-directions, respectively. i_{h_x} and j_{h_x} denote global index of H_x grid points in x- and y-directions.

expanded using the regularized Lagrange interpolation basis. $\frac{\partial E_z}{\partial y}$ is calculated at a H_x grid point. From Figure A.1, one can see that only $L_{M,j}(y)$ is needed to expand E_z at a H_x grid point, i.e.

$$E_z \mid_{i_{h_x}, j_{h_x}} = \sum_{j=-M+1}^{M} L_{M,j}(y_{0.5}) E_z^{i_{h_x}, j_{h_x}-1+j}, \qquad (A.1)$$

where $\mid_{i_{h_x}, j_{h_x}}$ means the value of E_z is calculated at H_x grid point (i_{h_x}, j_{h_x}), and j is the local index of E_z grid points, as illustrated in Figure A.2. $L_{M,j}(y_{0.5})$ means the regularized Lagrange interpolation basis is calculated at a point $0.5h_y$ away from two grid points, as shown in Figure A.2. Hence,

$$\frac{\partial E_z}{\partial y} \mid_{i_{h_x}, j_{h_x}} = \sum_{j=-M+1}^{M} L'_{M,j}(y_{0.5}) E_z^{i_{h_x}, j_{h_x}-1+j}. \qquad (A.2)$$

(A.2) is valid if $(j_{h_x} - 1 + j) \in (0, N_y^{E_z}]$. Therefore, if $(j_{h_x} - 1 + j) \in (0, N_y^{E_z}]$, $A_x(m, n) = L'_{M,j}(y_{0.5})$, where $m = i_{h_x} + (j_{h_x} - 1) N_x^{H_x}$, $n = i_{h_x} + (j' - 1) N_x^{E_z}$, and

122

local index of grid points

$-3 \quad -2 \quad -1 \quad 0 \quad y' \quad 1 \quad 2 \quad 3 \quad 4$

$-\dfrac{7h_y}{2} \quad -\dfrac{5h_y}{2} \quad -\dfrac{3h_y}{2} \quad -\dfrac{h_y}{2} \quad 0 \quad \dfrac{h_y}{2} \quad \dfrac{3h_y}{2} \quad \dfrac{5h_y}{2} \quad \dfrac{7h_y}{2}$

local coordinate
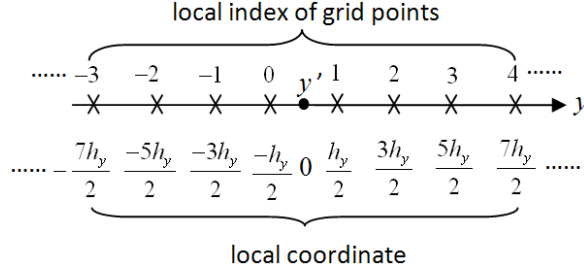
Figure A.2: Point y' is $0.5h_y$ away from two neighboring grid points. h_y is the grid size in y-direction.
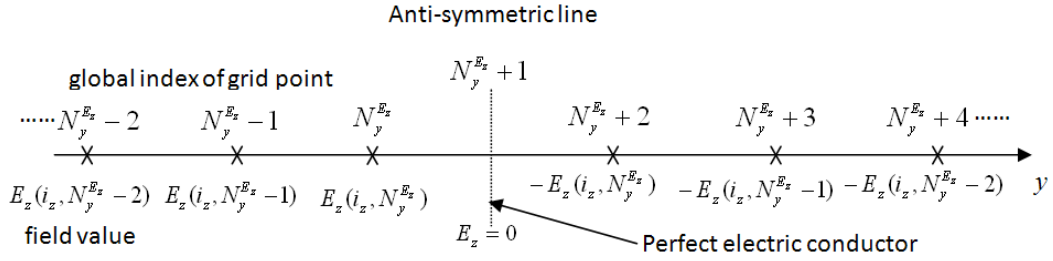
Figure A.3: Anti-symmetric extension of E_z near a perfect electric conductor.

$j' = j_{h_x} - 1 + j$. When $(j_{h_x} - 1 + j)$ is 0 or $N_y^{E_z}+1$, the value of $E_z^{i_{h_x}, j_{h_x}-1+j}$ is 0, and it will not contribute to the summation in (A.2). If $(j_{h_x} - 1 + j) > N_y^{E_z} + 1$, anti-symmetric extension can be used to calculate the summation in (A.2). Figure A.3 shows how anti-symmetric extension relates E_z beyond $N_y^{E_z}$ (on the right of the perfect electric conductor) to E_z within $N_y^{E_z}$ (on the left of the perfect electric conductor). The theoretical basis of anti-symmetric extension is image theory. Similarly, one can use anti-symmetric extension to calculate (A.2) if $(j_{h_x} - 1 + j) < 0$. With the anti-symmetric extension and from the summation in (A.2), one can have $A_x(m, n) = A_x(m, n) - L'_{M,j}(y_{0.5})$, where $m = i_{h_x} + (j_{h_x} - 1) N_x^{H_x}$, $n = i_{h_x} + (j' - 1) N_L^{E_z}$. j' equals $1 - j_{h_x} - j$ and $2N_y^{E_z} - (j_{h_x} - 3 + j)$ for the case of $(j_{h_x} - 1 + j) < 0$ and $(j_{h_x} - 1 + j) > N_y^{E_z} + 1$, respectively. In summary,

$$
A_x(m, n) = \begin{bmatrix} L'_{M,j}(y_{0.5}) & \text{if } (j_{h_x} - 1 + j) \in (0, N_y^{E_z}] \\ A_x(m, n) - L'_{M,j}(y_{0.5}) & \text{if } (j_{h_x} - 1 + j) \notin [0, N_y^{E_z} + 1] \end{bmatrix}, \quad \text{(A.3)}
$$

123
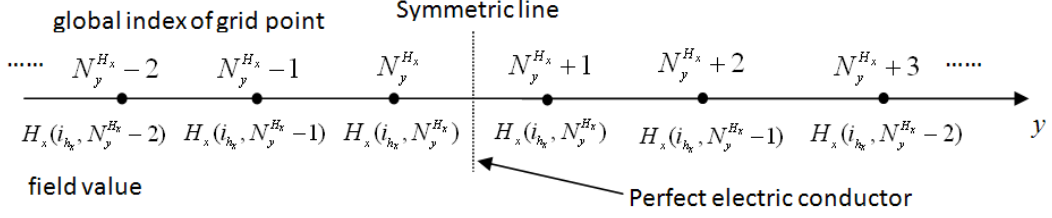
Figure A.4: Symmetric extension of H_x near a perfect electric conductor.

where $m = i_{h_x} + (j_{h_x} - 1) N_x^{H_x}$, $n = i_{h_x} + (j' - 1) N_x^{E_z}$, $-M + 1 \leq j \leq M$ and

$$
j' = \begin{bmatrix} 1 - j_{h_x} - j & \text{if } (j_{h_x} - 1 + j) < 0 \\ 2N_y^{E_z} - (j_{h_x} - 3 + j) & \text{if } (j_{h_x} - 1 + j) > N_y^{E_z} + 1 \\ j_{h_x} - 1 + j & \text{if } (j_{h_x} - 1 + j) \in (0, N_y^{E_z}] \end{bmatrix} .
$$

If uniform grid is used, $L'_{M,j}(y_{0.5}) \, (-M + 1 \leq j \leq M)$ only needs calculating once using the grid configuration in Figure A.2.

Matrices $\mathbf{A_y}$, $\mathbf{B_x}$ and $\mathbf{B_y}$ can be filled following the way described in the first paragraph of this section. It should be mentioned that when the global index in ξ-direction is abnormal for tangential magnetic field (i.e. less than one or larger than the number of grid points in ξ-direction), symmetric extension is used to recalculate the global index. Figure A.4 shows how symmetric extension works in the case of H_x. Symmetric extension is also based on the image theory. Since the derivation of expression for matrices $\mathbf{A_y}$, $\mathbf{B_x}$ and $\mathbf{B_y}$ is similar to that for matrix $\mathbf{A_x}$, only final expression of these matrices are given and the detailed derivation is omitted.

Equations (A.4) to (A.6) present the expression of differentiation matrices $\mathbf{A_y}$, $\mathbf{B_x}$ and $\mathbf{B_y}$. In these equations, the subscript '0.5' means L' is calculated at a point which is $0.5h_\xi$ away from two neighboring grid points. i and j are local indexes of grid

points, and they range from $-M + 1$ to M. $N_x^{H_y}$ is the number of H_y grid points in x-direction. i_{h_y} and j_{h_y} are global indexes of H_y in x- and y-directions, respectively.

$$
A_y(m, n) = \left[\begin{array}{ll} L'_{M,i}(x_{0.5}) & \text{if } \left(i_{h_y} - 1 + i\right) \in (0, N_x^{E_z}] \\ A_y(m, n) = A_y(m, n) - L'_{M,i}(x_{0.5}) & \text{if } \left(i_{h_y} - 1 + i\right) \notin [0, N_x^{E_z} + 1] \end{array} \right],
$$

(A.4)

where $m = i_{h_y} + \left(j_{h_y} - 1\right) N_x^{H_y}$, $n = i' + \left(j_{h_y} - 1\right) N_x^{E_z}$, and

$$
i' = \left[\begin{array}{ll} 1 - i_{h_y} - i & \text{if } \left(i_{h_y} - 1 + i\right) < 0 \\ 2N_x^{E_z} - \left(i_{h_y} - 3 + i\right) & \text{if } \left(i_{h_y} - 1 + i\right) > N_x^{E_z} + 1 \\ i_{h_y} - 1 + i & \text{if } \left(i_{h_y} - 1 + i\right) \in (0, N_x^{E_z}] \end{array} \right].
$$

$$
B_x(m, n) = \left[\begin{array}{ll} -L'_{M,j}(y_{0.5}) & \text{if } (j_z + j) \in (0, N_y^{H_x}] \\ B_x(m, n) - L'_{M,j}(y_{0.5}) & \text{otherwise} \end{array} \right],
$$

(A.5)

where $m = i_z + (j_z - 1) N_x^{E_z}$, $n = i_z + (j' - 1) N_x^{H_x}$, and

$$
j' = \left[\begin{array}{ll} 1 - j_z - j & \text{if } (j_z + j) \leq 0 \\ 2N_y^{H_x} - (j_z - 1 + j) & \text{if } (j_z + j) \geq N_y^{H_x} + 1 \\ j_z + j & \text{if } (j_z + j) \in (0, N_y^{H_x}] \end{array} \right].
$$

$$
B_y(m, n) = \left[\begin{array}{ll} L'_{M,i}(x_{0.5}) & \text{if } (i_z + i) \in (0, N_x^{H_y}] \\ B_y(m, n) + L'_{M,i}(x_{0.5}) & \text{otherwise} \end{array} \right],
$$

(A.6)

where $m = i_z + (j_z - 1) N_x^{E_z}$, $n = i' + (j_z - 1) N_x^{H_y}$, and

$$
i' = \begin{bmatrix} 1 - i_z - i & \text{if } (i_z + i) \leq 0 \\ 2N_x^{H_y} - (i_z - 1 + i) & \text{if } (i_z + i) \geq N_x^{H_y} + 1 \\ i_z + i & \text{if } (i_z + i) \in (0, N_x^{H_y}] \end{bmatrix}.
$$

A.2 Matrix D in Equation (4.14)

The scalar form of $\nabla \times \nabla \times \vec{E}_{DSC}$ in (4.11) is

$$
\begin{bmatrix} -\frac{\partial^2}{\partial y^2} - \frac{\partial^2}{\partial z^2} & \frac{\partial^2}{\partial x \partial y} & \frac{\partial^2}{\partial x \partial z} \\ \frac{\partial^2}{\partial x \partial y} & -\frac{\partial^2}{\partial x^2} - \frac{\partial^2}{\partial z^2} & \frac{\partial^2}{\partial y \partial z} \\ \frac{\partial^2}{\partial x \partial z} & \frac{\partial^2}{\partial y \partial z} & -\frac{\partial^2}{\partial x^2} - \frac{\partial^2}{\partial y^2} \end{bmatrix} \begin{bmatrix} E_{DSC}^x(\vec{r}) \\ E_{DSC}^y(\vec{r}) \\ E_{DSC}^z(\vec{r}) \end{bmatrix}. \tag{A.7}
$$

Therefore, matrix $\mathbf{D}$ can be written as

$$
\mathbf{D} = \begin{bmatrix} \mathbf{D_{xx}} & \mathbf{D_{xy}} & \mathbf{D_{xz}} \\ \mathbf{D_{yx}} & \mathbf{D_{yy}} & \mathbf{D_{yz}} \\ \mathbf{D_{zx}} & \mathbf{D_{zy}} & \mathbf{D_{zz}} \end{bmatrix}. \tag{A.8}
$$

The nine sub-matrices of matrix $\mathbf{D}$ are defined in Tables A.1 to A.18. In all these tables, i, j, and k denote local index of grid points in x-, y-, and z-directions, and they range from $-M + 1$ to M. Figure A.2 illustrates how the local index is defined. i', j', and k' are global counterpart of i, j, and k, respectively. $N_\xi^{E_\zeta}$ represents the number of E_ζ grid points in ξ-direction. i_ξ, j_ξ, and k_ξ are global index of E_ξ grid points in x-, y-, and z-directions, respectively. $i_\xi \in (0, N_x^{E_\xi}]$, $j_\xi \in (0, N_y^{E_\xi}]$, and $k_\xi \in (0, N_z^{E_\xi}]$. $\xi_{0.5}$ means the function value is calculated at a point $0.5h_\xi$ away from two neighboring

local index of grid points

$$\cdots -3 \quad -2 \quad -1 \quad 0 \, \xi' \quad 1 \quad 2 \quad 3 \quad 4 \cdots$$

$$\cdots -3h_\xi \quad -2h_\xi \quad -h_\xi \quad 0 \quad h_\xi \quad 2h_\xi \quad 3h_\xi \quad 4h_\xi \cdots$$

local coordinate
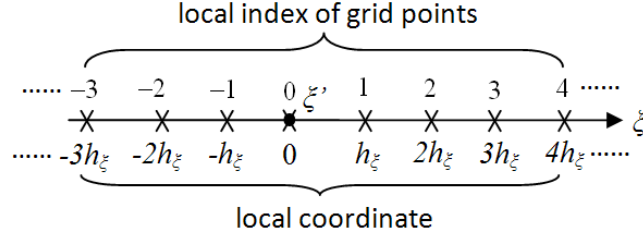
Figure A.5: Point ξ' is a grid point. h_ξ is the grid size in ξ-direction.

Table A.1: Definition of $D_{xx}(m, n)$. $m = i_x + (j_x - 1)N_x^{E_x} + (k_x - 1)N_x^{E_x}N_y^{E_x}$ and $n = i_x + (j' - 1)N_x^{E_x} + (k' - 1)N_x^{E_x}N_y^{E_x}$. j' and k' are defined in Table A.2

$D_{xx}(m, n) = -L''_{M,j}(y_0)$	if $k = 0$, $j \neq 0$ and $(j_x + j) \in (0, N_y^{E_x}]$
$D_{xx}(m, n) = D_{xx}(m, n) + L''_{M,j}(y_0)$	if $k = 0$, $j \neq 0$ and $(j_x + j) \notin [0, N_y^{E_x}+1]$
$D_{xx}(m, n) = -L''_{M,k}(z_0)$	if $j = 0$, $k \neq 0$ and $(k_x + k) \in (0, N_z^{E_x}]$
$D_{xx}(m, n) = D_{xx}(m, n) + L''_{M,k}(z_0)$	if $j = 0$, $k \neq 0$ and $(k_x + k) \notin [0, N_z^{E_x}+1]$
$D_{xx}(m, n) = -L''_{M,j}(y_0) - L''_{M,k}(z_0)$	if $k = 0$ and $j = 0$

grid points, where h_ξ is the grid size in ξ-direction. An example of $y_{0.5}$ is shown in Figure A.2. Meanwhile, ξ_0 means the function value is computed at a grid point, as shown in Figure A.5.

If global index of E_ζ grid points in ξ-direction is less than one or exceeds $N_\xi^{E_\zeta}$, symmetric or anti-symmetric extension can be utilized to recalculate the global index. For normal and tangential electric fields, symmetric and anti-symmetric extension should be used, respectively. Once the nine sub-matrices are assembled using Tables A.1 to A.18, they are put together to obtain matrix $\mathbf{D}$ as shown in (A.8).

Table A.2: Definition of j' and k' for $D_{xx}(m, n)$

Condition for j'	Value of j'	Condition for k'	Value of k'
if $(j_x + j) \in (0, N_y^{E_x}]$	$j_x + j$	if $(k_x + k) \in (0, N_z^{E_x}]$	$k_x + k$
if $(j_x + j) < 0$	$-(j_x + j)$	if $(k_x + k) < 0$	$-(k_x + k)$
if $(j_x + j) > N_y^{E_x} + 1$	$2N_y^{E_x} - j_x - j + 2$	if $(k_x + k) > N_z^{E_x}+1$	$2N_z^{E_x} - k_x - k + 2$

Table A.3: Definition of $D_{xy}(m,n)$. $m = i_x + (j_x - 1)N_x^{E_x} + (k_x - 1)N_x^{E_x}N_y^{E_x}$ and $n = i' + (j' - 1)N_x^{E_y} + (k_x - 1)N_x^{E_y}N_y^{E_y}$. i' and j' are defined in Table A.4

$D_{xy}(m,n) =$ $L'_{M,i}(x_{0.5})\,L'_{M,j}(y_{0.5})$	if $(i_x - 1 + i) \in (0, N_x^{E_y}]$ and $(j_x + j) \in (0, N_y^{E_y}]$
$D_{xy}(m,n) = D_{xy}(m,n) +$ $L'_{M,i}(x_{0.5})L'_{M,j}(y_{0.5})$	if $(i_x - 1 + i) \in (0, N_x^{E_y}]$ and $(j_x + j) \notin (0, N_y^{E_y}]$
$D_{xy}(m,n) = D_{xy}(m,n) -$ $L'_{M,i}(x_{0.5})L'_{M,j}(y_{0.5})$	if $(i_x - 1 + i) < 0$ or $(i_x - 1 + i) > N_x^{E_y} + 1$

Table A.4: Definition of i' and j' for $D_{xy}(m,n)$

Condition for i'	Value of i'	Condition for j'	Value of j'
if $(i_x - 1 + i) \in (0, N_x^{E_y}]$	$i_x + i - 1$	if $(j_x + j) \in (0, N_y^{E_y}]$	$j_x + j$
if $(i_x - 1 + i) < 0$	$1 - i_x - i$	if $(j_x + j) \leq 0$	$1 - j_x - j$
if $(i_x - 1 + i) > N_x^{E_y} + 1$	$2N_x^{E_y} - (i_x + i - 3)$	if $(j_x + j) > N_y^{E_y}$	$2N_y^{E_y} + 1 - j_x - j$

Table A.5: Definition of $D_{xz}(m,n)$. $m = i_x + (j_x - 1)N_x^{E_x} + (k_x - 1)N_x^{E_x}N_y^{E_x}$ and $n = i' + (j_x - 1)N_x^{E_z} + (k' - 1)N_x^{E_z}N_y^{E_z}$. i' and k' are defined in Table A.6

$D_{xz}(m,n) =$ $L'_{M,i}(x_{0.5})\,L'_{M,k}(z_{0.5})$	if $(i_x - 1 + i) \in (0, N_x^{E_z}]$ and $(k_x + k) \in (0, N_z^{E_z}]$
$D_{xz}(m,n) = D_{xz}(m,n) +$ $L'_{M,i}(x_{0.5})L'_{M,k}(z_{0.5})$	if $(i_x - 1 + i) \in (0, N_x^{E_z}]$ and $(k_x + k) \notin (0, N_z^{E_z}]$
$D_{xz}(m,n) = D_{xz}(m,n) -$ $L'_{M,i}(x_{0.5})L'_{M,k}(z_{0.5})$	if $(i_x - 1 + i) < 0$ or $(i_x - 1 + i) > N_x^{E_z} + 1$

Table A.6: Definition of i' and k' for $D_{xz}(m,n)$

Condition for i'	Value of i'	Condition for j'	Value of j'
if $(i_x - 1 + i) \in (0, N_x^{E_z}]$	$i_x + i - 1$	if $(k_x + k) \in (0, N_z^{E_z}]$	$k_x + k$
if $(i_x - 1 + i) < 0$	$1 - i_x - i$	if $(k_x + k) \leq 0$	$1 - k_x - k$
if $(i_x - 1 + i) > N_x^{E_z} + 1$	$2N_x^{E_z} - (i_x + i - 3)$	if $(k_x + k) > N_z^{E_z}$	$2N_z^{E_z} + 1 - k_x - k$

Table A.7: Definition of $D_{yy}(m,n)$. $m = i_y + (j_y - 1)N_x^{E_y} + (k_y - 1)N_x^{E_y}N_y^{E_y}$ and $n = i' + (j_y - 1)N_x^{E_y} + (k' - 1)N_x^{E_y}N_y^{E_y}$. i' and k' are defined in Table A.8

$D_{yy}(m,n) = -L_{M,i}''(x_0)$	if $k = 0$, $i \neq 0$ and $(i_y + i) \in (0, N_x^{E_y}]$
$D_{yy}(m,n) = D_{yy}(m,n) + L_{M,i}''(x_0)$	if $k = 0$, $i \neq 0$ and $(i_y + i) \notin [0, N_x^{E_y} + 1]$
$D_{yy}(m,n) = -L_{M,k}''(z_0)$	if $i = 0$, $k \neq 0$ and $(k_y + k) \in (0, N_z^{E_y}]$
$D_{yy}(m,n) = D_{yy}(m,n) + L_{M,k}''(z_0)$	if $i = 0$, $k \neq 0$ and $(k_y + k) \notin [0, N_z^{E_y} + 1]$
$D_{yy}(m,n) = -L_{M,i}''(x_0) - L_{M,k}''(z_0)$	if $k = 0$ and $i = 0$

Table A.8: Definition of i' and k' for $D_{yy}(m,n)$

Condition for i'	Value of i'	Condition for k'	Value of k'
if $(i_y + i) \in (0, N_x^{E_y}]$	$i_y + i$	if $(k_y + k) \in (0, N_z^{E_y}]$	$k_y + k$
if $(i_y + i) < 0$	$-(i_y + i)$	if $(k_y + k) < 0$	$-(k_y + k)$
if $(i_y + i) > N_x^{E_y} + 1$	$2N_x^{E_y} - i_y - i + 2$	if $(k_y + k) > N_z^{E_y} + 1$	$2N_z^{E_y} - k_y - k + 2$

Table A.9: Definition of $D_{yx}(m,n)$. $m = i_y + (j_y - 1)N_x^{E_y} + (k_y - 1)N_x^{E_y}N_y^{E_y}$ and $n = i' + (j' - 1)N_x^{E_x} + (k_y - 1)N_x^{E_x}N_y^{E_x}$. i' and j' are defined in Table A.10

$D_{yx}(m,n) = L_{M,i}'(x_{0.5})L_{M,j}'(y_{0.5})$	if $(j_y - 1 + j) \in (0, N_y^{E_x}]$ and $(i_y + i) \in (0, N_x^{E_x}]$
$D_{yx}(m,n) = D_{yx}(m,n) + L_{M,i}'(x_{0.5})L_{M,j}'(y_{0.5})$	if $(j_y - 1 + j) \in (0, N_y^{E_x}]$ and $(i_y + i) \notin (0, N_x^{E_x}]$
$D_{yx}(m,n) = D_{yx}(m,n) - L_{M,i}'(x_{0.5})L_{M,j}'(y_{0.5})$	if $(j_y - 1 + j) < 0$ or $(j_y - 1 + j) > N_y^{E_x} + 1$

Table A.10: Definition of i' and j' for $D_{yx}(m,n)$

Condition for i'	Value of i'	Condition for j'	Value of j'
if $(i_y + i) \in (0, N_x^{E_x}]$	$i_y + i$	if $(j_y - 1 + j) \in (0, N_y^{E_x}]$	$j_y + j - 1$
if $(i_y + i) \leq 0$	$1 - i_y - i$	if $(j_y + j - 1) < 0$	$1 - j_y - j$
if $(i_y + i) > N_x^{E_x}$	$2N_x^{E_x} - (i_y + i - 1)$	if $(j_y + j - 1) > N_y^{E_x} + 1$	$2N_y^{E_x} + 3 - j_y - j$

Table A.11: Definition of $D_{yz}(m,n)$. $m = i_y + (j_y - 1)N_x^{E_y} + (k_y - 1)N_x^{E_y}N_y^{E_y}$ and $n = i_y + (j' - 1)N_x^{E_z} + (k' - 1)N_x^{E_z}N_y^{E_z}$. j' and k' are defined in Table A.12

$D_{yz}(m,n) =$	if $(j_y - 1 + j) \in (0, N_y^{E_z}]$ and $(k_y + k) \in (0, N_z^{E_z}]$
$L'_{M,j}(y_{0.5})\, L'_{M,k}(z_{0.5})$	
$D_{yz}(m,n) = D_{yz}(m,n) +$	if $(j_y - 1 + j) \in (0, N_y^{E_z}]$ and $(k_y + k) \notin (0, N_z^{E_z}]$
$L'_{M,j}(y_{0.5})L'_{M,k}(z_{0.5})$	
$D_{yz}(m,n) = D_{yz}(m,n) -$	if $(j_y - 1 + j) < 0$ or $(j_y - 1 + j) > N_y^{E_z} + 1$
$L'_{M,j}(y_{0.5})L'_{M,k}(z_{0.5})$	

Table A.12: Definition of j' and k' for $D_{yz}(m,n)$

Condition for j'	Value of j'	Condition for k'	Value of k'
if $(j_y - 1 + j) \in (0, N_y^{E_z}]$	$j_y + j - 1$	if $(k_y + k) \in (0, N_z^{E_z}]$	$k_y + k$
if $(j_y - 1 + j) < 0$	$1 - j_y - j$	if $(k_y + k) \leq 0$	$1 - k_y - k$
if $(j_y - 1 + j) > N_y^{E_z} + 1$	$2N_y^{E_z} - (j_y + j - 3)$	if $(k_y + k) > N_z^{E_z}$	$2N_z^{E_z} + 1 - k_y - k$

Table A.13: Definition of $D_{zz}(m,n)$. $m = i_z + (j_z - 1)N_x^{E_z} + (k_z - 1)N_x^{E_z}N_y^{E_z}$ and $n = i' + (j' - 1)N_x^{E_z} + (k_z - 1)N_x^{E_z}N_y^{E_z}$. i' and j' are defined in Table A.14

$D_{zz}(m,n) = -L''_{M,i}(x_0)$	if $j = 0$, $i \neq 0$ and $(i_z + i) \in (0, N_x^{E_z}]$
$D_{zz}(m,n) = D_{zz}(m,n) + L''_{M,i}(x_0)$	if $j = 0$, $i \neq 0$ and $(i_z + i) \notin [0, N_x^{E_z} + 1]$
$D_{zz}(m,n) = -L''_{M,j}(y_0)$	if $i = 0$, $j \neq 0$ and $(j_z + j) \in (0, N_y^{E_z}]$
$D_{zz}(m,n) = D_{zz}(m,n) + L''_{M,j}(y_0)$	if $i = 0$, $j \neq 0$ and $(j_z + j) \notin [0, N_y^{E_z} + 1]$
$D_{zz}(m,n) = -L''_{M,i}(x_0) - L''_{M,j}(y_0)$	if $i = 0$ and $j = 0$

Table A.14: Definition of i' and j' for $D_{zz}(m,n)$

Condition for i'	Value of i'	Condition for j'	Value of j'
if $(i_z + i) \in (0, N_x^{E_z}]$	$i_z + i$	if $(j_z + j) \in (0, N_y^{E_z}]$	$j_z + j$
if $(i_z + i) < 0$	$-(i_z + i)$	if $(j_z + j) < 0$	$-(j_z + j)$
if $(i_z + i) > N_x^{E_z} + 1$	$2N_x^{E_z} - i_z - i + 2$	if $(j_z + j) > N_y^{E_z} + 1$	$2N_y^{E_z} - j_z - j + 2$

Table A.15: Definition of $D_{zx}(m,n)$. $m = i_z + (j_z - 1)N_x^{E_z} + (k_z - 1)N_x^{E_z}N_y^{E_z}$ and $n = i' + (j_z - 1)N_x^{E_x} + (k' - 1)N_x^{E_x}N_y^{E_x}$. i' and k' are defined in Table A.16

$D_{zx}(m,n) =$	if $(i_z + i) \in (0, N_x^{E_x}]$ and $(k_x - 1 + k) \in (0, N_z^{E_x}]$
$L'_{M,i}(x_{0.5})\, L'_{M,k}(z_{0.5})$	
$D_{zx}(m,n) = D_{zx}(m,n) +$	if $(i_z + i) \notin (0, N_x^{E_x}]$ and $(k_z - 1 + k) \in (0, N_z^{E_x}]$
$L'_{M,i}(x_{0.5})L'_{M,k}(z_{0.5})$	
$D_{zx}(m,n) = D_{zx}(m,n) -$	if $(k_z - 1 + k) < 0$ or $(k_z - 1 + k) > N_z^{E_x} + 1$
$L'_{M,i}(x_{0.5})L'_{M,k}(z_{0.5})$	

Table A.16: Definition of i' and k' for $D_{zx}(m,n)$

Condition for i'	Value of i'	Condition for j'	Value of j'
if $(i_z + i) \in$ $(0, N_x^{E_x}]$	$i_z + i$	if $(k_z - 1 + k) \in$ $(0, N_z^{E_x}]$	$k_z + k - 1$
if $(i_z + i) \le 0$	$1 - i_z - i$	if $(k_z - 1 + k) < 0$	$1 - k_z - k$
if $(i_z + i) > N_x^{E_x}$	$2N_x^{E_x} - (i_z + i - 1)$	if $(k_z - 1 + k) >$ $N_z^{E_z} + 1$	$2N_z^{E_z} + 3 - k_x - k$

A.3   Matrix $\mathbf{D_e}$ in Equation (4.31)

The scalar form of (4.10a) is

$$
\frac{1}{C_2}
\begin{bmatrix}
0 & -\frac{\partial}{\partial z} & \frac{\partial}{\partial y} \\[2mm]
\frac{\partial}{\partial z} & 0 & -\frac{\partial}{\partial x} \\[2mm]
-\frac{\partial}{\partial y} & \frac{\partial}{\partial x} & 0
\end{bmatrix}
\begin{bmatrix}
E_{DSC}^x \\[2mm]
E_{DSC}^y \\[2mm]
E_{DSC}^z
\end{bmatrix}
=
\begin{bmatrix}
H_{DSC}^x \\[2mm]
H_{DSC}^y \\[2mm]
H_{DSC}^z
\end{bmatrix},
\tag{A.9}
$$

Therefore, matrix $\mathbf{D_e}$ has the form

$$
\mathbf{D_e} =
\begin{bmatrix}
\mathbf{0} & \mathbf{D_e^{xy}} & \mathbf{D_e^{xz}} \\[2mm]
\mathbf{D_e^{yx}} & \mathbf{0} & \mathbf{D_e^{yz}} \\[2mm]
\mathbf{D_e^{zx}} & \mathbf{D_e^{zy}} & \mathbf{0}
\end{bmatrix},
\tag{A.10}
$$

where the six sub-matrices are defined in equations (A.11) to (A.16).

Table A.17: Definition of $D_{zy}(m,n)$. $m = i_z + (j_z - 1)N_x^{E_z} + (k_z - 1)N_x^{E_z}N_y^{E_z}$ and $n = i_z + (j'-1)N_x^{E_y} + (k'-1)N_x^{E_y}N_y^{E_y}$. j' and k' are defined in Table A.18

$D_{zy}(m,n) =$ $L'_{M,j}(y_{0.5})L'_{M,k}(z_{0.5})$	if $(k_z-1+k) \in (0, N_z^{E_y}]$ and $(j_z+j) \in (0, N_y^{E_y}]$
$D_{zy}(m,n) = D_{zy}(m,n) +$ $L'_{M,j}(y_{0.5})L'_{M,k}(z_{0.5})$	if $(k_z-1+k) \in (0, N_z^{E_y}]$ and $(j_z+j) \notin (0, N_y^{E_y}]$
$D_{zy}(m,n) = D_{zy}(m,n) -$ $L'_{M,j}(y_{0.5})L'_{M,k}(z_{0.5})$	if $(k_z-1+k) < 0$ or $(k_z-1+k) > N_z^{E_y}+1$

Table A.18: Definition of j' and k' for $D_{zy}(m,n)$

Condition for j'	Value of j'	Condition for k'	Value of k'
if $(j_z+j) \in (0, N_y^{E_y}]$	j_z+j	if $(k_z-1+k) \in (0, N_z^{E_y}]$	k_z+k-1
if $(j_z+j) \leq 0$	$1-j_z-j$	if $(k_z-1+k) < 0$	$1-k_z-k$
if $(j_z+j) > N_y^{E_y}$	$2N_y^{E_y}-(j_z+j-1)$	if $(k_z-1+k) > N_z^{E_y}+1$	$2N_z^{E_y}+3-k_z-k$

In equations (A.11) to (A.16), $N_\xi^{H_\zeta}$ is the number of H_ζ grid points in ξ-direction. i_{h_ξ}, j_{h_ξ}, and k_{h_ξ} are global index of H_ξ grid points in x-, y-, and z-directions, respectively. $i_{h_\xi} \in (0, N_x^{H_\xi}]$, $j_{h_\xi} \in (0, N_y^{H_\xi}]$, and $k_{h_\xi} \in (0, N_z^{H_\xi}]$. i, j, and k are local index of grid points involved in calculating the differential (as shown in Figure A.2), and they all range from $-M+1$ to M. i', j', and k' are the global counterpart of i, j, and k, respectively. $N_\xi^{E_\zeta}$ denote the number of E_ζ grid points in ξ-direction. $\xi_{0.5}$ means the differential is calculated at a point $0.5h_\xi$ away from two neighboring grid points (as illustrated in Figure A.2).

If the global index of E_ζ grid points in ξ-direction is less than one or it exceeds the number of E_ζ grid points in ξ-direction, the global index should be recalculated by symmetric and anti-symmetric extension for normal and tangential electric field, respectively.

132

Using equations (A.11) to (A.16), the six sub-matrices of matrix $\mathbf{D_e}$ can be assembled. By putting these sub-matrices together as shown in equation (A.10), one can obtain matrix $\mathbf{D_e}$.

$$
D_e^{xy}(m,n) = \left[
\begin{array}{ll}
-L'_{M,k}(z_{0.5}) & \text{if } (k_{h_x} - 1 + k) \in (0, N_z^{E_y}] \\[2mm]
D_e^{xy}(m,n) + L'_{M,k}(z_{0.5}) & \text{if } (k_{h_x} - 1 + k) \notin [0, N_z^{E_y} + 1]
\end{array}
\right], \quad \text{(A.11)}
$$

where $m = i_{h_x} + (j_{h_x} - 1) N_x^{H_x} + (k_{h_x} - 1) N_x^{H_x} N_y^{H_x}$, $n = i_{h_x} + (j_{h_x} - 1) N_x^{E_y} + (k' - 1) N_x^{E_y} N_y^{E_y}$, and

$$
k' = \left[
\begin{array}{ll}
k_{h_x} - 1 + k & \text{if } (k_{h_x} - 1 + k) \in (0, N_z^{E_y}] \\[2mm]
1 - k_{h_x} - k & \text{if } (k_{h_x} - 1 + k) < 0 \\[2mm]
2N_z^{E_y} - (k_{h_x} - 3 + k) & \text{if } (k_{h_x} - 1 + k) > N_z^{E_y} + 1
\end{array}
\right].
$$

$$
D_e^{xz}(m,n) = \left[
\begin{array}{ll}
L'_{M,j}(y_{0.5}) & \text{if } (j_{h_x} - 1 + j) \in (0, N_y^{E_z}] \\[2mm]
D_e^{xz}(m,n) - L'_{M,j}(y_{0.5}) & \text{if } (j_{h_x} - 1 + j) \notin [0, N_y^{E_z} + 1]
\end{array}
\right], \quad \text{(A.12)}
$$

where $m = i_{h_x} + (j_{h_x} - 1) N_x^{H_x} + (k_{h_x} - 1) N_x^{H_x} N_y^{H_x}$, $n = i_{h_x} + (j' - 1) N_x^{E_z} + (k_{h_x} - 1) N_x^{E_z} N_y^{E_z}$, and

$$
j' = \left[
\begin{array}{ll}
j_{h_x} - 1 + j & \text{if } (j_{h_x} - 1 + j) \in (0, N_y^{E_z}] \\[2mm]
1 - j_{h_x} - j & \text{if } (j_{h_x} - 1 + j) < 0 \\[2mm]
2N_y^{E_z} - (j_{h_x} - 3 + j) & \text{if } (j_{h_x} - 1 + j) > N_y^{E_z} + 1
\end{array}
\right].
$$

$$D_e^{yx}(m,n) = \begin{bmatrix} L'_{M,k}(z_{0.5}) & \text{if } (k_{h_y} - 1 + k) \in (0, N_z^{E_x}] \\ D_e^{yx}(m,n) - L'_{M,k}(z_{0.5}) & \text{if } (k_{h_y} - 1 + k) \notin [0, N_z^{E_x} + 1] \end{bmatrix}, \quad \text{(A.13)}$$

where $m = i_{h_y} + (j_{h_y} - 1) N_x^{H_y} + (k_{h_y} - 1) N_x^{H_y} N_y^{H_y}$, $n = i_{h_y} + (j_{h_y} - 1) N_x^{E_x} + (k' - 1) N_x^{E_x} N_y^{E_x}$, and

$$k' = \begin{bmatrix} k_{h_y} - 1 + k & \text{if } (k_{h_y} - 1 + k) \in (0, N_z^{E_x}] \\ 1 - k_{h_y} - k & \text{if } (k_{h_y} - 1 + k) < 0 \\ 2N_z^{E_x} - (k_{h_y} - 3 + k) & \text{if } (k_{h_y} - 1 + k) > N_z^{E_x} + 1 \end{bmatrix}.$$

$$D_e^{yz}(m,n) = \begin{bmatrix} -L'_{M,i}(x_{0.5}) & \text{if } (i_{h_y} - 1 + i) \in (0, N_x^{E_z}] \\ D_e^{yz}(m,n) + L'_{M,i}(x_{0.5}) & \text{if } (i_{h_y} - 1 + i) \notin [0, N_x^{E_z} + 1] \end{bmatrix}, \quad \text{(A.14)}$$

where $m = i_{h_y} + (j_{h_y} - 1) N_x^{H_y} + (k_{h_y} - 1) N_x^{H_y} N_y^{H_y}$, $n = i' + (j_{h_y} - 1) N_x^{E_z} + (k_{h_y} - 1) N_x^{E_z} N_y^{E_z}$, and

$$i' = \begin{bmatrix} i_{h_y} - 1 + i & \text{if } (i_{h_y} - 1 + i) \in (0, N_x^{E_z}] \\ 1 - i_{h_y} - i & \text{if } (i_{h_y} - 1 + i) < 0 \\ 2N_x^{E_z} - (i_{h_y} - 3 + i) & \text{if } (i_{h_y} - 1 + i) > N_x^{E_z} + 1 \end{bmatrix}.$$

$$D_e^{zx}(m,n) = \begin{bmatrix} -L'_{M,j}(y) & \text{if } (j_{h_z} - 1 + j) \in (0, N_y^{E_x}] \\ D_e^{zx}(m,n) + L'_{M,j}(y) & \text{if } (j_{h_z} - 1 + j) \notin [0, N_y^{E_x} + 1] \end{bmatrix}, \quad \text{(A.15)}$$

where $m = i_{h_z} + (j_{h_z} - 1) N_x^{H_z} + (k_{h_z} - 1) N_x^{H_z} N_y^{H_z}$, $n = i_{h_z} + (j' - 1) N_x^{E_x} + (k_{h_z} - 1)$

$N_x^{E_x} N_y^{E_x}$, and

$$
j' = \begin{bmatrix} j_{h_z} - 1 + j & \text{if } (j_{h_z} - 1 + j) \in (0, N_y^{E_x}] \\[2ex] 1 - j_{h_z} - j & \text{if } (j_{h_z} - 1 + j) < 0 \\[2ex] 2N_y^{E_x} - (j_{h_z} - 3 + j) & \text{if } (j_{h_z} - 1 + j) > N_y^{E_x} + 1 \end{bmatrix}.
$$

$$
D_e^{zy} (m, n) = \begin{bmatrix} L'_{M,i} (x_{0.5}) & \text{if } (i_{h_z} - 1 + i) \in (0, N_x^{E_y}] \\[2ex] D_e^{zy} (m, n) - L'_{M,i} (x_{0.5}) & \text{if } (i_{h_z} - 1 + i) \in [0, N_x^{E_y} + 1] \end{bmatrix}, \quad \text{(A.16)}
$$

where $m = i_{h_z} + (j_{h_z} - 1) N_x^{H_z} + (k_{h_z} - 1) N_x^{H_z} N_y^{H_z}$, $n = i' + (j_{h_z} - 1) N_x^{E_y} + (k_{h_z} - 1)$
$N_x^{E_y} N_y^{E_y}$, and

$$
i' = \begin{bmatrix} i_{h_z} - 1 + i & \text{if } (i_{h_z} - 1 + i) \in (0, N_x^{E_y}] \\[2ex] 1 - i_{h_z} - i & \text{if } (i_{h_z} - 1 + i) < 0 \\[2ex] 2N_x^{E_y} - (i_{h_z} - 3 + i) & \text{if } (i_{h_z} - 1 + i) > N_x^{E_y} + 1 \end{bmatrix}.
$$

Appendix B

Expression of Interpolation Matrices

This Appendix first demonstrates the derivation of interpolation matrices using interpolation matrix $\mathbf{W_x}$ for H_x in the 2-D TM case. Expression of other interpolation matrices is then summarized. It should be noted that only non-zero elements of an interpolation matrix are defined in this Appendix.

B.1   2-D TM Case

Take matrix $\mathbf{W_x}$ as an example to describe how interpolation matrix is calculated. $\mathbf{W_x}$ is used for interpolation of H_x. Using the regularized Lagrange interpolation basis, $H_x(x, y)$ can be expanded

$$H_x(x, y) = \sum_{i=-M+1}^{M} \sum_{j=-M+1}^{M} L_{M,i}^{H_x}(x) L_{M,j}^{H_x}(y) H_x^{i,j}, \qquad \text{(B.1)}$$

where i and j are local indexes of H_x grid points in x- and y-directions, respectively. The superscript H_x means the interpolation function is calculated on H_x grids. The

grid point with $i = 0$ and $j = 0$ has the global indexes i_0, and j_0, where $i_0 = \text{int}\left(\frac{x}{h_x}\right)$, $j_0 = \text{int}\left(\frac{y+0.5h_y}{h_y}\right)$. The symbol 'int' means taking the integer part of a number. h_ξ is the grid size in ξ-direction, where ξ can be x or y. Denote the number of H_x grid points in ξ-direction by $N_\xi^{H_x}$. If $i_0 + i \in (0, N_x^{H_x}]$, and $j_0 + j \in (0, N_y^{H_x}]$,

$$W_x(m,n) = L_{M,i}^{H_x}(x_m)L_{M,j}^{H_x}(y_m), \tag{B.2}$$

where m is the index of the pulse basis on Huygens' box, $n = i' + (j'-1)N_x^{H_x}$, $i' = i_0 + i$, and $j' = j_0 + j$. If $(i_0 + i)$ equals $N_x^{H_x} + 1$ or 0, the grid point falls on a y-directed conducting wall and the value of $H_x^{i,j}$ is zero. In that case, $H_x^{i,j}$ doesn't make contribution to the summation in (B.1). If $(i_0 + i)$ is larger than $N_x^{H_x} + 1$ or less than 0, anti-symmetric extension can be used to calculate (B.1). Furthermore, symmetric extension is applied when $(j_0 + j)$ is larger than $N_y^{H_x}$ or less than 1. Therefore,

$$W_x(m,n) = W_x(m,n) - L_{M,i}^{H_x}(x_m)L_{M,j}^{H_x}(y_m), \tag{B.3}$$

if $(i_0 + i) < 0$ or $(i_0 + i) > N_x^{H_x} + 1$, and

$$W_x(m,n) = W_x(m,n) + L_{M,i}^{H_x}(x_m)L_{M,j}^{H_x}(y_m), \tag{B.4}$$

if $(i_0 + i) \in (0, N_x^{H_x}]$ and $(j_0 + j) \notin (0, N_y^{H_x}]$, where $n = i' + (j'-1)N_x^{H_x}$,

$$i' = \begin{bmatrix} -(i_0 + i) & \text{if } (i_0 + i) < 0 \\ 2N_x^{H_x} - (i_0 + i - 2) & \text{if } (i_0 + i) > N_x^{H_x} + 1 \end{bmatrix},$$

$$j' = \begin{bmatrix} 1 - (j_0 + j) & \text{if } (j_0 + j) \leq 0 \\ 2N_y^{H_x} - (j_0 + j - 1) & \text{if } (j_0 + j) > N_y^{H_x} \end{bmatrix}.$$

137

Table B.1: Expression of $W_y(m,n)$. $n = i' + (j'-1)N_x^{H_y}$. i' and j' are defined in Table B.2

$L_{M,i}^{H_y}(x_m)L_{M,j}^{H_y}(y_m)$	if $(i_0+i) \in (0, N_x^{H_y}]$ and $(j_0+j) \in (0, N_y^{H_y}]$
$W_y(m,n) + L_{M,i}^{H_y}(x_m)L_{M,j}^{H_y}(y_m)$	if $(j_0+j) \notin [0, N_y^{H_y}+1]$
$W_y(m,n) - L_{M,i}^{H_y}(x_m)L_{M,j}^{H_y}(y_m)$	if $(i_0+i) \notin (0, N_x^{H_y}]$ and $(j_0+j) \in (0, N_y^{H_y}]$

Table B.2: i' and j' for $W_y(m,n)$, $i_0 = \text{int}\left(\frac{x_m + 0.5h_x}{h_x}\right)$ and $j_0 = \text{int}\left(\frac{y_m}{h_y}\right)$

Condition for i'	Value of i'	Condition for j'	Value of j'
$(i_0+i) \in (0, N_x^{H_y}]$	$i_0 + i$	$(j_0+j) \in (0, N_y^{H_y}]$	$j_0 + j$
$(i_0+i) \leq 0$	$1 - (i_0+i)$	$(j_0+j) < 0$	$-(j_0+j)$
$(i_0+i) \geq N_x^{H_y}+1$	$2N_x^{H_y} - (i_0+i-1)$	$(j_0+j) > N_y^{H_y}+1$	$2N_y^{H_y} - (j_0+j-2)$

Following a similar way, H_y interpolation matrix $\mathbf{W_y}$ and E_z interpolation matrix $\mathbf{W_z}$ can be derived. It should be mentioned that tangential and normal magnetic field components are symmetric and anti-symmetric along a conducting wall. Therefore, an abnormal global index of H_y grid points is dealt with using anti-symmetric and symmetric extension in y- and x-directions, respectively. 'Abnormal' means the index in ξ-direction exceeds the number of grid points along ξ-direction or the index is less than one. Meanwhile, a conducting wall of the cavity is an anti-symmetric plane for tangential electric field component. Hence, anti-symmetric extension is used to deal with an abnormal global index of E_z in x- or y- direction. Tables B.1 to B.4 present the expression of $\mathbf{W_y}$ and $\mathbf{W_z}$. In these Tables, $N_\xi^{H_y}$ and $N_\xi^{E_z}$ respectively denote the number of H_y and E_z grid points in ξ-direction, where ξ represents x or y.

Table B.3: Expression of $W_z(m,n)$. $n = i' + (j'-1)N_x^{E_z}$. i' and j' are defined in Table B.4

$L_{M,i}^{E_z}(x_m)L_{M,j}^{E_z}(y_m)$	if $(i_0+i) \in (0, N_x^{E_z}]$ and $(j_0+j) \in (0, N_y^{E_z}]$
$W_z(m,n) + L_{M,i}^{E_z}(x_m)L_{M,j}^{E_z}(y_m)$	if $(i_0+i) \notin [0, N_x^{E_z}+1]$ and $(j_0+j) \notin [0, N_y^{E_z}+1]$
$W_z(m,n) - L_{M,i}^{E_z}(x_m)L_{M,j}^{E_z}(y_m)$	1. if $(i_0+i) \notin [0, N_x^{E_z}+1]$ and $(j_0+j) \in (0, N_y^{E_z}]$; 2. if $(j_0+j) \notin [0, N_y^{E_z}+1]$ and $(i_0+i) \in (0, N_x^{E_z}]$

Table B.4: i' and j' for $W_z(m, n)$, $i_0 = \text{int}\left(\frac{x_m}{h_x}\right)$ and $j_0 = \text{int}\left(\frac{y_m}{h_y}\right)$

Condition for i'	Value of i'	Condition for j'	Value of j'
$(i_0 + i) \in (0, N_x^{E_z}]$	$i_0 + i$	$(j_0 + j) \in (0, N_y^{E_z}]$	$j_0 + j$
$(i_0 + i) < 0$	$-(i_0 + i)$	$(j_0 + j) < 0$	$-(j_0 + j)$
$(i_0 + i) > N_x^{E_z} + 1$	$2N_x^{E_z} - (i_0 + i - 2)$	$(j_0 + j) > N_y^{E_z} + 1$	$2N_y^{E_z} - (j_0 + j - 2)$

Table B.5: Definition of $W_x^e(m, n)$, m is the index of RWG basis function on Huygens' box, and $n = i' + (j' - 1)N_x^{E_x} + (k' - 1)N_x^{E_x}N_y^{E_x}$. i', j', and k' are defined in Table B.6

$W_x^e(m, n) =$ $L_{M,i}^{E_x}(x_m) L_{M,j}^{E_x}(y_m) L_{M,k}^{E_x}(z_m)$	if $(i_0 + i) \in (0, N_x^{E_x}], (j_0 + j) \in (0, N_y^{E_x}], (k_0 + k) \in (0, N_z^{E_x}]$
$W_x^e(m, n) = W_x^e(m, n) +$ $L_{M,i}^{E_x}(x_m) L_{M,j}^{E_x}(y_m) L_{M,k}^{E_x}(z_m)$	1. if $(i_0 + i) \notin (0, N_x^{E_x}]$, $(j_0 + j) \in (0, N_y^{E_x}]$ and $(k_0 + k) \in (0, N_z^{E_x}]$; 2. if $(j_0 + j) \notin [0, N_y^{E_x} + 1]$ and $(k_0 + k) \notin [0, N_z^{E_x} + 1]$
$W_x^e(m, n) = W_x^e(m, n) -$ $L_{M,i}^{E_x}(x_m) L_{M,j}^{E_x}(y_m) L_{M,k}^{E_x}(z_m)$	1. if $(j_0 + j) \notin [0, N_y^{E_x} + 1]$ and $(k_0 + k) \in (0, N_z^{E_x}]$; 2. if $(k_0 + k) \notin [0, N_z^{E_x} + 1]$ and $(j_0 + j) \in (0, N_y^{E_x}]$

B.2 Matrix $\mathbf{W^e}$ for Interpolation of Electric Field

The matrix $\mathbf{W^e}$ for the interpolation of electric field has the form of

$$\mathbf{W^e} = \begin{bmatrix} \mathbf{W_x^e} & \mathbf{0} & \mathbf{0} \\ \mathbf{0} & \mathbf{W_y^e} & \mathbf{0} \\ \mathbf{0} & \mathbf{0} & \mathbf{W_z^e} \end{bmatrix},$$

where sub-matrices $\mathbf{W_x^e}$, $\mathbf{W_y^e}$, and $\mathbf{W_z^e}$ are interpolation matrices for E_x, E_y, and E_z, respectively. Expression for these three sub-matrices is given in Tables B.5-B.10. In these tables, $N_\xi^{E_\zeta}$ represents the number of E_ζ grid points in ζ-direction. h_ζ denotes the grid size in ζ-direction. i, j, k are local indexes of grid points along x-, y- and z-directions, respectively, and they all range from $-M + 1$ to M.

Tables B.5 and B.6 give the expression for $\mathbf{W_x^e}$, the interpolation matrix for E_x. In

Table B.6: i', j', and k' for $W_x^e(m,n)$, $i_0 = \text{int}\left(\frac{x_m+0.5h_x}{h_x}\right)$, $j_0 = \text{int}\left(\frac{y_m}{h_y}\right)$ and $k_0 = \text{int}\left(\frac{z_m}{h_z}\right)$

Condition for i'	Value of i'	Condition for j'	Value of j'	Condition for k'	Value of k'
$(i_0+i) \in (0, N_x^{E_x}]$	i_0+i	$(j_0+j) \in (0, N_y^{E_x}]$	j_0+j	$(k_0+k) \in (0, N_z^{E_x}]$	k_0+k
$(i_0+i) \le 0$	$1-(i_0+i)$	$(j_0+j) < 0$	$-(j_0+j)$	$(k_0+k) < 0$	$-(k_0+k)$
$(i_0+i) \ge N_x^{E_x}+1$	$2N_x^{E_x}-(i_0+i-1)$	$(j_0+j) > N_y^{E_x}+1$	$2N_y^{E_x}-(j_0+j-2)$	$(k_0+k) > N_z^{E_x}+1$	$2N_z^{E_x}-(k_0+k-2)$

Table B.7: Definition of $W_y^e(m,n)$. $n = i' + (j'-1)N_x^{E_y} + (k'-1)N_x^{E_y}N_y^{E_y}$. i', j', and k' are defined in Table B.8

$W_y^e(m,n) =$	if $(i_0+i) \in (0, N_x^{E_y}], (j_0+j) \in (0, N_y^{E_y}], (k_0+k) \in (0, N_z^{E_y}]$
$L_{M,i}^{E_y}(x_m) L_{M,j}^{E_y}(y_m) L_{M,k}^{E_y}(z_m)$	
$W_y^e(m,n) = W_y^e(m,n) +$ $L_{M,i}^{E_y}(x_m) L_{M,j}^{E_y}(y_m) L_{M,k}^{E_y}(z_m)$	1. if $(j_0+j) \notin (0, N_y^{E_y}]$, $(i_0+i) \in (0, N_x^{E_y}]$ and $(k_0+k) \in (0, N_z^{E_y}]$; 2. if $(i_0+i) \notin [0, N_x^{E_y}+1]$ and $(k_0+k) \notin [0, N_z^{E_y}+1]$
$W_y^e(m,n) = W_y^e(m,n) -$ $L_{M,i}^{E_y}(x_m) L_{M,j}^{E_y}(y_m) L_{M,k}^{E_y}(z_m)$	1. if $(i_0+i) \notin [0, N_x^{E_y}+1]$ and $(k_0+k) \in (0, N_z^{E_y}]$; 2. if $(k_0+k) \notin [0, N_z^{E_y}+1]$ and $(i_0+i) \in (0, N_x^{E_y}]$

deriving tables B.5 and B.6, anti-symmetric extension is used to deal with abnormal global index in y- or z-directions, and symmetric extension is used for abnormal global index in x-direction. The term 'abnormal' means the global index in ξ-direction is less than one or it exceeds the number of grid points in ξ-direction.

Sub-matrix $\mathbf{W_y^e}$ for interpolation of E_y is defined in Tables B.7 and B.8. In deriving matrix $\mathbf{W_y^e}$, abnormal global index in z or x-direction is dealt with using anti-symmetric extension, and abnormal global index in y-direction is treated using symmetric extension.

Expression of E_z interpolation matrix $\mathbf{W_z^e}$ is presented in Tables B.9 and B.10.

Table B.8: i', j', and k' for $W_y^e(m,n)$, $i_0 = \text{int}\left(\frac{x_m}{h_x}\right)$, $j_0 = \text{int}\left(\frac{y_m+0.5h_y}{h_y}\right)$ and $k_0 = \text{int}\left(\frac{z_m}{h_z}\right)$

Condition for i'	Value of i'	Condition for j'	Value of j'	Condition for k'	Value of k'
$(i_0+i) \in (0, N_x^{E_y}]$	i_0+i	$(j_0+j) \in (0, N_y^{E_y}]$	j_0+j	$(k_0+k) \in (0, N_z^{E_y}]$	k_0+k
$(i_0+i) < 0$	$-(i_0+i)$	$(j_0+j) \leq 0$	$1-(j_0+j)$	$(k_0+k) < 0$	$-(k_0+k)$
$(i_0+i) > N_x^{E_y}+1$	$2N_x^{E_y} - (i_0+i-2)$	$(j_0+j) \geq N_y^{E_y}+1$	$2N_y^{E_y} - (j_0+j-1)$	$(k_0+k) > N_z^{E_y}+1$	$2N_z^{E_y} - (k_0+k-2)$

Table B.9: Definition of $W_z^e(m,n)$. $n = i' + (j'-1)N_x^{E_z} + (k'-1)N_x^{E_z}N_y^{E_z}$. i', j', and k' are defined in Table B.10

$W_z^e(m,n) =$	if $(i_0+i) \in (0, N_x^{E_z}]$, $(j_0+j) \in (0, N_y^{E_z}]$, $(k_0+k) \in$
$L_{M,i}^{E_z}(x_m) L_{M,j}^{E_z}(y_m) L_{M,k}^{E_z}(z_m)$	$(0, N_z^{E_z}]$
$W_z^e(m,n) = W_z^e(m,n) +$	1. if $(k_0+k) \notin (0, N_z^{E_z}]$, $(j_0+j) \in (0, N_y^{E_z}]$ and
$L_{M,i}^{E_z}(x_m) L_{M,j}^{E_z}(y_m) L_{M,k}^{E_z}(z_m)$	$(i_0+i) \in (0, N_x^{E_z}]$; 2. if $(i_0+i) \notin [0, N_x^{E_z}+1]$ and $(k_0+k) \notin [0, N_z^{E_z}+1]$
$W_z^e(m,n) = W_z^e(m,n) -$	1. if $(i_0+i) \notin [0, N_x^{E_z}+1]$ and $(j_0+j) \in (0, N_y^{E_z}]$;
$L_{M,i}^{E_z}(x_m) L_{M,j}^{E_z}(y_m) L_{M,k}^{E_z}(z_m)$	2. if $(j_0+j) \notin [0, N_y^{E_z}+1]$ and $(i_0+i) \in (0, N_x^{E_z}]$

Table B.10: i', j', and k' for $W_z^e(m,n)$, $i_0 = \text{int}\left(\frac{x_m}{h_x}\right)$, $j_0 = \text{int}\left(\frac{y_m}{h_y}\right)$ and $k_0 = \text{int}\left(\frac{z_m+0.5h_z}{h_z}\right)$

Condition for i'	Value of i'	Condition for j'	Value of j'	Condition for k'	Value of k'
$(i_0+i) \in (0, N_x^{E_z}]$	i_0+i	$(j_0+j) \in (0, N_y^{E_z}]$	j_0+j	$(k_0+k) \in (0, N_z^{E_z}]$	k_0+k
$(i_0+i) < 0$	$1-(i_0+i)$	$(j_0+j) < 0$	$-(j_0+j)$	$(k_0+k) \leq 0$	$1-(k_0+k)$
$(i_0+i) > N_x^{E_z}+1$	$2N_x^{E_z} - (i_0+i-2)$	$(j_0+j) > N_y^{E_z}+1$	$2N_y^{E_z} - (j_0+j-2)$	$(k_0+k) \geq N_z^{E_z}+1$	$2N_z^{E_z} - (k_0+k-1)$

Table B.11: Definition of $W_x^h(m,n)$. $n = i' + (j'-1)N_x^{H_x} + (k'-1)N_x^{H_x}N_y^{H_x}$. i', j', and k' are defined in Table B.12

$W_x^h(m,n) =$	if $(i_0+i) \in (0, N_x^{H_x}]$, $(j_0+j) \in (0, N_y^{H_x}]$, $(k_0+k) \in$
$L_{M,i}^{H_x}(x_m) L_{M,j}^{H_x}(y_m) L_{M,k}^{H_x}(z_m)$	$(0, N_z^{H_x}]$
$W_x^h(m,n) = W_x^h(m,n) +$	1. if $(i_0+i) \in (0, N_x^{H_x}]$ and $(j_0+j) \notin (0, N_y^{H_x}]$; 2. if
$L_{M,i}^{H_x}(x_m) L_{M,j}^{H_x}(y_m) L_{M,k}^{H_x}(z_m)$	$(i_0+i) \in (0, N_x^{H_x}]$ and $(k_0+k) \notin (0, N_z^{H_x}]$;
$W_x^h(m,n) = W_x^h(m,n) -$	if $(i_0+i) \notin [0, N_x^{H_x}+1]$
$L_{M,i}^{H_x}(x_m) L_{M,j}^{H_x}(y_m) L_{M,k}^{H_x}(z_m)$	

During the derivation of matrix $\mathbf{W_z^e}$, anti-symmetric extension is used to treat abnormal global index in y- or x-direction, and symmetric extension is used for abnormal global index in z-direction.

For numerical calculation, one may first assemble these three sub-matrices $\mathbf{W_x^e}$, $\mathbf{W_y^e}$, and $\mathbf{W_z^e}$, and then put them together to obtain $\mathbf{W^e}$.

B.3 Matrix $\mathbf{W^h}$ for Interpolation of Magnetic Field

The magnetic field interpolation matrix $\mathbf{W^h}$ has the same form as $\mathbf{W^e}$, and it can be written as

$$\mathbf{W^h} = \begin{bmatrix} \mathbf{W_x^h} & \mathbf{0} & \mathbf{0} \\ \mathbf{0} & \mathbf{W_y^h} & \mathbf{0} \\ \mathbf{0} & \mathbf{0} & \mathbf{W_z^h} \end{bmatrix},$$

where sub-matrices $\mathbf{W_x^h}$, $\mathbf{W_y^h}$ and $\mathbf{W_z^h}$ are interpolation matrices for H_x, H_y, and H_z, respectively. These three sub-matrices are defined in Tables B.11 to B.16, where h_ξ is the grid size along ξ-direction and $N_\xi^{H_\zeta}$ is the number of H_ζ grid points in ξ-direction. i, j, k represent local indexes of grid points along x-, y-, and z-directions, respectively.

Tables B.11 and B.12 present the expression of H_x interpolation matrix $\mathbf{W_x^h}$. Based

Table B.12: i', j', and k' for $W_x^h(m,n)$, $i_0 = \mathrm{int}\left(\frac{x_m}{h_x}\right)$, $j_0 = \mathrm{int}\left(\frac{y_m+0.5h_y}{h_y}\right)$ and $k_0 = \mathrm{int}\left(\frac{z_m+0.5h_z}{h_z}\right)$

Condition for i'	Value of i'	Condition for j'	Value of j'	Condition for k'	Value of k'
$(i_0+i)\in(0,N_x^{H_x}]$	i_0+i	$(j_0+j)\in(0,N_y^{H_x}]$	j_0+j	$(k_0+k)\in(0,N_z^{H_x}]$	k_0+k
$(i_0+i)<0$	$-(i_0+i)$	$(j_0+j)\le 0$	$1-(j_0+j)$	$(k_0+k)\le 0$	$1-(k_0+k)$
$(i_0+i)>N_x^{H_x}+1$	$2N_x^{H_x}-(i_0+i-2)$	$(j_0+j)\ge N_y^{H_x}+1$	$2N_y^{H_x}-(j_0+j-1)$	$(k_0+k)\ge N_z^{H_x}+1$	$2N_z^{H_x}-(k_0+k-1)$

Table B.13: Definition of $W_y^h(m,n)$. $n = i' + (j'-1)N_x^{H_y} + (k'-1)N_x^{H_y}N_y^{H_y}$. i', j', and k' are defined in Table B.14

$W_y^h(m,n)=$	if $(i_0+i)\in(0,N_x^{H_y}]$, $(j_0+j)\in(0,N_y^{H_y}]$, $(k_0+k)\in$
$L_{M,i}^{H_y}(x_m)\,L_{M,j}^{H_y}(y_m)\,L_{M,k}^{H_y}(z_m)$	$(0,N_z^{H_y}]$
$W_y^h(m,n)=W_y^h(m,n)+$	1. if $(j_0+j)\in(0,N_y^{H_y}]$ and $(i_0+i)\notin(0,N_x^{H_y}]$; 2. if
$L_{M,i}^{H_y}(x_m)\,L_{M,j}^{H_y}(y_m)\,L_{M,k}^{H_y}(z_m)$	$(j_0+j)\in(0,N_y^{H_y}]$ and $(k_0+k)\notin(0,N_z^{H_y}]$
$W_y^h(m,n)=W_y^h(m,n)-$	if $(j_0+j)\notin[0,N_y^{H_y}+1]$
$L_{M,i}^{H_y}(x_m)\,L_{M,j}^{H_y}(y_m)\,L_{M,k}^{H_y}(z_m)$	

on image theory, a conducting wall of the cavity is an anti-symmetric and symmetric plane for normal and tangential components of magnetic field, respectively. H_x is normal to y-z plane and parallel with x-y and x-z planes. Hence, symmetric extension is used when global indexes of grid points are abnormal in z- and y-directions, and anti-symmetric extension is utilized if the global index is abnormal in x-direction. The global index in ξ-direction is considered as abnormal when it becomes less than one or exceeds the number of grid points along ξ-direction. By using anti-symmetric or symmetric extension, one can change an abnormal index to a normal one.

For H_y interpolation matrix $\mathbf{W_y^h}$ defined in Tables B.13 and B.14, symmetric extension is used if the global index in z- or x-direction is abnormal, and anti-symmetric extension is applied when the global index in $y-$direction is abnormal.

Table B.14: i', j', and k' for $W_y^h(m,n)$, $i_0 = \text{int}\left(\frac{x_m+0.5h_x}{h_x}\right)$, $j_0 = \text{int}\left(\frac{y_m}{h_y}\right)$ and $k_0 = \text{int}\left(\frac{z_m+0.5h_z}{h_z}\right)$

Condition for i'	Value of i'	Condition for j'	Value of j'	Condition for k'	Value of k'
$(i_0+i) \in (0, N_x^{H_y}]$	i_0+i	$(j_0+j) \in (0, N_y^{H_y}]$	j_0+j	$(k_0+k) \in (0, N_z^{H_y}]$	k_0+k
$(i_0+i) \leq 0$	$1-(i_0+i)$	$(j_0+j) < 0$	$-(j_0+j)$	$(k_0+k) \leq 0$	$1-(k_0+k)$
$(i_0+i) \geq N_x^{H_y}+1$	$2N_x^{H_y} - (i_0+i-1)$	$(j_0+j) > N_y^{H_y}+1$	$2N_y^{H_y} - (j_0+j-2)$	$(k_0+k) \geq N_z^{H_y}+1$	$2N_z^{H_y} - (k_0+k-1)$

Table B.15: Definition of $W_z^h(m,n)$. $n = i' + (j'-1)N_x^{H_z} + (k'-1)N_x^{H_z}N_y^{H_z}$. i', j', and k' are defined in Table B.16

$W_z^h(m,n) = L_{M,i}^{H_z}(x_m) L_{M,j}^{H_z}(y_m) L_{M,k}^{H_z}(z_m)$	if $(i_0+i) \in (0, N_x^{H_z}], (j_0+j) \in (0, N_y^{H_z}], (k_0+k) \in (0, N_z^{H_z}]$
$W_z^h(m,n) = W_z^h(m,n) + L_{M,i}^{H_z}(x_m) L_{M,j}^{H_z}(y_m) L_{M,k}^{H_z}(z_m)$	1. if $(k_0+k) \in (0, N_z^{H_z}]$ and $(i_0+i) \notin (0, N_x^{H_z}]$; 2. if $(k_0+k) \in (0, N_z^{H_z}]$ and $(j_0+j) \notin (0, N_y^{H_z}]$
$W_z^h(m,n) = W_z^h(m,n) - L_{M,i}^{H_z}(x_m) L_{M,j}^{H_z}(y_m) L_{M,k}^{H_z}(z_m)$	if $(k_0+k) \notin [0, N_z^{H_z}+1]$

Table B.16: i', j', and k' for $W_z^h(m,n)$, $i_0 = \text{int}\left(\frac{x_m+0.5h_x}{h_x}\right)$, $j_0 = \text{int}\left(\frac{y_m+0.5h_y}{h_y}\right)$ and $k_0 = \text{int}\left(\frac{z_m}{h_z}\right)$

Condition for i'	Value of i'	Condition for j'	Value of j'	Condition for k'	Value of k'
$(i_0+i) \in (0, N_x^{H_z}]$	i_0+i	$(j_0+j) \in (0, N_y^{H_z}]$	j_0+j	$(k_0+k) \in (0, N_z^{H_z}]$	k_0+k
$(i_0+i) \leq 0$	$1-(i_0+i)$	$(j_0+j) \leq 0$	$1-(j_0+j)$	$(k_0+k) < 0$	$-(k_0+k)$
$(i_0+i) \geq N_x^{H_z}+1$	$2N_x^{H_z} - (i_0+i-1)$	$(j_0+j) \geq N_y^{H_z}+1$	$2N_y^{H_z} - (j_0+j-1)$	$(k_0+k) > N_z^{H_z}+1$	$2N_z^{H_z} - (k_0+k-2)$

144

The expression of H_z interpolation matrix $\mathbf{W_z^h}$ is given in Tables B.15 and B.16. If global index of H_z grid points is abnormal in x- or y-direction, symmetric extension is used to change it to a normal index. If it is abnormal in z-direction, anti-symmetric extension is applied.

Appendix C

Numerical Calculation of Integrals in (4.7) to (4.9)

Gaussian quadrature is first described in this appendix, and numerical calculation of Z_{mn}^e, Z_{mn}^c, and Z_{mn} is then detailed.

C.1   Gaussian Quadrature Rule for Triangle

In this work, M-point Gaussian quadrature is utilized to compute integral over a triangle. Consider the following integral,

$$I_T = \int\int_T f\left(\vec{r}\right) d\vec{r}, \tag{C.1}$$

where $f\left(\vec{r}\right)$ denotes a function, T is a triangle, and $\vec{r}$ is a point on T. Using M-point Gaussian quadrature, I_T is computed as

$$I_T = A_T \sum_{p=1}^{M} w_p f\left(\vec{r}_p\right), \tag{C.2}$$

where A_T is the area of the triangle T, w_p is the weight, and $\vec{r}_p$ is the integration point. The formula for computing $\vec{r}_p$ is

$$\vec{r}_p = \alpha_p \vec{v}_1 + \beta_p \vec{v}_2 + \gamma_p \vec{v}_3, \tag{C.3}$$

where $\vec{v}_1$, $\vec{v}_2$ and $\vec{v}_3$ are vertices of triangle T. α_p, β_p, and γ_p are pre-computed variables for choosing integration points. Table C.1 presents the 4-point Gaussian quadrature rule, which is used throughout this thesis.

C.2 Numerical calculation of Z_{mn}^e

Substituting (4.4) and (4.5) into (4.7) and applying M-point Gaussian quadrature, Z_{mn}^e can be calculated as

$$Z_{mn}^e = Z_{mn}^{e++} + Z_{mn}^{e+-} + Z_{mn}^{e-+} + Z_{mn}^{e--}, \tag{C.4}$$

where

$$Z_{mn}^{e++} = C_{mn_b} \sum_{p=1}^{M} \sum_{q_b=1}^{M} W_{pq_b} \left[\frac{(\vec{v}_m^+ - \vec{r}_p) \cdot (\vec{v}_n^{b+} - \vec{r}'_{q_b})}{4} - \frac{1}{k^2} \right], \vec{r}_p \in S_m^+ \text{ and } \vec{r}'_{q_b} \in S_b^{n+},$$

$$Z_{mn}^{e+-} = C_{mn_b} \sum_{p=1}^{M} \sum_{q_b=1}^{M} W_{pq_b} \left[\frac{(\vec{v}_m^+ - \vec{r}_p) \cdot (\vec{r}'_{q_b} - \vec{v}_n^{b-})}{4} + \frac{1}{k^2} \right], \vec{r}_p \in S_m^+ \text{ and } \vec{r}'_{q_b} \in S_b^{n-},$$

Table C.1: Four-point Gaussian Quadrature Rule

p	α_p	β_p	γ_p	w_p
1	0.33333333	0.33333333	0.33333333	-0.56250000
2	0.60000000	0.20000000	0.20000000	0.52083333
3	0.20000000	0.60000000	0.20000000	0.52083333
4	0.20000000	0.20000000	0.60000000	0.52083333

$$Z_{mn}^{e-+} = C_{mn_b} \sum_{p=1}^{M} \sum_{q_b=1}^{M} W_{pq_b} \left[\frac{(\vec{r}_p - \vec{v}_m^{-}) \cdot (\vec{v}_n^{b+} - \vec{r}_{q_b}')}{4} + \frac{1}{k^2} \right], \vec{r}_p \in S_m^{-} \text{ and } \vec{r}_{q_b}' \in S_b^{n+},$$

$$Z_{mn}^{e--} = C_{mn_b} \sum_{p=1}^{M} \sum_{q_b=1}^{M} W_{pq_b} \left[\frac{(\vec{r}_p - \vec{v}_m^{-}) \cdot (\vec{r}_{q_b}' - \vec{v}_n^{b-})}{4} - \frac{1}{k^2} \right], \vec{r}_p \in S_m^{-} \text{ and } \vec{r}_{q_b}' \in S_b^{n-},$$

$$C_{mn_b} = -\frac{j\omega\mu l_m l_{n_b}}{4\pi},$$

$$W_{pq_b} = w_p w_{q_b} \frac{e^{-jkR_{pq_b}}}{R_{pq_b}}.$$

$\vec{r}_p$ and $\vec{r}_{q_b}'$ denote vector positions of the pth Gaussian integration point in S_m and the q_bth Gaussian integration point in S_b^n, respectively. R_{pq_b} is the distance between $\vec{r}_p$ and $\vec{r}_{q_b}'$. w_p and w_{q_b} are weights at $\vec{r}_p$ and $\vec{r}_{q_b}'$, respectively. l_m is length of the mth triangle edge on the stirrer, and l_{n_b} denote length of the nth triangle edge on the Huygens' box. S_m^+ and S_m^- are triangles sharing edge m on the stirrer. S_b^{n+} and S_b^{n-} are triangles sharing edge n on the Huygens' box. $\vec{v}_m^{\pm}$ denote the vertex of $S_m^{\pm}$ opposite edge m on the stirrer, and $\vec{v}_n^{b\pm}$ is the vertex of $S_b^{n\pm}$ opposite edge n on Huygens' box.

C.3 Numerical calculation of Z_{mn}^c

Since $\nabla \times (G\vec{f}) = G\nabla \times \vec{f} + (\nabla G) \times \vec{f}$, and $\nabla \times \vec{f}(\vec{r}') = 0$, (4.8) can be rewritten as

$$Z_{mn}^c = -\int\int_{S_m} \vec{f}_m(\vec{r}) \cdot \int\int_{S_b^n} \left[\nabla G(\vec{r}, \vec{r}') \times \vec{f}_n(\vec{r}') \, d\vec{r}' \right] d\vec{r}, \qquad (C.5)$$

where $\nabla G(\vec{r}, \vec{r}') = -\frac{1}{R}\left(\frac{1}{R} + jk\right)G(\vec{r}, \vec{r}')(\vec{r} - \vec{r}')$. Therefore, applying M-point Gaussian quadrature and substituting (4.4) and (4.5) into (C.5), Z_{mn}^c can be calculated as

$$Z_{mn}^c = Z_{mn}^{c++} + Z_{mn}^{c+-} + Z_{mn}^{c-+} + Z_{mn}^{c--}, \qquad (C.6)$$

148

where

$$Z_{mn}^{c++} = C_{mn_b}^c \sum_{p=1}^{M} \sum_{q_b=1}^{M} W_{pq_b}^c (\vec{v}_m^+ - \vec{r}_p) \cdot \left[\vec{R}_{pq_b} \times \left(\vec{v}_n^{b+} - \vec{r}_{q_b}' \right) \right], \vec{r}_p \in S_m^+ \text{ and } \vec{r}_{q_b}' \in S_b^{n+},$$

$$Z_{mn}^{c+-} = C_{mn_b}^c \sum_{p=1}^{M} \sum_{q_b=1}^{M} W_{pq_b}^c (\vec{v}_m^+ - \vec{r}_p) \cdot \left[\vec{R}_{pq_b} \times \left(\vec{r}_{q_b}' - \vec{v}_n^{b-} \right) \right], \vec{r}_p \in S_m^+ \text{ and } \vec{r}_{q_b}' \in S_b^{n-},$$

$$Z_{mn}^{c-+} = C_{mn_b}^c \sum_{p=1}^{M} \sum_{q_b=1}^{M} W_{pq_b}^c (\vec{r}_p - \vec{v}_m^-) \cdot \left[\vec{R}_{pq_b} \times \left(\vec{v}_n^{b+} - \vec{r}_{q_b}' \right) \right], \vec{r}_p \in S_m^- \text{ and } \vec{r}_{q_b}' \in S_b^{n+},$$

$$Z_{mn}^{c--} = C_{mn_b}^c \sum_{p=1}^{M} \sum_{q_b=1}^{M} W_{pq_b}^c (\vec{r}_p - \vec{v}_m^-) \cdot \left[\vec{R}_{pq_b} \times \left(\vec{r}_{q_b}' - \vec{v}_n^{b-} \right) \right], \vec{r}_p \in S_m^- \text{ and } \vec{r}_{q_b}' \in S_b^{n-},$$

$$C_{mn_b}^c = \frac{l_m l_{n_b}}{16\pi},$$

$$W_{pq_b}^c = w_p w_{q_b} \frac{e^{-jkR_{pq_b}}}{R_{pq_b}^2} \left(\frac{1}{R_{pq_b}} + jk \right),$$

$$\vec{R}_{pq_b} = \vec{r}_p - \vec{r}_{q_b}'.$$

C.4   Numerical calculation of Z_{mn}

If the distance between S_m is far away from S_n, the calculation of Z_{mn} is simply

$$Z_{mn} = Z_{mn}^{++} + Z_{mn}^{+-} + Z_{mn}^{-+} + Z_{mn}^{--}, \tag{C.7}$$

where

$$Z_{mn}^{++} = C_{mn} \sum_{p=1}^{M} \sum_{q=1}^{M} W_{pq} \left[\frac{(\vec{v}_m^+ - \vec{r}_p) \cdot (\vec{v}_n^+ - \vec{r}_q')}{4} - \frac{1}{k^2} \right], \vec{r}_p \in S_m^+ \text{ and } \vec{r}_q' \in S_n^+,$$

$$Z_{mn}^{+-} = C_{mn} \sum_{p=1}^{M} \sum_{q=1}^{M} W_{pq} \left[\frac{(\vec{v}_m^+ - \vec{r}_p) \cdot (\vec{r}_q' - v_n^-)}{4} + \frac{1}{k^2} \right], \vec{r}_p \in S_m^+ \text{ and } \vec{r}_q' \in S_n^-,$$

149

$$Z_{mn}^{-+} = C_{mn} \sum_{p=1}^{M} \sum_{q=1}^{M} W_{pq} \left[\frac{(\vec{r}_p - \vec{v}_m^-) \cdot (\vec{v}_n^+ - \vec{r}_q')}{4} + \frac{1}{k^2} \right], \vec{r}_p \in S_m^- \text{ and } \vec{r}_q' \in S_n^+,$$

$$Z_{mn}^{--} = C_{mn} \sum_{p=1}^{M} \sum_{q=1}^{M} W_{pq} \left[\frac{(\vec{r}_p - \vec{v}_m^-) \cdot (\vec{r}_q' - \vec{v}_n^-)}{4} - \frac{1}{k^2} \right], \vec{r}_p \in S_m^- \text{ and } \vec{r}_q' \in S_n^-,$$

$$C_{mn} = \frac{j\omega\mu l_m l_n}{4\pi},$$

$$W_{pq} = w_p w_q \frac{e^{-jkR_{pq}}}{R_{pq}}.$$

l_n denotes length of the mth triangle edge on the stirrer. $\vec{r}_p$ is the pth Gaussian integration point on S_m, $\vec{r}_q'$ is the qth Gaussian integration point on S_n, and $R_{pq} = | \vec{r}_p - \vec{r}_q' |$. w_p and w_q are weights at $\vec{r}_p$ and $\vec{r}_q'$, respectively. S_n^+ and S_n^- are a pair of triangles sharing edge n on the stirrer. $\vec{v}_n^{\pm}$ denotes vertex of $S_n^{\pm}$ opposite edge n.

If S_m is near to S_n, R_{pq} may be very small and the problem of singularity may occur when evaluating Z_{mn}. In that case, the numerical and analytical integration method described in Section 7.3.2.2 of [98] is utilized to deal with the singularity. Green's function may be written as

$$G(\vec{r}, \vec{r}') = \frac{e^{-jkR} - 1}{4\pi R} + \frac{1}{4\pi R}. \tag{C.8}$$

The first term in (C.8) is free of singularity as

$$\lim_{R \to 0} \frac{e^{-jkR} - 1}{4\pi R} = \frac{-jk}{4\pi}. \tag{C.9}$$

Therefore, Z_{mn} can be calculated as the sum of two terms

$$Z_{mn} = Z_{mn}^{I} + Z_{mn}^{II}, \tag{C.10}$$

where

$$Z_{mn}^{I} = j\omega\mu \int\int_{S_m} \vec{f}_m(\vec{r}) \cdot \left[\int\int_{S_n} \vec{f}_n(\vec{r}') \frac{e^{-jkR}-1}{4\pi R} d\vec{r}' \right] d\vec{r}$$
$$+ \frac{1}{j\omega\epsilon} \int\int_{S_m} \nabla \cdot \vec{f}_m(\vec{r}) \left[\int\int_{S_n} \nabla' \cdot \vec{f}_n(\vec{r}') \frac{e^{-jkR}-1}{4\pi R} d\vec{r}' \right] d\vec{r}, \qquad \text{(C.11)}$$

and

$$Z_{mn}^{II} = j\omega\mu \int\int_{S_m} \vec{f}_m(\vec{r}) \cdot \left[\int\int_{S_n} \vec{f}_n(\vec{r}') \frac{1}{4\pi R} d\vec{r}' \right] d\vec{r}$$
$$+ \frac{1}{j\omega\epsilon} \int\int_{S_m} \nabla \cdot \vec{f}_m(\vec{r}) \left[\int\int_{S_n} \nabla' \cdot \vec{f}_n(\vec{r}') \frac{1}{4\pi R} d\vec{r}' \right] d\vec{r}. \qquad \text{(C.12)}$$

Z_{mn}^{I} is free of singularity, and it can be numerically calculated using M-point Gaussian quadrature. The formula for computing Z_{mn}^{I} is

$$Z_{mn}^{I} = Z_{mn}^{I++} + Z_{mn}^{I+-} + Z_{mn}^{I-+} + Z_{mn}^{I--}, \qquad \text{(C.13)}$$

$$Z_{mn}^{I++} = C_{mn} \sum_{p=1}^{M} \sum_{q=1}^{M} W_{pq}' \left[\frac{(\vec{v}_m^+ - \vec{r}_p) \cdot (\vec{v}_n^+ - \vec{r}_q')}{4} - \frac{1}{k^2} \right], \vec{r}_p \in S_m^+ \text{ and } \vec{r}_q' \in S_n^+,$$

$$Z_{mn}^{I+-} = C_{mn} \sum_{p=1}^{M} \sum_{q=1}^{M} W_{pq}' \left[\frac{(\vec{v}_m^+ - \vec{r}_p) \cdot (\vec{r}_q' - v_n^-)}{4} + \frac{1}{k^2} \right], \vec{r}_p \in S_m^+ \text{ and } \vec{r}_q' \in S_n^-,$$

$$Z_{mn}^{I-+} = C_{mn} \sum_{p=1}^{M} \sum_{q=1}^{M} W_{pq}' \left[\frac{(\vec{r}_p - \vec{v}_m^-) \cdot (\vec{v}_n^+ - \vec{r}_q')}{4} + \frac{1}{k^2} \right], \vec{r}_p \in S_m^- \text{ and } \vec{r}_q' \in S_n^+,$$

$$Z_{mn}^{I--} = C_{mn} \sum_{p=1}^{M} \sum_{q=1}^{M} W_{pq}' \left[\frac{(\vec{r}_p - \vec{v}_m^-) \cdot (\vec{r}_q' - \vec{v}_n^-)}{4} - \frac{1}{k^2} \right], \vec{r}_p \in S_m^- \text{ and } \vec{r}_q' \in S_n^-,$$

$$W_{pq}' = w_p w_q \frac{e^{-jkR_{pq}}-1}{R_{pq}}.$$

It should be noted that (C.9) can be used to calculate W_{pq}' if R_{pq} is below a user-defined tolerance τ_R (it is set to 1×10^{-6} in this work).

Applying M-point Gaussian quadrature to the outermost integral of (C.12), Z_{mn}^{II} can be calculated as

$$Z_{mn}^{II} = Z_{mn}^{II+} + Z_{mn}^{II-}, \tag{C.14}$$

$$Z_{mn}^{II+} = \frac{j\omega\mu l_m}{4\pi} \sum_{p=1}^{M} w_p \left[\frac{(\vec{v}_m^+ - \vec{r}_p)}{2} \cdot \vec{I}_p + \frac{1}{k^2} I_p' \right],$$

$$Z_{mn}^{II-} = \frac{j\omega\mu l_m}{4\pi} \sum_{p=1}^{M} w_p \left[\frac{(\vec{r}_p - \vec{v}_m^-)}{2} \cdot \vec{I}_p - \frac{1}{k^2} I_p' \right],$$

where

$$\vec{I}_p = \int\int_{S_n} \vec{f}_n(\vec{r}') \frac{1}{R_p} d\vec{r}', \tag{C.15}$$

$$I_p' = \int\int_{S_n} \nabla' \cdot \vec{f}_n(\vec{r}') \frac{1}{R_p} \vec{r}', \tag{C.16}$$

$R_p = | \vec{r}_p - \vec{r}' |$. Substituting (4.4) into (C.15),

$$\vec{I}_p = \frac{l_n}{2A_n^+} \left[\int\int_{S_n^+} (\vec{v}_n^+ - \vec{r}') \frac{1}{R_p} d\vec{r}' \right] + \frac{l_n}{2A_n^-} \left[\int\int_{S_n^-} (\vec{r}' - \vec{v}_n^-) \frac{1}{R_p} d\vec{r}' \right], \tag{C.17}$$

Since $\vec{v}_n^+ - \vec{r}' = \vec{v}_n^+ - \vec{r}_p + \vec{r}_p - \vec{r}'$, and $\vec{r}' - \vec{v}_n^- = \vec{r}' - \vec{r}_p + \vec{r}_p - \vec{v}_n^-$,

$$\vec{I}_p = \frac{l_n}{2A_n^+} \left[\int\int_{S_n^+} (\vec{r}_p - \vec{r}') \frac{1}{R_p} d\vec{r}' + (\vec{v}_n^+ - \vec{r}_p) \int\int_{S_n^+} \frac{1}{R_p} d\vec{r}' \right] + \tag{C.18}$$
$$\frac{l_n}{2A_n^-} \left[(\vec{r}_p - \vec{v}_n^-) \int\int_{S_n^-} \frac{1}{R_p} d\vec{r}' + \int\int_{S_n^-} (\vec{r}' - \vec{r}_p) \frac{1}{R_p} d\vec{r}' \right].$$

Using (4.5), (C.16) becomes
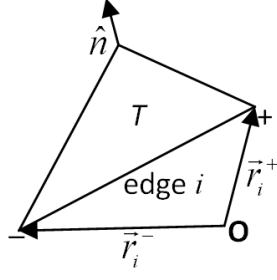
Figure C.1: A triangle T over which integrals (C.20) and (C.21) are to be calculated. $\vec{r}_i^-$ and $\vec{r}_i^+$ are position vectors of the nodes of the ith edge. Edges of the triangle are numbered anticlockwisely. $\hat{n}$ is unit vector normal to T and it can be calculated as $\left(\vec{r}_1^+ - \vec{r}_1^-\right) \times \left(\vec{r}_2^+ - \vec{r}_2^-\right) / \mid \left(\vec{r}_1^+ - \vec{r}_1^-\right) \times \left(\vec{r}_2^+ - \vec{r}_2^-\right) \mid.$

$$I'_p = \frac{l_n}{A_n^-} \int\int_{S_n^-} \frac{1}{R_p} \vec{r}' - \frac{l_n}{A_n^+} \int\int_{S_n^+} \frac{1}{R_p} \vec{r}'. \tag{C.19}$$

In equations (C.18) and (C.19), there are two kinds of integrals, i.e.

$$\vec{I}_a = \int\int_T \frac{\vec{r}' - \vec{r}}{R} d\vec{r}', \tag{C.20}$$

$$\vec{I}_b = \int\int_T \frac{1}{R} d\vec{r}', \tag{C.21}$$

where T represents a triangle, $\vec{r}'$ is the position vector of a point on T, $\vec{r}$ is a constant vector, and $R = \mid \vec{r} - \vec{r}' \mid$. Following [124], integrals (C.20) and (C.21) can be calculated analytically. Figure C.1 shows a triangle T. Edges of the triangle are numbered anticlockwisely. $\vec{r}_i^+$ and $\vec{r}_i^-$ denote position vectors of nodes of edge i. According to [124], $\vec{I}_a$ and I_b can be calculated as

$$\vec{I}_a = \frac{1}{2} \sum_{i=1}^{3} \hat{u}_i \left[\left(R_i^0\right)^2 \lg \frac{R_i^+ + l_i^+}{R_i^- + l_i^-} + l_i^+ R_i^+ - l_i^- R_i^- \right], \tag{C.22a}$$

$$I_b = \sum_{i=1}^{3} \hat{P}_i^0 \cdot \hat{u}_i \left[P_i^0 \lg \frac{R_i^+ + l_i^+}{R_i^- + l_i^-} - \mid d \mid Y_i \right], \tag{C.22b}$$

153

where

$$Y_i = \arctan \frac{P_i^0 l_i^+}{\left(R_i^0\right)^2 + \mid d \mid R_i^+} - \arctan \frac{P_i^0 l_i^-}{\left(R_i^0\right)^2 + \mid d \mid R_i^-},$$

$$l_i^\pm = \left(\vec{\rho}_i^\pm - \vec{\rho}\right) \cdot \hat{l}_i,$$

$$\hat{l}_i = \frac{\vec{\rho}_i^+ - \vec{\rho}}{\mid \rho_i^+ - \vec{\rho} \mid},$$

$$\vec{\rho}_i^\pm = \vec{r}_i^\pm - \hat{n}\left(\hat{n} \cdot \vec{r}_i^\pm\right),$$

$$\vec{\rho} = \vec{r} - \hat{n}\left(\hat{n} \cdot \vec{r}\right),$$

$$\hat{u}_i = \hat{l}_i \times \hat{n},$$

$$P_i^0 = \mid \left(\vec{\rho}_i^\pm - \vec{\rho}\right) \cdot \hat{u}_i \mid,$$

$$P_i^\pm = \mid \left(\vec{\rho}_i^\pm - \vec{\rho}\right) \mid,$$

$$\hat{P}_i^0 = \frac{\left(\vec{\rho}_i^+ - \vec{\rho}\right) - l_i^+ \hat{l}_i}{P_i^0},$$

$$R_i^0 = \sqrt{\left(P_i^0\right)^2 + d^2},$$

$$R_i^\pm = \sqrt{\left(P_i^\pm\right)^2 + d^2},$$

$$d = \hat{n} \cdot \left(\vec{r} - \vec{r}_1^+\right).$$

Using (C.22a) and (C.22b), $\vec{I}_p$ and I_p' can be calculated accordingly.

Author's Publications

A. Journal Papers

1. **H. P. Zhao** and Z. X. Shen, "Memory-effcient modeling of reverberation chambers using hybrid recursive update discrete singular convolution-method of moments," *IEEE Trans. Antennas Propagat.*, accepted, Dec. 2011.

2. **H. P. Zhao** and Z. X. Shen, "Efficient modeling of three-dimensional reverberation chambers using hybrid discrete singular convolution-method of moments," *IEEE Trans. Antennas Propagat.*, vol. 59, no. 8, pp. 2943-2953, Aug. 2011.

3. **H. P. Zhao** and Z. X. Shen, "Hybrid discrete singular convolution-method of moments analysis of a two-dimensional transverse magnetic reverberation chamber," *IEEE Trans. Electromagn. Compat.*, vol. 52, no. 3, pp. 612-619, Aug. 2010.

4. **H. P. Zhao** and Z. X. Shen, "Weighted Laguerre polynomials-finite difference method for time-domain modeling of thin wire antennas in a loaded cavity," *IEEE Antennas and Wireless Propagation Letters*, vol. 8, pp. 1131-1134, 2009.

5. **H. P. Zhao** and Z. X. Shen, "Modal-expansion analysis of a monopole in vibrating reverberation chamber," *Progress in Electromagnetic Research*, PIER 85, 303-322, 2008.

B. Techniqcal Report

1. Z. X. Shen, **H. P. Zhao**, W. Y. Zhong and C. Ruan, "Correlation of reverberation chamber," Defense Science Organization National Laboratories, Singapore, Technical Report DSOCL06201, 2010.

C. Conference Papers

1. **H. P. Zhao**, Z. X. Shen and E. P. Li, "Hybrid numerical modeling of reverberation chambers," *accepted by 2012 Asia-Pacific Symposium on Electromagnetic Compatibility*, Singapore, May 21-24, 2012.

2. **H. P. Zhao** and Z. X. Shen, "Fast and accurate prediction of reverberation chambers' resonant frequencies using time-domain integral equation and matrix pencil method," *in Procedings of 8th International Conference on Information, Communications and Signal Processing*, Singapore, Dec. 13-16, 2011.

3. **H. P. Zhao** and Z. X. Shen, "Recursive update-discrete singular convolution method for modeling highly resonant structures," *in Proceedings of 2011 IEEE Antennas and Propagation Society International Symposium*, Washington, USA, Jul. 3-8, 2011.

4. **H. P. Zhao** and Z. X. Shen, "Weighted Laguerre polynomials-discrete singular convolution method for efficient solution of Maxwell's equations," *in Proceedings of 2009 Asia-Pacific Microwave Conference*, Singapore, Dec. 7-10, 2009.

5. **H. P. Zhao** and Z. X. Shen, "On hybrid numerical methods for modeling complex electromagnetic problems," *in Proceedings of 2009 International Conference on Microwave Technology and Computational Electromagnetics*, Beijing, China, Nov. 3-6, 2009.

6. **H. P. Zhao** and Z. X. Shen, "Hybrid DSC-MoM analysis of two-dimensional transverse magnetic reverberation chamber," *in Proceedings of 2009 IEEE Antennas and Propagation Society International Symposium*, Charleston, SC, USA, Jun. 1-5, 2009.

7. **H. P. Zhao** and Z. X. Shen, "Modal-expansion analysis of a monopole in reverberation chamber," *in Procedings of 2008 Asia-Pacific Microwave Conference*, Hongkong, Dec. 16-20, 2008.

Bibliography

[1] *IEC 61000-4-21-Electromagnetic Compatibility (EMC)-Part 4-21: Testing and Measruement Techniques-Reverberation Chamber Test Methods.* International Electrotechnical Commission (IEC), Geneva, Switzerland Int. Std., CISPR/A and IEC SC 77B, Aug. 2003.

[2] G. Lerosey and J. Rosny, "Scattering cross section measurement in reverberation chamber," *IEEE Trans. Electromagn. Compat.*, vol. 49, no. 2, pp. 280–284, May 2007.

[3] U. Carlberg, P.-S. Kildal, A. Wolfgang, O. Sotoudeh, and C. Orlenius, "Calculated and measured absorption cross sections of lossy objects in reverberation chamber," *IEEE Trans. Electromagn. Compat.*, vol. 46, no. 2, pp. 146–154, May 2004.

[4] P. Hallbjorner, U. Carlberg, K. Madsen, and J. Andersson, "Extracting electrical material parameters of electrically large dielectric objects from reverberation chamber measurements of absorption cross section," *IEEE Trans. Electromagn. Compat.*, vol. 47, no. 2, pp. 291–303, May 2005.

[5] P.-S. Kildal and K. Rosengren, "Electromagnetic analysis of effective and apparent diversity gain of two parallel dipoles," *IEEE Antennas and Wireless Propag. Lett.*, vol. 2, no. 2, pp. 9–13, 2003.

[6] K. Rosengren and P.-S. Kildal, "Radiation efficiency, correlation, diversity gain, and capacity of a six monopole antenna array for a MIMO system: theory, simulation and measurement in reverberation chamber," *Proc. IEE Microw. Antennas and Propag.*, vol. 152, no. 1, pp. 7–16, Jan. 2005.

[7] A. Khaleghi, "Diversity techniques with parallel dipole antennas: Radiation pattern analysis," *Progress in Electromagnetics Research*, vol. 64, pp. 23–42, 2006.

[8] P.-S. Kildal and K. Rosengren, "Correlation and capacity of MIMO systems and mutual coupling, radiation efficiency, and diversity gain of their antennas: simulations and measurements in a reverberation chamber," *IEEE Communications Magazine*, vol. 42, no. 12, pp. 104–112, Dec. 2004.

[9] L. Garcia-Garcia, B. Lindmark, N. Jalden, and C. Orlenius, "MIMO capacity of antenna arrays evaluated using radio channel measurements, reverberation chamber and radiation patterns," *IET Microw. Antennas Propag.*, vol. 1, no. 6, pp. 1160–1169, Dec. 2007.

[10] C. Holloway, D. Hill, J. Ladbury, P. Wilson, G. Koepke, and J. Coder, "On the use of reverberation chambers to simulate a rician radio environment for the testing of wireless devices," *IEEE Trans. Antennas Propagat.*, vol. 54, no. 11, pp. 3167–3177, Nov. 2006.

[11] P.-S. Kildal, C. Carlsson, and J. Yang, "Measurement of free space impedances of small antennas in reverberation chambers," *Microw. Opt. Tech. Lett.*, vol. 32, no. 2, pp. 112–115, Jan. 2002.

[12] V. Fiumara, A. Fusco, V. Matta, and I. Pinto, "Free-space antenna field/pattern retrieval in reverberation environments," *IEEE Antennas and Wireless Propag. Lett.*, vol. 4, pp. 329–332, 2005.

[13] K. Rosengren, P.-S. Kildal, J. Carlsson, and O. Lunden, "A new method to measure radiation efficiency of terminal antennas," in *Proc. IEEE-APS Conf. Antennas and Propagation for Wireless Communications*, Nov. 2000, pp. 5–8.

[14] N. Kouveliotis, P. Trakadas, and C. Capsalis, "Theoretical investigation of the field conditions in a vibrating reverberation chamber with an unstirred component," *IEEE Trans. Electromagn. Compat.*, vol. 45, no. 1, pp. 77–80, 2003.

[15] F. Leferink, "In-SITU EMI testing of large naval radar systems using a vibrating intrinsic reverberation chamber (VIRC)," in *Proc. 2005 IEEE International Symposium on Electromagnetic Compatibility and Electromagnetic Ecology*, 2005, pp. 307–310.

[16] C. Bunting, "Shielding effectiveness in a two-dimensional reverberation chamber using finite-elment techniques," *IEEE Trans. Electromagn. Compat.*, vol. 45, no. 3, pp. 548–552, Aug. 2003.

[17] T. Loughry, "Frequency stirring: An alternate approach to mechanical mode-stirring for conduct of electromagnetic susceptibility testing," Phillips Lab., Tech.Rep.PL-TR-91-1036, 1991.

[18] D. Hill, "Electronic mode stirring for reverberation chambers," *IEEE Trans. Electromagn. Compat.*, vol. 36, no. 4, pp. 294–299, 1994.

[19] S. Yu and C. Bunting, "Statistical investigation of frequency-stirred reverberation chambers," in *Proc. 2003 IEEE International Symposium on Electromagnetic Compatibility*, vol. 1, Aug. 2003, pp. 155–159.

[20] U. Carlberg, P.-S. Kildal, and J. Carlsson, "Study of antennas in reverberation chamber using method of moments with cavity Green's function calculated by

Ewald summation," *IEEE Trans. Electromagn. Compat.*, vol. 47, no. 4, pp. 805–814, 2005.

[21] G. Cerri, V. Primiani, and P. Russo, "Source stirring mode for reverberation chambers," *IEEE Trans. Electromagn. Compat.*, vol. 47, no. 4, pp. 815–823, 2005.

[22] E. Voges and T. Eisenburger, "Electrical mode stirring in reverberating chambers by reactively loaded antennas," *IEEE Trans. Electromagn. Compat.*, vol. 49, no. 4, pp. 756–761, Nov. 2007.

[23] C. Bruns, "Three-dimensional simulation and experimental verification of a reverberation chamber," Ph.D. dissertation, Swiss Federal Institute of Technology Zurich, 2005.

[24] F. Moglie and A. P. Pastore, "FDTD analysis of plane wave superposition to simulate susceptibility tests in reverberation chambers," *IEEE Trans. Electromagn. Compat.*, vol. 48, no. 1, pp. 195–202, Feb. 2006.

[25] P. Bonnet, F. Diouf, C. Chauviere, S. Lallechere, M. Fogli, and F. Paladian, "Numerical simulation of a reverberation chamber with a stochastic collocation method," *C. R. Physique*, vol. 10, no. 1, pp. 54–64, 2009.

[26] D. Hill, "Linear dipole response in a reverberation chamber," *IEEE Trans. Electromagn. Compat.*, vol. 41, no. 4, pp. 365–368, Nov 1999.

[27] P. Corona, G. Ferrara, and M. Migliaccio, "Generalized stochastic field model for reverberating chambers," *IEEE Trans. Electromagn. Compat.*, vol. 46, no. 4, pp. 655–660, Nov 2004.

[28] K. Karlsson, J. Carlsson, and P.-S. Kildal, "Reverberation chamber for antenna measurements: modeling using method of moments, spectral domain techniques,

and asymptote extraction," *IEEE Trans. Antennas Propagat.*, vol. 54, no. 11, pp. 3106–3113, 2006.

[29] E. Laermans, L. Knockaert, and D. D. Zutter, "Two-dimensional method of moments modeling of lossless overmoded transverse magnetic cavities," *Journal of Computational Physics*, vol. 198, pp. 326–348, Feb. 2004.

[30] C. Bruns and R. Vahldieck, "A closer look at reverberation chambers-3-D simulation and experimental verification," *IEEE Trans. Electromagn. Compat.*, vol. 47, no. 3, pp. 612–626, Aug. 2005.

[31] G. Orjubin, E. Richalot, S. Mengue, M.-F. Wong, and O. Picon, "On the FEM modal approach for a reverberation chamber analysis," *IEEE Trans. Electromagn. Compat.*, vol. 49, no. 1, pp. 76–85, Feb. 2007.

[32] F. Moglie, "Convergence of the reverberation chambers to the equilibrium analyzed with the finite-difference time-domain algorithm," *IEEE Trans. Electromagn. Compat.*, vol. 46, no. 3, pp. 469–476, Aug. 2004.

[33] P. Bonnet, R. Vernet, S. Girard, and F. Paladian, "FDTD modeling of reverberation chamber," *Electronics Letters*, vol. 41, no. 20, Sept. 2005.

[34] G. Orjubin, F. Petit, E. Richalot, S. Mengué, and O. Picon, "Cavity losses modeling using lossless FDTD method," *IEEE Trans. Electromagn. Compat.*, vol. 48, no. 2, pp. 429–431, May 2006.

[35] F. Moglie and A. Pastore, "FDTD analysis of plane wave superposition to simulate susceptibility tests in reverberation chambers," *IEEE Trans. Electromagn. Compat.*, vol. 48, no. 1, pp. 195–202, Feb. 2006.

[36] G. Gradoni, F. Moglie, A. Pastore, and V. Primiani, "Numerical and experimental analysis of the field to enclosure coupling in reverberation chamber

and comparison with anechoic chamber," *IEEE Trans. Electromagn. Compat.*, vol. 48, no. 1, pp. 203–211, Feb. 2006.

[37] J. Clegg, A. Marvin, J. Dawson, and S. Porter, "Optimization of stirrer designs in a reverberation chamber," *IEEE Trans. Electromagn. Compat.*, vol. 47, no. 4, pp. 824–832, Nov. 2005.

[38] A. Coates, H. S. amd D. Coleby, A. Duffy, and A. Orlandi, "Validation of a three-dimensional transmission line matrix (TLM) model implementation of a mode-stirred reverberation chamber," *IEEE Trans. Electromagn. Compat.*, vol. 49, no. 4, pp. 734–744, Nov 2007.

[39] A. Coates and A. Duffy, "Maximum working volume and minimum working frequency tradeoff in a reverberation chamber," *IEEE Trans. Electromagn. Compat.*, vol. 49, no. 3, pp. 719–722, Aug 2007.

[40] W. Yu and R. Mittra, "A conformal FDTD software package modeling antennas and microstrip circuit components," *IEEE Antennas Propagat. Mag.*, vol. 42, no. 5, pp. 28–39, Oct. 2000.

[41] S. L. Ray, "Numerical dispersion and stability characteristics of time-domain methods on nonorthogonal meshes," *IEEE Trans. Antennas Propagat.*, vol. 41, no. 2, pp. 233–235, Feb. 1993.

[42] D. A. Hill, *Electromagnetic Fields in Cavities: Derterministic and Statistical Theories.* WILEY, NJ, 2009.

[43] R. Harrington, *Field Computation by Moment Methods.* New York: IEEE Press, 1993.

[44] J. Jin, *The Finite Element Method in Electromagnetics.* New York: John Wiley and Sons, 2002.

163

[45] N. Kouveliotis, P. Trakadas, and C. Capsalis, "Examination of field uniformity in vibrating intrinsic reverberation chamnber using the FDTD method," *Electron. Lett.*, vol. 38, no. 3, pp. 109–110, 2002.

[46] ——, "FDTD calculation of quality factor of vibrating intrinsic reverberation chamber," *Electron. Lett.*, vol. 38, no. 16, pp. 861–862, 2002.

[47] ——, "FDTD modelling of a vibrating intrinsic reverberation chamber," *J. of Electromagn. Waves and Appl*, vol. 17, no. 6, pp. 849–850, 2003.

[48] K. Yee, "Numerical solution of initial boundary value problems involving Maxwell's equation in isotropic media," *IEEE Trans. Antennas Propagat.*, vol. 14, no. 5, pp. 302–307, May 1966.

[49] H. P. Zhao and Z. X. Shen, "Modal-expansion analysis of a monopole in vibrating reverberation chamber," *Progress In Electromagnetics Research*, vol. PIER 85, pp. 303–322, 2008.

[50] S. M. Rao, D. R. Wilton, and A. W. Glisson, "Electromagnetic scattering by surfaces of arbitrary shape," *IEEE Trans. Antennas Propagat.*, vol. AP-30, no. 3, pp. 409–418, May 1982.

[51] U. Carlberg, P.-S. Kildal, and A.-A. Kishk, "Fast numerical model of reverberation chambers with metal stirrers using moment method and cavity Green's function calculated by Ewald summation," in *Proceedings of 2006 IEEE Antennas and Propagation Society International Symposium*, Albuquerque, NM USA, 9-14 July 2006.

[52] R. Vernet, P. Bonnet, S. Girard, and F. Paladian, "Use of the digital geometry for the generation of grids in the fdtd method," in *Proc. of Int. Symp. on Electromagnetic Compatibility*, Eindhoven, The Netherlands, 2004, pp. 36–41.

[53] A. C. Cangellaris and D. B. Wright, "Analysis of the numerical error caused by the stair-stepped approximation of a conducting boundary in FDTD simulations of electromagnetic phenomena," *IEEE Trans. Antennas Propagat.*, vol. 39, no. 10, pp. 1518–1525, Oct. 1991.

[54] http://www.ansoft.com/products/hf/hfss/.

[55] J. Song and W. Chew, "Multilevel fast-multipole algorithm for solving combined field integral equations of electromagnetic scattering," *Microw. Opt. Technol. Lett.*, vol. 10, pp. 14–19, Sept. 1995.

[56] S. Velamparambil, W. Chew, and J. Song, "10 million unknonwns: is it that big?" *IEEE Antennas Propagat. Mag.*, vol. 45, no. 2, pp. 43–58, 2003.

[57] S. Velamparambil and W. Chew, "Analysis and performance of a distributed memory multilevel fast multipole algorithm," *IEEE Trans. Antennas Propagat.*, vol. 53, no. 8, pp. 2719–2727, Aug. 2005.

[58] H. P. Zhao, J. Hu, and Z. P. Nie, "Block storing method for efficient storage of near group impedance in MLFMA," *Electron. Lett.*, vol. 44, no. 20, pp. 1171–1172, Sept. 2008.

[59] L. Gurel and O. Ergul, "Fast and accurate solutions of extremely large integral-equation problems discretised with tens of millions of unknowns," *Electron. Lett.*, vol. 43, no. 9, pp. 499–500, Apr. 2007.

[60] H. P. Zhao, J. Hu, and Z. P. Nie, "Parallelization of MLFMA with composite load partition criteria and asynchronous communication," *Applied Computational Electromagnetics Society Journal*, vol. 25, no. 2, pp. 167–173, Feb. 2010.

[61] J. M. Song, C. C. Lu, and W. C. Chew, "Multilevel fast multipole algorithm for electromagnetic scattering by large complex objects," *IEEE Trans. Antennas Propagat.*, vol. 45, no. 10, pp. 1488–1493, Oct. 1997.

[62] H. P. Zhao and J. M. Song, "On the truncation error of multipole expansion," *Private Communication*, Mar. 2011.

[63] W.-B. Ewe, L.-W. Li, C.-S. Chang, and J.-P. Xu, "AIM analysis of scattering and radiation by arbitrary surface-wire configurations," *IEEE Trans. Antennas Propagat.*, vol. 55, no. 1, pp. 162–166, Jan. 2007.

[64] J. R. Mautz and R. F. Harrington, "H-field, E-field, and combined-field solutions for conducting bodies of revolution," *AEU*, vol. 32, no. 4, pp. 157–164, Apr. 1978.

[65] O. Ergul and L. Gurel, "Iterative solutions of hybrid integral equations for co-existing open and closed surfaces," *IEEE Trans. Antennas Propagat.*, vol. 57, no. 6, pp. 1751–1758, Jun. 2009.

[66] W. C. Chew, J. M. Jin, E. Michielssen, and J. M. Song, *Fast and Efficient Algorithms in Computational Electromagnetics.* MA: Artech House, 2001.

[67] R. Graglia, D. Wilton, and A. Peterson, "High order interpolatory vector bases for computational electromagnetics," *IEEE Trans. Antennas Propagat.*, vol. 45, no. 3, pp. 329–342, Mar. 1997.

[68] G. Kang, J. Song, W. Chew, K. Donepudi, and J. Jin, "A novel grid-robust higher-order vector basis function for the method of moments," *IEEE Trans. Antennas Propagat.*, vol. 49, no. 6, pp. 908–915, Jun. 2001.

[69] E. Demaldent, D. Levadoux, and G. Cohen, "Spectral elements for the integral equations of time-harmonic maxwell problems," *IEEE Trans. Antennas Propagat.*, vol. 56, no. 9, pp. 3001–3010, Sept. 2008.

[70] J.-H. Lee and Q. Liu, "A 3-D spectral-element time-domain method for electromagnetic simulation," *IEEE Trans. Microwave Theory Tech.*, vol. 55, no. 5, pp. 983–991, May. 2007.

[71] A. Kabakian, V. Shankar, and W. Hall, "Unstructured grid-based discontinuous Galerkin method for broadband electromagnetic simulations," *Journal of Scientific Computing*, vol. 20, no. 3, pp. 405–431, Jun. 2004.

[72] S. Pernet, X. Ferrieres, and G. Cohen, "High spatial order finiet element method to solve maxwell's equations in time domain," *IEEE Trans. Antennas Propagat.*, vol. 53, no. 9, pp. 2889–2899, Sept. 2005.

[73] T. Xiao and Q. Liu, "Three-dimensional unstructured-grid discontinuous Galerkin method for maxwell's euqations with well-posed perfectly matched layer," *Microw. Opt. Technol. Lett.*, vol. 46, no. 5, pp. 459–463, Sept. 2005.

[74] Z. Shao, G. Wei, and S. Zhao, "DSC time-domain solution of Maxwell's equations," *Journal of Computational Physics*, vol. 189, pp. 427–453, 2003.

[75] Z. Shao, Z. Shen, Q. He, and G. Wei, "A generalized higher order finite-difference time-domain method and its application in guided-wave problems," *IEEE Trans. Microwave Theory Tech.*, vol. 51, no. 3, pp. 856–861, Mar. 2003.

[76] N. Kantartzis and T. Tsiboukis, *Higher Order FDTD Schemes for Waveguide and Antenna Structures.* USA: Morgan & Claypool Publishers, 2006.

[77] Q. H. Liu, "The PSTD algorithm: a time-domain method requiring only two cells per wavelength," *Microw. Opt. Technol. Lett.*, vol. 15, no. 3, pp. 158–165, June 1997.

[78] ——, "A pseudospectral frequency-domain (PSFD) method for computational electromagnetics," *IEEE Antennas Wireless Propagat. Lett.*, vol. 1, pp. 131–134, 2001.

[79] S. Yu, S. Zhao, and G. W. Wei, "Local spectral time splitting method for first- and second-order partial differential equations," *Journal of Computational Physics*, vol. 206, no. 2, pp. 727–780, July 2005.

[80] S. Y. Yang, Y. C. Zhou, and G. W. Wei, "Comparison of the discrete singular convolution algorithm and the Fourier pseudospectral method for solving partial differential equations," *Computer Physics Communications*, vol. 143, no. 2, pp. 113–135, Feburary 2002.

[81] J. M. Jin and J. L. Volakis, "TE scattering by an inhomogeneously filled aperture in a thick conducting plane," *IEEE Trans. Antennas Propagat.*, vol. 38, no. 8, pp. 1280–1286, Aug. 1990.

[82] D. Jiao, A. Ergin, B. Shanker, E. Michielssen, and J. Jin, "A fast higher-order time-domain finite element-boundary integral method for 3-D electromagnetic scattering analysis," *IEEE Trans. Antennas Propagat.*, vol. 50, no. 9, pp. 1192–1202, Sept. 2002.

[83] G. Jian, J. Volakis, A. Woo, and H. Wang, "A hybrid finite element-boundary integral method for the analysis of cavity-backed antennas of arbitrary shape," *IEEE Trans. Antennas Propagat.*, vol. 42, no. 9, pp. 1233–1242, Sept. 1994.

[84] X.-Q. Sheng, E. K.-N. Yung, C. H. Chan, J. M. Jin, and W. C. Chew, "Scattering from a large body with cracks and cavities by the fast and accurate finite-element boundary-integral method," *IEEE Trans. Antennas Propagat.*, vol. 48, no. 8, pp. 1153–1160, Aug. 2000.

[85] Y. Lin, J.-H. Lee, M. C. J. Liu, J. A. Mix, and Q. H. Liu, "A hybrid SIM-SEM method for 3-D electromagnetic scattering problems," *IEEE Trans. Antennas Propagat.*, vol. 57, no. 11, pp. 3655–3663, Sept. 2009.

[86] Z. Huang, K. Demarest, and R. Plumb, "An FDTD/MoM hybrid techinique for modeling complex antennas in the presence of heterogeneous grounds," *IEEE Trans. Geosci. Remote Sensing*, vol. 37, no. 6, pp. 2692–2698, Nov. 1999.

[87] W. Thiel, K. Sabet, and L. Katehi, "A hybrid MoM/FDTD approach for an efficient modeling of complex antennas on mobile platforms," in *Procedings of 33rd European Microwave Conference*, Oct. 2003, pp. 719–722.

[88] A. Monorchio, A. Bretones, R. Mittra, G. Manara, , and R. Martín, "A hybrid time-domain technique that combines the finite element, finite difference and method of moment techniques to solve complex electromagnetic problems," *IEEE Trans. Antennas Propagat.*, vol. 52, no. 10, pp. 2666–2674, Oct. 2004.

[89] C. Feng and Z. Shen, "A hybrid FD-MoM technique for predicting shielding effectiveness of metallic enclosures with apertures," *IEEE Trans. Electromagn. Compat.*, vol. 47, no. 3, pp. 456–462, Aug. 2005.

[90] Z. Shen, C. Law, and C. Qian, "Hybrid finite-element-modal-expansion method for matched magic T-junction," *IEEE Trans. Magn.*, vol. 38, no. 2, pp. 385–388, Mar. 2002.

[91] F. Arndt, J. Brandt, V. Catina, J. Ritter, I. Rullhusen, J. Dauelsberg, U. Hilgefort, and W. Wessel, "Fast CAD and optimization of waveguide components and aperture antennas by hybrid MM/FE/MoM/FD methods-state-of-the-art and recent advances," *IEEE Trans. Microwave Theory Tech.*, vol. 52, no. 1, pp. 292–304, Jan. 2004.

[92] F. Edelvik and G. Ledfelt, "A comparison of time-domain hybrid solvers for complex scattering problems," *Int. J. Numer. Model.*, vol. 15, pp. 475–487, 2002.

[93] M. Chai, T. Xiao, G. Zhao, and Q. H. Liu, "A hybrid PSTD/ADI-CFDTD method for mixed-scale electromagnetic problems," *IEEE Trans. Antennas Propagat.*, vol. 55, no. 5, pp. 1398–1406, May 2007.

[94] C. Pflaum and Z. Rahimi, "An iterative solver for the finite-difference frequency-domain (FDFD) method for the simulation of materials with negative permittivity," *Numer. Linear Algebra Appl.*, in press, 2010.

[95] R. Mittra, "A new CEM algorithm for solving real-world antenna and scattering problems," in *Proceedings of the Fourth European Conference on Antennas and Propagation*, 2010, pp. 1–3.

[96] A.-K. Tornberg and B. Engquist, "Numerical approximations of singular source terms in differential equations," *Journal of Computational Physics*, vol. 200, pp. 462–488, Nov. 2004.

[97] B. Fornberg, *A Practical Guide to Pseudospectral Methods.* New York: Cambridge University Press, 1998.

[98] W. Gibson, *The Method of Moments in Electromagnetics.* New York: Chapman and Hall, 2008.

[99] Y. Altman, "Undocumented matlab: Undocumented profiler options," http://undocumentedmatlab.com/blog/undocumented-profiler-options/, Apr. 2nd 2009.

[100] T. A. Davis and I. S. Duff, "A combined unifrontal/multifrontal method for unsymmetric sparse matrices," *ACM Trans. Math. Softw.*, vol. 25, no. 1, pp. 1–19, 1999.

[101] L. Tobón, J. Chen, and Q. H. Liu, "Spurious solutions in mixed finite element method for Maxwell's equations: Dispersion analysis and new basis functions," *Journal of Computational Physics*, vol. 230, no. 19, pp. 7300–7310, Aug. 2011.

[102] S. Zhao, "On the spurious solutions in high-order finite difference methods for eigenvalue problems," *Computer Methods in Applied Mechanics and Engineering*, vol. 196, no. 49, pp. 5031–5046, Jul. 2007.

[103] C. Lemoine, P. Besnier, and M. Drissi, "Estimating the effective sample size to select independent measurements in a reverberation chamber," *IEEE Trans. Electromagn. Compat.*, vol. 50, no. 2, pp. 227–236, May 2008.

[104] J. M. Jin, "Electromagnetic scattering from large, deep, and arbitrarily shaped open cavities," *Electromagn.*, vol. 18, no. 1, pp. 3–34, Jan./Feb. 1998.

[105] J. Liu and J. M. Jin, "A special higher order finite-element method for scattering by deep cavities," *IEEE Trans. Antennas Propagat.*, vol. 48, no. 5, pp. 694–703, May 2000.

[106] J. M. Jin, J. Liu, Z. Lou, and C. S. T. Liang, "A fully high-order finite-element simulation of scattering by deep cavities," *IEEE Trans. Antennas Propagat.*, vol. 51, no. 9, pp. 2420–2429, Sep. 2003.

[107] J. Liu and J. M. Jin, "Scattering analysis of a large body with deep cavities," *IEEE Trans. Antennas Propagat.*, vol. 51, no. 6, pp. 1157–1167, Jun. 2003.

[108] F. G. Hu, C. F. Wang, and Y. B. Gan, "Efficient calculation of interior scattering from large three-dimensional PEC cavity," *IEEE Trans. Antennas Propagat.*, vol. 55, no. 1, pp. 167–177, Jan. 2007.

[109] Z. Peng and X. Q. Sheng, "A flexible and efficient higher order FE-BI-MLFMA for scattering by a large body with deep cavities," *IEEE Trans. Antennas Propagat.*, vol. 56, no. 7, pp. 2031–2042, Jul. 2008.

[110] F. G. Hu and C. F. Wang, "Preconditioned formulation of FE-BI equations with domain decomposition method for calculation of electromagnetic scattering from cavities," *IEEE Trans. Antennas Propagat.*, vol. 57, no. 8, pp. 2506–2511, Aug. 2009.

[111] T. M. Wang and H. Ling, "A connection algorithm on the problem of EM scattering from arbitrary cavities," *J. EM Waves Applicat.*, vol. 5, no. 3, pp. 301–314, 1991.

[112] Z. P. Nie, H. G. Wang, and J. Wang, "A combined field solution with single operator for electromagnetic scattering from conductive targets with open cavities," *IEEE Trans. Antennas Propagat.*, vol. 56, no. 6, pp. 1734–1741, Jun. 2008.

[113] W. C. Wei and E. P. Li, "Transmitting antenna's reflected power and its influence on reverberation chamber calibration," *IEEE Trans. Electromagn. Compat.*, vol. 49, no. 1, pp. 192–194, Feb. 2007.

[114] S. M. Rao and D. R. Wilton, "Transient scattering by conducting surfaces of arbitrary shape," *IEEE Trans. Antennas Propagat.*, vol. 39, no. 1, pp. 56–61, Jan. 1991.

[115] D. A. Vechinski and S. M. Rao, "A stable procedure to calculate the transient scattering by conducting surfaces of arbitrary shape," *IEEE Trans. Antennas Propagat.*, vol. 40, no. 6, pp. 661–665, Jun. 1992.

[116] D. S. Weile, G. Pisharody, N. W. Chen, B. Shanker, and E. Michielssen, "A novel scheme for the solution of the time-domain integral equations of electromagnetics," *IEEE Trans. Antennas Propagat.*, vol. 52, no. 1, pp. 283–295, Jan. 2004.

[117] X. Wang, R. A. Wildman, D. S. Weile, and P. Monk, "A finite difference delay modeling approach to the discretization of the time domain integral equations of electromagnetics," *IEEE Trans. Antennas Propagat.*, vol. 56, no. 8, pp. 2442–2452, Aug. 2008.

[118] H. P. Zhao and Z. X. Shen, "Fast and accurate prediction of reverberation chambers' resonant frequencies using time-domain integral equation and matrix pencil method," in *Proceedings of 8th International Conference on Information, Communications and Signal Processing*, Singapore, Dec. 13-16 2011.

[119] Y.-S. Chung, T. Sarkar, B. Jung, M. Salazar-Palma, Z. Ji, S. Jang, and K. Kim, "Solution of time domain electric field integral equation using the Laguerre polynomials," *IEEE Trans. Antennas Propagat.*, vol. 52, no. 9, pp. 2319–2328, Sept. 2004.

[120] Z. Ji, T. Sarkar, B. Jung, M. Yuan, and M. Salazar-Palma, "Solving time domain electric field integral equation without the time variable," *IEEE Trans. Antennas Propagat.*, vol. 54, no. 1, pp. 258–262, Jan. 2006.

[121] H. P. Zhao and Z. X. Shen, "Weighted Laguerre polynomials-finite difference method for time-domain modeling of thin wire antennas in a loaded cavity," *IEEE Antennas Wireless Propagat. Lett.*, vol. 8, pp. 1131–1134, 2009.

[122] M. A. Mangoud, R. A. Abd-Alhameed, and P. S. Excell, "Simulation of human interaction with mobile telephones using hybrid techniques over cupoled domains," *IEEE Trans. Microwave Theory Tech.*, vol. 48, no. 11, pp. 2014–2021, Nov. 2000.

[123] S. Zhao and G. W. Wei, "Truly high-order FDTD method for inhomogeneous electromagnetic media," in *Proceedings of 2004 IEEE Antennas and Propagation Society International Symposium*, Monterey, CA USA, Jun 20-26 2004.

[124] D. Wilton, S. Rao, A. Glisson, D. Schaubert, M. Al-Bundak, and C. M. Butler, "Potential integrals for uniform and linear source distributions on polygonal and polyhedral domains," *IEEE Trans. Antennas Propagat.*, vol. 32, no. 3, pp. 276–281, Mar. 1984.